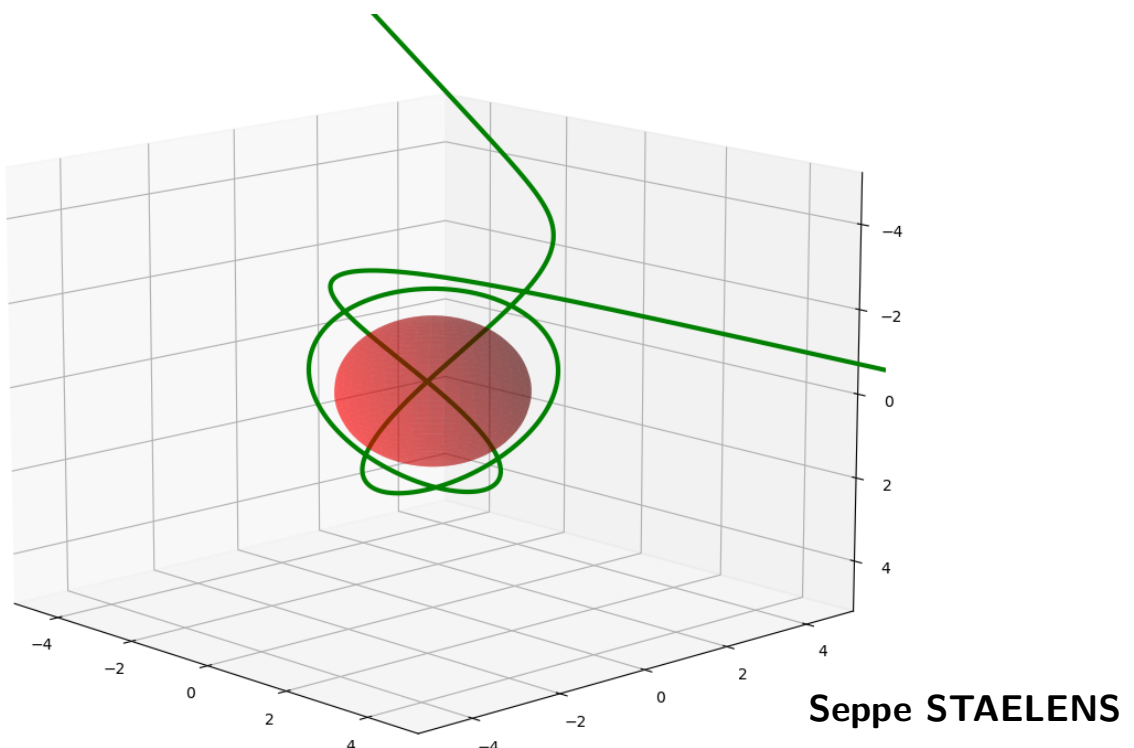


Black Hole Photon Rings Beyond General Relativity

Analytic and Ray-Tracing Approaches



Supervisor: Prof. T. Hertog
Affiliation *KU Leuven*

Mentor: Dr. D. Mayerson
Affiliation *KU Leuven*

Mentor: Dr. F. Bacchini
Affiliation *CU Boulder, KU Leuven*

Thesis presented in
fulfillment of the requirements
for the degree of Master of Science
in Physics

Academic year 2021-2022

© Copyright by KU Leuven

Without written permission of the promoters and the authors it is forbidden to reproduce or adapt in any form or by any means any part of this publication. Requests for obtaining the right to reproduce or utilize parts of this publication should be addressed to KU Leuven, Faculteit Wetenschappen, Geel Huis, Kasteelpark Arenberg 11 bus 2100, 3001 Leuven (Heverlee), Telephone +32 16 32 14 01. A written permission of the promoter is also required to use the methods, products, schematics and programs described in this work for industrial or commercial use, and for submitting this publication in scientific contests.

”In theory, theory and practice are the same. In practice, they are not.”
- Albert Einstein

Preface

Twelve hours until the deadline. These may be the first sentences you are reading, but they are the last ones I am writing. It feels unreal to finally hand in this Master's Thesis after a year of hard, devoted work. Working on this project has given me a first taste of what it really is like to be a physicist, and I have to say I enjoyed it thoroughly. Despite all the hard work, miscalculations and mood swings regarding the plausibility of writing everything I want - seriously, who starts writing in time? - I feel like this is something I want do for the coming years of my life. Luckily, I did not have to go through this alone, and therefore some words of appreciation are in order.

I want to start by thanking my promoter, prof. Thomas Hertog, for enabling me to take part in this project and fine-tuning the final result. I also want to thank you for the time you spent on discussing the pros and cons of the different plans I had for the future. Furthermore, I want to thank you for blessing me with dr. Daniel Mayerson as my daily supervisor.

Daniel, I cannot thank you enough for the *gazillion* contributions you made to this thesis over the entire year. You were always prepared to answer my questions, on and off-topic, and this thesis would not have been possible without you. Thank you for hinting me towards interesting presentations, proofreading my text when you would rather enjoy the wine at the conference and helping me shape my plans for the future.

I also want to thank dr. Fabio Bacchini, for helping me with the computational aspect of the project during the second semester. Additionally, I want to thank you for being my personal Linux Stack Exchange, teaching me to work with a supercomputer and starting your day in Colorado with a coffee and a plate of my questions. I look forward to meeting you in person in a few months!

I already want to thank dr. Pablo Marchant and dr. Pablo Antonio Cano for being the readers of this thesis.

But, the physics may be as interesting as it is, a year would not be complete without the many friends that brighten my day-to-day life. Bram, Cédric, Matthieu, thank you for being some of the best friends someone can have, and for watching my health by taking me along for a run or to the gym. Also, Matthieu, you are right: in the case of an error, the problem is always *between the chair and the screen*. To the rest of the P97 gang, thank you for creating an amazing atmosphere at *kot*. Working at the office would not be nearly as fun without the thesis squad. Thank you Thibeau, for all the great teamwork we have produced over the past years. Thank you Hannah for making it impossible not

to smile when you are your enthusiastic self. Thank you Cassandra for teaching me to drink coffee in the last few weeks, sparing me from a cardiac arrest due to an overdose of energy drinks. Thank you to Eva, Bram, Alex, Lucas, Michael and Egon as well.

Furthermore, I want to thank my parents for providing me with a warm home and every opportunity I could ask for in life. I want to thank the rest of my family, for supporting me and, at least pretend, to be interested in what I do. Finally, I want to thank my loving girlfriend, Lenka, for enduring my terrible sense of humour and making me happy for the past 4.5 years.

I want to acknowledge inspiring talks by Heino Falcke, Roger Blandford, Pedro Cunha, Daniel Mayerson, Stefan Vandoren, Peter Jonker and Samuel Gralla that have helped shape the story I am about to present you.

To you, reading this, I thank you for taking interest in my work. I proudly present you my Master's Thesis.

Seppe Staelens

Summary

Black holes are among the most poorly understood objects in the Universe. Within Einstein’s Theory of General Relativity they appear remarkably simple, as the spacetime around a black hole is determined by no more than 3 parameters. However, the introduction of quantum mechanical effects close to the event horizon leads to the field of black hole thermodynamics and the Information Paradox. As of today, the latter is still an unresolved problem, and it appears that an explanation requires a theory that combines elements of general relativity and quantum mechanics.

With the advent of gravitational wave observations (2016) and the image reconstructions of black holes by the Event Horizon Telescope (2019), it is now possible to probe black hole spacetimes at the horizon scale. This provides one of the best opportunities to study strong gravitational fields, and extract information on what properties a theory of quantum gravity should have.

This Master’s thesis focuses on features that are present in interferometric images, like the ones obtained by the Event Horizon Telescope. The goal is to study two black hole spacetimes beyond general relativity, and investigate the signatures that they imprint on the black hole shadow and the photon rings. For the latter, the focus is on the Lyapunov exponent that determines the relative widths of subsequent photon rings. The metrics of interest are the Johannsen metric, which deviates from the Kerr spacetime in a continuous way, and an almost-BPS metric, which is a solution of a particular supergravity theory. The concepts of black hole shadow and photon rings are explained by presenting the existing literature on the Kerr metric, after which similar methods are applied to the spacetimes of interest. We find that the predictions for these spacetimes can differ significantly from the predictions for the Kerr metric, meaning that they could serve as a test against the null hypothesis that astrophysical black holes are described by the Kerr metric.

Subsequently, these semi-analytical results are compared to the predictions of the ray-tracing code **RAPTOR**. The goal of this second part is to investigate the feasibility of performing the foregoing analysis on spacetimes that do not allow an analytical treatment. We find excellent agreement for the shadows, whereas the numerical analysis of the Lyapunov exponent produces results that deviate from analytical expectations. The reason for the latter is twofold. On the one hand, our numerical approach yields errors that are intrinsic to the method employed, but suggestions to improve it are given. On the other hand, the estimates for the Lyapunov are based on photon rings with low order n ,

whereas the theoretical value is calculated in the large- n limit.

Overall, this thesis presents predictions of two black hole spacetimes beyond general relativity, that can be tested by (an improved version of) the Event Horizon Telescope or similar surveys that reconstruct images of black holes on the horizon scale. Furthermore, it explores the possibility of using a numerical approach to make similar predictions for spacetimes in arbitrary theories, that can put Einstein's theory to the test.

Summary for a General Audience

In 1915, Einstein published his *Theory of General Relativity*, which describes gravity in a revolutionary way. His theory had many profound implications, among which the existence of *black holes*. A black hole is an object with a density so large that the gravitational pull in its immediate surroundings becomes extremely strong. As a consequence, anything that comes too close - even light itself - is inevitably pulled towards the center of the black hole. Contrary to popular belief, which depicts black holes as "cosmic vacuum cleaners" that devour everything, falling in can be avoided as long as sufficient distance from the black hole is maintained.

Being aware of a black hole's personal space, it is actually very interesting to study these objects. By now, it is clear to physicists that general relativity is *not* the final theory of gravity. It fails to explain several intricate problems, meaning that there must be a more general and detailed description. Since the gravity around black holes is so strong, it is expected that studying them will give clues to what lies beyond Einstein's theory.

In April 2019, scientists from the *Event Horizon Telescope Collaboration* released the first image of a black hole, a picture that reached many people via international news channels. It shows the supermassive black hole M87*, with a mass several billion times that of the Sun. Recently, they released a second picture visualizing the supermassive black hole Sagittarius A* at the center of our Milky Way. Since these images depict black holes and their immediate surroundings, scientists hope to find clues about an improved theory of gravity by analyzing them.

This Master's thesis is concerned with two theoretical descriptions of black holes that go beyond general relativity. The *Johannsen black hole* is a generalization of a black hole in general relativity. What makes this one interesting is that it is not a solution in a specific theory, but rather a model of some possible deviations that could occur. The other one, called the *almost-BPS* black hole, is a solution of a *supergravity* theory: this is one of the proposed theories that try to extend general relativity.

First, we present a pen-and-paper approach to give semi-analytical predictions for features in black hole images. Secondly, we employ a computer code to verify our results and investigate the possibility of making predictions based on the code alone. This would be useful for black holes that are too complicated for analytical calculations. The main goal is to characterize effects that these two black holes would have on images, and how they differ from the predictions of relativity. In this way, future images could possibly tell us how likely it is that astrophysical black holes are described by either one of these two models, or simply in what direction we should look for an extension of general relativity.

Contribution Statement

The work in sections 3.2 and 3.3 is my own, based on the treatment of the Kerr metric in section 3.1. In a similar fashion, the work in sections 4.1.2, 4.1.3, 4.3.3, 4.3.4 is my own. This includes the analysis of bound and nearly-bound geodesics in the Johannsen and almost-BPS black hole metrics, the production and analysis of their shadows, and the calculation and analysis of their Lyapunov exponents. The Figures 4.7 - 4.10, 4.14-4.17 and Tables 4.1, 4.2 are my original productions that summarize and illustrate this work. Note that the results in section 4.1.2 contain some overlap with a paper by T. Johannsen [60]. However, the results presented here were obtained independently from [60], so I have verified and generalized the analysis of [60].

I have implemented the Johannsen and almost-BPS metric in the **RAPTOR** code myself, meaning that the whole analysis of sections 5.2 and 5.3 is the result of my own work. Table 5.1 and all the Figures in Chapter 5, except for 5.1, and Appendix B are my own, just like the Python code used to make them. Furthermore, I have also implemented the metrics given in Appendix C in the **RAPTOR** code. This would not have been possible without the extensive explanation of the code by dr. Fabio Bacchini.

Using the metrics in Appendix C, I have produced the first ever images of black holes whose shadow breaks equatorial symmetry. These can be seen in Figure 6.1, and require further investigation. Although I have produced the figures myself, the idea to use these specific metrics came from dr. Daniel Mayerson.

I have presented a more accessible way of obtaining (3.22) as compared to the original treatment of [6], by simply calculating the zeroes of (3.20). With respect to the Lyapunov exponent, I have made the correspondence between what an off-equatorial observer and equatorial observer see explicit in (4.26, 4.32), and derived the approximation (4.27). Regarding the almost-BPS metric, I have presented a straightforward rescaling algorithm in section 2.2.4, to easily find parameters such that the black hole mass is equal to one, while maintaining any desired relative magnitude between the different parameters. Also, I have explicitly checked the separability of the Hamilton-Jacobi equations for this metric in section 3.3. To my knowledge, these minor results have not been explicitly remarked on in the literature.

List of Common Symbols

- a Rescaled angular momentum in the Kerr-Newman and Johannsen metric
- α 1) Spin parameter in the almost-BPS metric 2) Impact parameter on the observer screen
- α_{13} First deviation parameter in the Johannsen metric
- α_{22} Second deviation parameter in the Johannsen metric
- α_{52} Third deviation parameter in the Johannsen metric
- c Speed of light
- χ Energy-rescaled Carter constant (b)
- E Energy
- η Energy-rescaled Carter constant (a)
- γ Lyapunov exponent of the geodesic motion
- h Scale parameter in the almost-BPS metric
- k Carter constant (b)
- L Angular momentum
- λ Energy-rescaled angular momentum
- M_\odot The mass of the Sun, equal to $1.989 \cdot 10^{30}$ kg
- M Mass of a black hole
- ϕ_R Polar coordinate on the observer screen
- Q Carter constant (a)
- q Electric charge
- Q_Λ Conserved charges for the almost-BPS metric ($\Lambda = 0, 1, 2, 3$)
- R Radial coordinate on the observer screen
- r_+ Outer event horizon of the Kerr-Newman and Johannsen metric

- $\mathcal{R}(r)$ Radial potential for the geodesic motion
 R_S Schwarzschild radius
 $\Theta(\theta)$ Angular potential for the geodesic motion
 ζ Rescaling parameter for the almost-BPS metric parameters

List of Common Abbreviations

| | |
|--------|---------------------------------------|
| BH | black hole |
| BL | Boyer-Lindquist |
| BPS | Bogomol'nyi–Prasad–Sommerfield |
| EHT | Event Horizon Telescope Collaboration |
| GR | General Relativity |
| HJ | Hamilton-Jacobi |
| ISCO | innermost stable circular orbit |
| KN | Kerr-Newman |
| RN | Reissner-Nordström |
| Sgr A* | Sagittarius A* |
| SMBH | supermassive Black Hole |
| VLBI | Very Long Baseline Interferometry |

List of Figures

| | | |
|------|---|----|
| 1.1 | Interferometric data from the EHT observation of M87*. | 7 |
| 1.2 | Different baselines for the 2017 Event Horizon Telescope array. | 8 |
| 1.3 | Images of M87* and Sgr A* taken by the Event Horizon Telescope. | 8 |
| 1.4 | Example of a precise test of strong-field general relativity. | 11 |
| 3.1 | Qualitative plots of constants of motion for the Kerr photon sphere. | 34 |
| 3.2 | Solutions to the cubic equation $\eta = 0$ for Kerr. | 38 |
| 3.3 | Radius of bound equatorial orbits in the Kerr-Newman metric. | 40 |
| 3.4 | 3D-visualization of $\Theta(\rho, \theta)$ | 44 |
| 4.1 | Geometry of an observer screen aligned with a black hole. | 48 |
| 4.2 | Influence of the spin on the Kerr black hole shadow | 52 |
| 4.3 | Influence of the observing angle on the Kerr black hole shadow | 52 |
| 4.4 | The photon shell of the Kerr spacetime. | 53 |
| 4.5 | Influence of the charge on the Kerr-Newman black hole shadow | 54 |
| 4.6 | Shadow of extremal Kerr-Newman black holes | 55 |
| 4.7 | Influence of the parameters α_{13} and α_{22} on the shadow of a Johannsen black hole. | 57 |
| 4.8 | Difference in the almost-BPS black hole shadow for an observer above or below the equatorial plane. | 58 |
| 4.9 | Influence of the spin α and parameter h on the almost-BPS black hole shadow. | 60 |
| 4.10 | Influence of the charges Q_0, Q_1 on the almost-BPS black hole shadow. | 61 |
| 4.11 | Autocorrelation in black hole photons rings. | 63 |
| 4.12 | Visualization of photons rings according to the distinction in azimuthal angle. | 65 |
| 4.13 | The Lyapunov exponent $\gamma(\phi_R)$ for different values of the spin a in the Kerr metric. | 67 |
| 4.14 | The Lyapunov exponent $\gamma(\phi_R)$ for different values of the charge q in the Kerr-Newman metric. | 70 |
| 4.15 | The Lyapunov exponent $\gamma(\phi_R)$ for different values of the deviation parameters in the Johannsen metric. | 72 |
| 4.16 | The Lyapunov exponent $\gamma(\phi_R)$ for different values of the parameters α, h in the almost-BPS metric. | 74 |
| 4.17 | The Lyapunov exponent $\gamma(\phi_R)$ for different values of the charges Q_0, Q_1 in the almost-BPS metric. | 75 |
| 5.1 | Visualization of the celestial sphere in the geometry of ray tracing. | 78 |

| | | |
|-----|--|-----|
| 5.2 | Examples of ray-traced images and representative geodesics. | 80 |
| 5.3 | Overlays of semi-analytical shadow and RAPTOR results. | 84 |
| 5.4 | Zoom-in on the shadow of a Johannsen black hole. | 85 |
| 5.5 | Importance of the stopping condition for integration. | 86 |
| 5.6 | Example of a grazing geodesic. | 87 |
| 5.7 | Extraction of the photon rings and their widths. | 90 |
| 5.8 | Example of Lyapunov exponent estimates. | 91 |
| 6.1 | Ray-traced images of bumpy black holes. | 94 |
| A.1 | The third solution to $\eta = 0$ in the Kerr-Newman metric. | 105 |
| A.2 | The fourth solution to $\eta = 0$ in the Kerr-Newman metric. | 106 |
| B.1 | Lyapunov exponent estimates for the almost-BPS models. | 107 |
| B.2 | Lyapunov exponent estimates for the Kerr models. | 108 |
| B.3 | Lyapunov exponent estimates for the non-rotating Johannsen models. | 109 |
| B.4 | Lyapunov exponent estimates for the rotating Johannsen models. | 110 |

List of Tables

| | | |
|-----|--|----|
| 1.1 | Comparison of angular sizes for some astronomical targets. | 5 |
| 4.1 | Summary of the primary influence of the different parameters on the black hole shadow for the Johannsen and almost-BPS metrics. | 59 |
| 4.2 | Summary of the primary influences of the different parameters on the Lyapunov exponent for the Johannsen and almost-BPS metrics. | 73 |
| 5.1 | Summary of the numerical estimates for the Lyapunov exponent of different models. | 91 |

Contents

| | |
|---|-----------|
| Preface | i |
| Summary | iii |
| Summary for a General Audience | v |
| Contribution Statement | vii |
| List of Common Symbols | ix |
| List of Common Abbreviations | xi |
| List of Figures | xiii |
| List of Tables | xv |
| Contents | xvii |
| 1 Introduction | 1 |
| 1.1 The limits of General Relativity | 2 |
| 1.2 M87*, Sgr A* and the EHT | 5 |
| 1.3 Features in black hole images | 10 |
| 1.4 Motivation and research objectives | 12 |
| 2 Black Hole Metrics | 15 |
| 2.1 General Relativity - essentials | 15 |
| 2.2 Black hole metrics | 19 |
| 2.2.1 Schwarzschild black hole | 19 |
| 2.2.2 Kerr-Newman black hole | 20 |
| 2.2.3 Johannsen metric | 21 |
| 2.2.4 Almost-BPS black hole | 26 |
| 3 Geodesic Motion in Black Hole Spacetimes | 29 |
| 3.1 Bound geodesics in the Kerr metric | 29 |
| 3.1.1 The angular integral | 31 |
| 3.1.2 The radial potential | 34 |
| 3.1.3 Extension to Kerr-Newman | 37 |
| 3.2 Extension to the Johannsen metric | 39 |

| | | |
|----------|--|------------|
| 3.3 | Extension to the almost-BPS metric | 41 |
| 4 | Black Hole Shadows and Photon Rings | 47 |
| 4.1 | Black hole shadow | 47 |
| 4.1.1 | Extension to Kerr-Newman | 53 |
| 4.1.2 | Johannsen metric | 55 |
| 4.1.3 | Almost-BPS metric | 56 |
| 4.2 | Photon rings | 62 |
| 4.2.1 | Number of oscillations in polar direction | 62 |
| 4.2.2 | Number of orbits around the symmetry axis | 63 |
| 4.3 | Lyapunov exponent | 64 |
| 4.3.1 | Kerr metric | 64 |
| 4.3.2 | Extension to Kerr-Newman | 68 |
| 4.3.3 | Johannsen metric | 69 |
| 4.3.4 | Almost-BPS metric | 71 |
| 5 | Ray Tracing | 77 |
| 5.1 | Numerical ray tracing with RAPTOR | 77 |
| 5.1.1 | The RAPTOR code | 79 |
| 5.2 | Verification of the analytic shadow | 83 |
| 5.3 | Estimates of the Lyapunov exponent | 88 |
| 6 | Conclusion and Outlook | 93 |
| | Bibliography | 95 |
| | Appendices | 103 |
| A | Additional solutions to $\eta = 0$ for the KN metric | 105 |
| B | Estimates for the Lyapunov exponent | 107 |
| C | Bumpy black hole metrics | 111 |
| C.1 | Linearized bumpy black hole | 111 |
| C.2 | Manko-Novikov black hole | 112 |

Chapter 1

Introduction

When Albert Einstein published his Theory of General Relativity (GR) in 1915 [41], it did not take long before the impact of his work would become clear. On the one hand, it solved the standing problem of the precession of Mercury’s perihelion (see [86] for a recent study), and on the other hand he predicted the deflection and gravitational redshift of light. These phenomena had not been observed before, and their verification provided a remarkable confirmation of his theory [39, 74].

Even though it took some time for the theory to become firmly established, some of its most mind-blowing predictions followed only months after its publication. Karl Schwarzschild published a paper [77] in 1916 in which he described a solution to Einstein’s equations (see Section 2.1) with far-reaching implications. The solution describes a configuration that behaves as a very massive object, but is concentrated in one point, called *the singularity*. This Schwarzschild black hole (BH) has unprecedented properties. It boasts a point-of-no-return: anything (even light) that approaches the central singularity to a distance closer than the *Schwarzschild radius* is inevitably forced to proceed towards the central singularity. The name “black hole” originates from this *event horizon*, as light cannot escape from the region surrounding the singularity.

At the time, such a BH was a theoretical construct existing only on paper. This changed in 1972, when astronomers investigated the binary system Cygnus X-1. By analyzing the X-ray spectrum originating from the binary, together with the radial velocities of the visible companion, there was conclusive evidence that the companion of the star is a compact object [12, 92]. As the mass of this invisible companion was estimated to be larger than $2 M_{\odot}$, which is assumed to be too large for a white dwarf or neutron star, the authors concluded that the companion was possibly a black hole. The existence of black holes as astrophysical objects has since been firmly established, culminating in the first direct observation of merging black holes with the use of a gravitational wave detector [69]. Even more recently, the first images of black holes have been produced by the Event Horizon Telescope Collaboration (EHT) (see section 1.2). Both achievements mark the beginning of an era in which it will be possible to test GR in strong-gravity regimes around black holes on the horizon scale.

Before we can discuss the goals of this thesis, we must ask the question: why do we care so much about these BHs? After all, the interaction of humans with BHs is restricted to sci-fi movies - which will remain the case for the foreseeable future. To answer this question, we have to take a critical look at GR and face the fact that it is not perfect. The spacetime around a black hole turns out to be an excellent 'laboratory' to look for clues as to what lies beyond GR. Section 1.1 describes the limits of GR in black hole physics, motivating the quest for a theory of quantum gravity. Afterwards, the recent results of the EHT are reviewed in section 1.2, as this dissertation focuses on features that are present in BH images. Section 1.3 introduces these features in a qualitative manner, along with some of the recent literature to underline their relevance. Finally, we present the motivation and concrete goals of this Master's Thesis in section 1.4.

1.1 The limits of General Relativity

One of the key aspects of science is the continuous refinement of theories. Before Einstein revolutionized the way we think about gravity, the theory of gravitation as described by Newton seemed to be quite satisfactory. As technology improved and measurements became more accurate, mismatches between theory and experiment became apparent (the precession of the perihelion of Mercury, as mentioned earlier, is a great example). If the predictions of a theory no longer match observations, the theory should be reviewed. In this way, Newton's laws of motion were eventually replaced by GR. It is naive, however, to think that GR is the final description of gravity. Indeed, even though it explains many phenomena that Newton's laws could not, the community is convinced that this is not the final answer. This section summarizes some of the main instances where GR fails to give an explanation in the context of BH physics, and provides clues of where to look next.

First of all, it is important to realize that GR is very restrictive when it comes to BHs. The combination of GR and electromagnetism, captured in the Einstein-Maxwell equations, ensures that any black hole is described by exactly three parameters: the mass, angular momentum and electric charge. Such a black hole is described by the Kerr-Newman metric. This statement about BHs in GR combined with Maxwell's equations is called the *no-hair¹ theorem*. Given that the charge is assumed to be astrophysically irrelevant, we can restrict to the Kerr² metric. If we could observe a BH in nature that is not described by the Kerr metric, this would constitute a violation of the no-hair theorem, and therefore of the Einstein equations.

So far, no BH that deviates from Kerr has been observed. So the question arises: is this no-hair theorem even a *problem*? It was not, until its implications were realised by Stephen Hawking [57, 58]. Below, the steps that lead to the *information paradox* are briefly summarized. For a full, detailed account, the reader can consult [55, 72]. The following paragraphs are largely based on [18], in which a more accessible description is given.

¹Of course, black holes don't have literal 'hair'. It is a collective name for anything that differs from the three parameters described before.

²This is the Kerr-Newman metric with zero charge (see section 2.2.2). The Einstein-Maxwell equations reduce to the vacuum Einstein equations (2.5).

First of all, the work of Hawking and Bekenstein [8, 9] showed that a BH can be seen as a thermodynamical system with entropy. The entropy of a BH is related to its *surface area* A ; that is, the area of the surface determined by the event horizon. The *Bekenstein-Hawking* entropy of a BH is given by³

$$S_{\text{BH}} = \frac{A}{4G}. \quad (1.1)$$

The *surface gravity* κ , equal to $\frac{1}{4GM}$ for a Schwarzschild BH, takes the role of temperature, according to the relation

$$T_{\text{BH}} = \frac{\kappa}{2\pi}. \quad (1.2)$$

Remarkably, the analogy between BHs and thermodynamical systems can be extended in the formulation of the laws of black hole mechanics, which mirror the laws of thermodynamics. As an example, the analogy of the second law (entropy always increases) is the so-called *area theorem*, which states that the area of the event horizon is non-decreasing. Immediately, this gives rise to a tension with the no-hair theorem. The bridge between thermodynamics and the microscopic world is given by Boltzmann's law, which states that $S = k_B \ln W$. Here, W is the number of accessible *microstates* in which a system with entropy S can be found. It is tempting to take the analogy to BH physics. However, the no-hair theorem tells us that a BH is unique once its charge, spin and mass are determined, meaning that there is basically one (micro)state for a BH in GR. But the Bekenstein-Hawking entropy associated with the horizon of such a BH is enormous⁴, indicating a multitude of microstates. This is already a first hint that there is something we are overlooking. At this point one could adopt the viewpoint that there is no real problem, since we could presume that all the information about the microstate of a BH is hidden behind the event horizon, inaccessible to external observers.

But, it gets worse. Hawking showed that quantum mechanical effects allow black holes to create and emit particles, behaving like a black body with temperature given by (1.2). The problem is that this radiation causes the BH to *evaporate*. This seems to violate the area theorem, but this law was based on classical principles, before we introduced quantum mechanical effects. As the area decreases, the surface gravity increases and with it the temperature. This causes the evaporation to end in a long, yet finite time⁵. This evaporation really is a problem, as we can no longer count on the event horizon to conceal an intricate substructure containing the multitude of microstates. Furthermore, the Hawking radiation is precisely thermal, meaning that it can not carry information from the BH. Therefore, once the BH has evaporated and nothing but Hawking radiation remains, it seems like all the information that was stored in the BH is lost. This

³We are using units in which $\hbar = k = c = 1$. See section 2.1.

⁴The entropy of a black hole with mass $M = 10^6 M_\odot$ is on the order of $S_{\text{BH}} \sim 10^{88}$. The entropy for the matter fields in the Universe is estimated on the order of 10^{87} . This means that the entropy of a million-solar-mass supermassive Black Hole (SMBH) is larger than the entropy of all the matter in the Universe, which is truly remarkable [55].

⁵Hawking estimated in his paper [57] that primordial black holes with mass on the order of 10^{12} kg would have evaporated by now. Note that this is still much less than a solar mass ($M_\odot \sim 2 \cdot 10^{30}$ kg).

is the *information paradox*, which is one of the major puzzles in high-energy physics today.

One important thing to note is that Hawking's argument is derived in the context of a semi-classical combination of quantum mechanics with general relativity. It is not yet completely understood how this paradox is resolved in a fully consistent theory of quantum gravity. Careful progress is being made in that direction, and it is therefore interesting to discuss how the information paradox may be resolved.

A first option is that at some point the evaporation process stops, and a remnant remains. This remnant is then likely Planck-sized⁶ [55]. Another option is that information really is lost in the end. This would violate the basic physical principle of *unitarity*, which means that the information required to specify a state at a certain time is equal to that needed to specify it at later times. Both quantum mechanics and GR feature this principle, as the equations of motion govern the evolution of a system. A third option is to introduce non-local interactions in the theory. A particular approach that considers such non-local effects is referred to as *the holographic principle*. Roughly speaking, this principle suggests that information contained within a certain volume in $d + 1$ dimensions can be stored on the boundary of that volume, which has only d dimensions [13, 59, 80]. This idea stems from the formula 1.1, explicitly showing that the entropy of a BH scales as the area of its event horizon.

Progress has been made in string theory, with one of its great successes being the reproduction of the Bekenstein-Hawking entropy from a microscopic description for specific classes of black holes [79]. Furthermore, string theory boasts descriptions of black holes as "stringy configurations" known as fuzzballs that could solve these problems as well [3, 73]. Another way to avoid the outlined problems associated with black holes - and especially their event horizon - is to look for black hole mimickers. These so-called Exotic Compact Objects (ECOs) form a whole separate field of study, ranging from boson stars to gravastars [17].

Overall, the consensus is that there must be a theory of gravity beyond GR which takes quantum effects into account. The quest for such a theory of quantum gravity is ongoing for several decades, with the theoretical development of e.g. supergravity and string theory. However, any theory that describes nature must make measurable and falsifiable predictions, and this is no different for a new theory of relativity. Predictions are being put forward, but as they are based on theories that are relevant at large energies the experiments to test these predictions are generally hard. With the advent of gravitational wave observations, a multitude of tests of relativity in the strong gravity regime has become possible. Similarly, the EHT results signal the start of a complementary method to probe gravity in the vicinity of BHs. In the next section, we review the results of the EHT campaigns and explain how they can be used to put GR to the test.

⁶Planck scales refer to scales at which new quantum-gravity physics will become important. The Planck length which is mentioned here is defined as $l_P = \sqrt{\frac{\hbar G}{c^3}} \sim 10^{-35}$ m. This is very small in all senses, the size of an atomic nucleus being on the order of 10^{-15} m.

| Target | Characteristic physical size | Distance | Angular size |
|-------------------|-----------------------------------|--------------------------|-------------------------|
| Orbit of a planet | 1 AU | 100 pc | 10 mas |
| M87* [20] | 128 ± 13 AU | 16.8 ± 0.8 Mpc | 42 ± 3 μ as |
| Sgr A* [28] | $79_{-12}^{+22} \cdot 10^{-2}$ AU | 8.15 ± 0.15 kpc [75] | 51.8 ± 2.3 μ as |

Table 1.1: Typical dimensions of astronomical targets. The first entry corresponds to a hypothetical planet with an Earth-like orbit around its host star, observed face-on. The characteristic physical size for the two SMBHs corresponds to the Schwarzschild radius of a black hole with the same mass. The angular size is taken from the respective papers, and corresponds to the diameter of the surrounding ring.

1.2 M87*, Sgr A* and the EHT

Telescopes are inherently limited in their angular resolution. The lower limit for a telescope with a diameter D , observing at a wavelength λ is the *theoretical diffraction limit* λ/D . As an example, resolving the radius of Earth's orbit⁷ at a distance of 100 parsec⁸ requires an angular resolution of approximately 10 milliarcseconds (mas) (see Table 1.1). A telescope observing in the near-infrared at $2\ \mu\text{m}$ requires a diameter of 40 m to reach this diffraction limit. If we consider the SMBH Sagittarius A* (Sgr A*) at the center of our Milky Way, an angular resolution of about 50 μ as is required to resolve it. This means that the same telescope would need to have a radius of 8 km.

In order to avoid building telescopes of such enormous proportions, scientists have developed the technique of Very Long Baseline Interferometry (VLBI). In a standard radio interferometer, two telescopes separated by a distance B will observe a certain target at the same time. The distance B is called the *baseline*, and it is only the projected distance perpendicular to the line of sight that is of relevance. Very roughly speaking, this behaves like a telescope of diameter B , allowing for an enormous increase in resolution by combining two telescopes that are far apart.

In practice, this is more complicated. Contrary to an ordinary telescope, such an *interferometric array* probes *spatial frequencies*, typically denoted by (u, v) . Essentially, the (u, v) -plane is the Fourier transform of the regular image plane. The spatial frequency that is probed by a projected baseline B at a wavelength λ equals B/λ . This is only one Fourier component, from which it is difficult to reconstruct the image. Therefore, the goal is to measure many of these spatial frequencies: this is done by varying baselines, wavelengths and using the rotation of the Earth which changes the projected baselength. The Fourier transform of the brightness distribution is called the *visibility* $V(u, v)$, which is generally a complex number. Therefore, plots usually show $|V|$ or its square. The (u, v) -coverage and visibility amplitude are the main data for the reconstruction of an

⁷The radius of Earth's orbit around the Sun is equal to 1 Astronomical Unit (AU), which is approximately equal to 150 million km.

⁸A parsec is a measure of distance equal to $3.09 \cdot 10^{16}$ m. For reference, our nearest stellar neighbour Proxima Centauri is located at approximately 1.3 parsec.

image as obtained by an interferometric array. An example is shown in Figure 1.1. The main takeaway for this figure is that the visibility amplitude is well described by (the absolute value of) a Bessel function J_0 , indicating the presence of a ring-like structure: this is what is seen in the actual image (see Figure 1.3, left). A detailed explanation of radio interferometry in astronomy can be found in e.g. [82].

The goal of the EHT was to use VLBI to construct the first ever images of BHs on the horizon scale, in order to test GR in this extreme environment. Given the difficulty to obtain a good resolution, their first objective was to image M87*, the SMBH in the center of the galaxy M87, and Sgr A*. The reason is that these are the two SMBHs with the largest angular size in the sky. In this first stage, the EHT was a global array of 8 stations at 6 different geographical locations, ranging from the South Pole (which was not included in the M87* observations) to Hawaii and Spain. This is shown in Figure 1.2. The baselines ranged from 160 m to 10 700 km with respect to M87*. Given that the observations are taken at a wavelength of 1.3 mm, the theoretical angular resolution was on the order of $25 \mu\text{as}$.

The first results on M87* have been published in 2019 [20–25]. This SMBH is located at a distance of $16.8 \pm 0.8 \text{ Mpc}$. Prior mass estimates exist, for example $(6.6 \pm 0.4) \cdot 10^9 M_\odot$ based on stellar dynamics [45] and $3.5_{-0.7}^{+0.9} \cdot 10^9 M_\odot$ based on observations of the gas dynamics [90]. The EHT observations suggest $M = (6.5 \pm 0.7) \cdot 10^9 M_\odot$, consistent with the first estimate. The image has been modelled using General Relativistic Magnetohydrodynamic (GRMHD) simulations: it is well described by a Kerr black hole (see Chapter 2), surrounded by a hot, magnetized accretion disk of plasma. The viewing angle⁹ is very well restricted by independent studies, and the adopted value is $\theta \approx 17^\circ$ [89]. The modelling is done by comparing the image to a large library of synthetic images, obtained through various simulations. It should be noted that this modelling procedure does not lead to a unique, best fit. Rather, several different models can explain the observed data equally well (e.g. some models have very low spin, whereas others have $a/M = 0.94$). A large part of this uncertainty is associated with the model of the plasma and the emission in the accretion disk.

The overall conclusion is that the data are consistent with the null hypothesis that the SMBH is described by the Kerr metric. The authors do note that it is harder to rule out alternative theories, as they can closely resemble the Kerr metric. However, the observations are able to rule out some specific exotic compact objects. In 2021, the collaboration released two more papers investigating the polarization and the magnetic field [26, 27].

Together with M87*, the main object of interest for this first stage of the EHT was Sgr A*. It is the source at the center of our own Milky Way, associated with a SMBH. Earlier evidence for its nature was obtained at the end of the last century by observations of stars in the Galactic Centre [1, 40, 46]. By studying the proper motions of these stars, it was shown that our galaxy harbors a SMBH with mass $2.6 \pm 0.2 \cdot 10^6 M_\odot$. This was a crucial

⁹This is the angle between the rotation axis of the black hole and the line of sight. The SMBH M87* produces a very large jet, which is likely to be directed along the rotation axis. This constrains the viewing angle very well in this case.

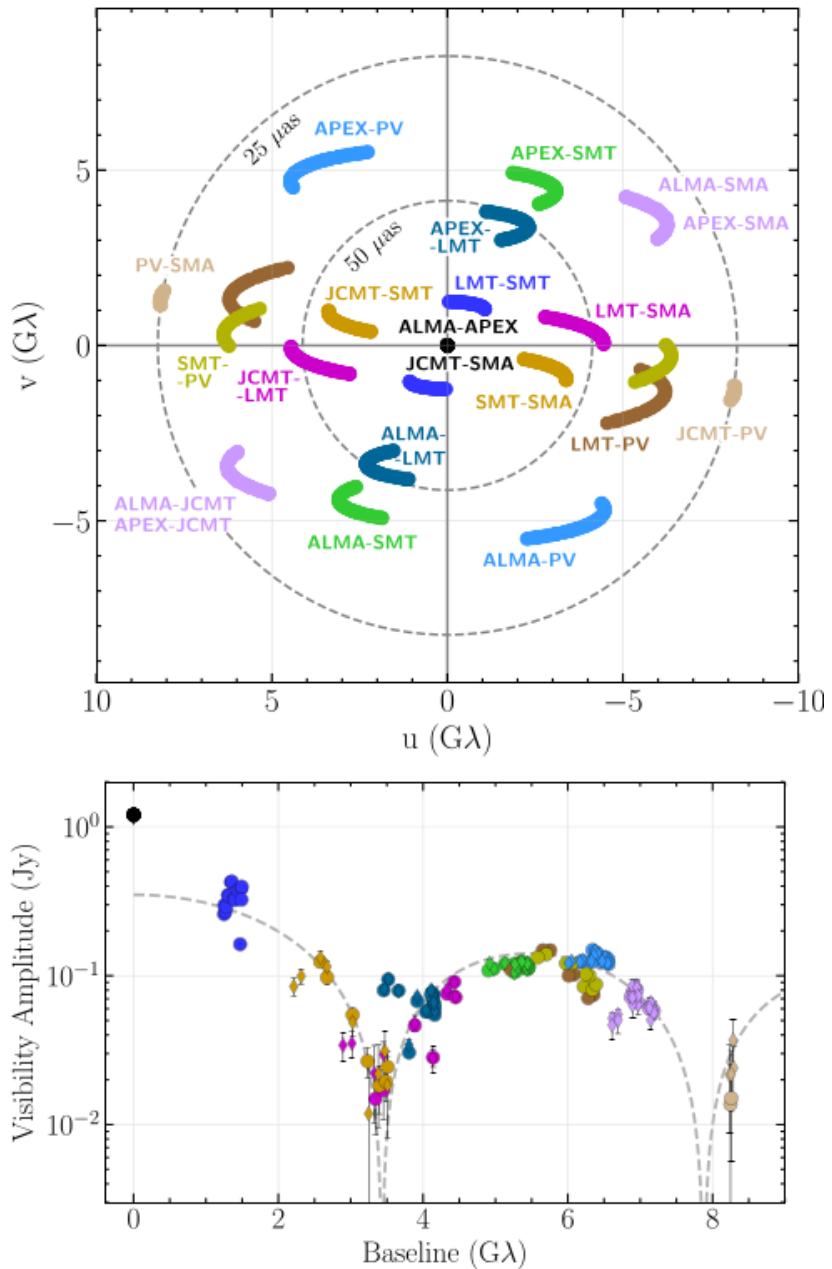


Figure 1.1: Interferometric data from the EHT observation of M87*. (top) The (u, v) -coverage obtained by using different baselines and using the rotation of the Earth. The plane is sparsely sampled, making the reconstruction of the image a challenging task. (bottom) The amplitude of the visibility. The dashed line corresponds to the Fourier transform of an azimuthally symmetric thin ring model with diameter $46 \mu\text{as}$. Figure taken from [20].

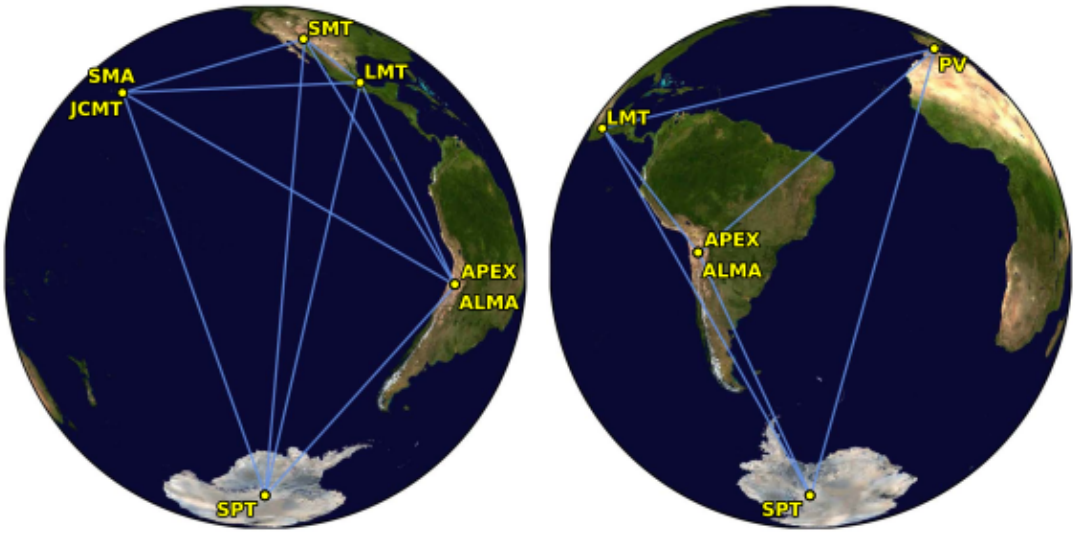


Figure 1.2: Different baselines for the 2017 Event Horizon Telescope array. Eight observatories across six locations work together to produce the first ever images of black holes. Figure taken from [28].

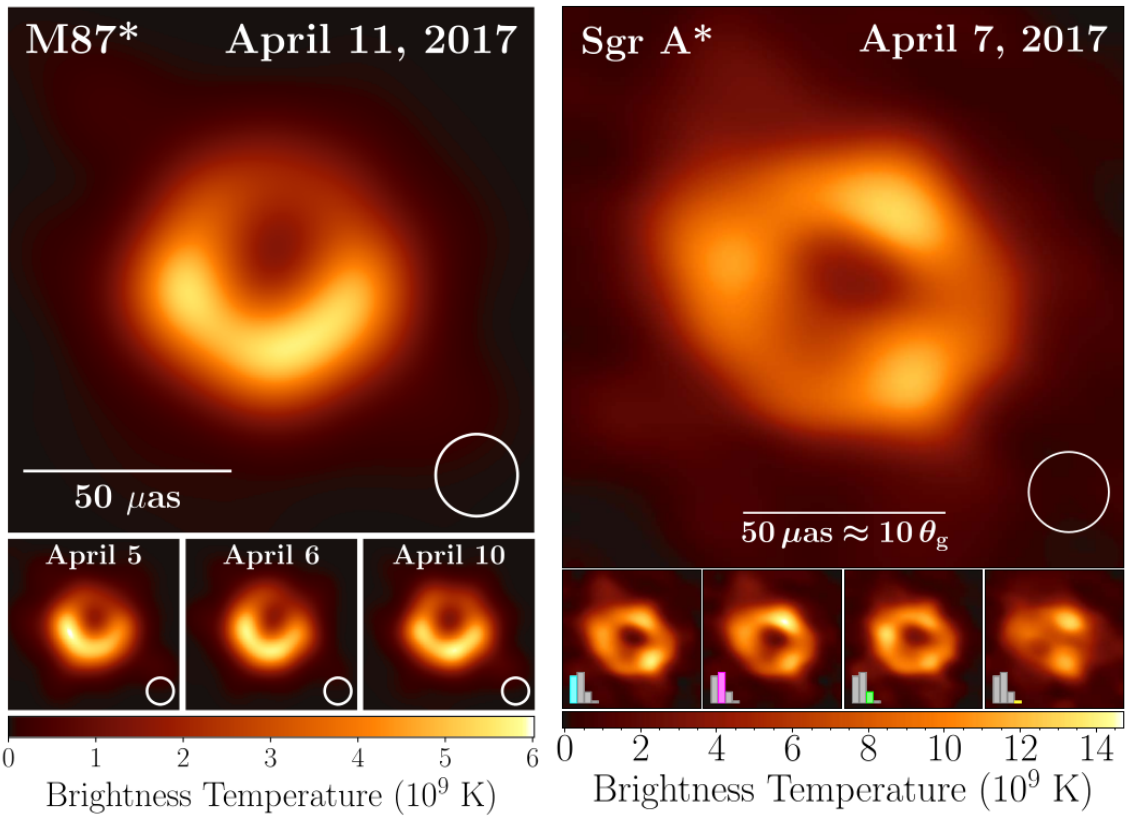


Figure 1.3: Images of (*left*) M87* as obtained on different days and (*right*) Sgr A* as taken by the Event Horizon Telescope. The small pictures below the latter do *not* correspond to different snapshots of the SMBH, but to average images within subsets of reconstructed images with similar morphology. The color denotes the specific intensity, in units of brightness temperature. This is (*left*) Figure 3 in [20] and (*right*) Figure 3 in [28].

observation, as astronomers at the time were wondering whether galactic nuclei contain central SMBHs. The benefit of these studies is that the mass of Sgr A* was already constrained very well before the EHT campaign, providing a powerful consistency check. Recently, the EHT collaboration has published their first results on Sgr A* [28–33]. The method is similar to that of M87*, with the added difficulty of the variability from the emission of the hot plasma around Sgr A*. The EHT estimated the central mass to be $4.0^{+1.1}_{-0.6} \cdot 10^6 M_\odot$, which is a factor 1000 smaller than the estimate for M87*. Because of this large difference, the variability timescale associated with the time it takes to orbit the SMBH at the innermost stable circular orbit (ISCO) is much smaller. This timescale is on the order of 4-30 minutes for Sgr A*, meaning that its appearance can change significantly during an observation. This is not an issue for M87*, where this timescale is on the order of 5-30 days. Therefore, time-averaging data is much more challenging for Sgr A*. This translates to a larger uncertainty compared with the estimates for M87*, also partially due to the uncertainty associated with the inclination of Sgr A*. No prior restrictions on the inclination were present, due to the lack of an emission jet, but in general the simulations seem to favor inclinations below 50° .

The main conclusion is once again that the Sgr A* data are consistent with the Kerr metric. This time, however, an entire paper [33] is devoted to comparing the data with the predictions of alternative descriptions of the spacetime around Sgr A*. On the one hand, the data is compared to sets of images generated by different black hole metrics. For example, the team considered metrics that deviate in a continuous way from Kerr (e.g. the Johannsen-Psaltis metric [63] and the Modified Gravity (MGBK) metric [87]). Their observations are used to put bounds on the different parameters in these Kerr-like spacetimes. On the other hand, they investigate the possibility that the data can be explained by an exotic compact object. Several exotic models are strongly disfavoured, based on the simulations produced by the team.

It should be noted however that, at the current resolution, the data obtained by the EHT is unlikely to put stringent bounds on the geometry describing these SMBHs [48]. Testing predictions of the theory that are independent of astrophysical effects, like the photons rings we discuss in section 4.2, will likely require a space mission.

The estimated masses of M87* and Sgr A* differ by a factor of order 1000. Combined with results for stellar-mass black holes as obtained from gravitational wave observations, it is impressive that the predictions of GR hold so well over this enormous range of 9 orders of magnitude in mass. The images obtained by the EHT are the result of an enormous collective effort of scientists all over the world. They have opened the door to the investigation of BHs at the horizon scale, complementary to gravitational wave studies. As of now, the angular resolution is not sufficient to perform accurate tests of GR, but increasing the resolution in the future may expose the near-horizon scales at which GR starts to break down.

1.3 Features in black hole images

In this section, we take a brief look at two features that are present in (simulated) images of BHs; the black hole shadow and the photon rings. We defer a detailed explanation to Chapter 4, but present a qualitative picture in this section, along with some recent publications to motivate the in-depth study of both concepts.

Predicting the appearance of an astrophysical black hole to a distant observer dates back to 1972 [6]. In 1978, Luminet produced the first simulation of what a BH with a surrounding accretion disk would look like: a marvelous picture which can be found in [70]. Since then, simulation techniques have become more sophisticated, including all the effects of GR and magnetohydrodynamics (MHD). Consider the left image in Figure 1.4. It displays a time-averaged simulation of a model for M87*, of which the details are not important to understand the essential ideas. Ideally, this is what Figure 1.3 would look like (at a specific wavelength) if the resolution of the EHT were much higher. The simulation boasts a very bright ring-like structure, nested in a diffuse ring of lower brightness. The latter is a direct view of the accretion disk that surrounds the central BH. The bright ring actually contains an even brighter, yet even thinner ring. These are two *photon rings*, which belong to a theoretical, infinite sequence of self-similar rings that decrease rapidly in width (such that the third ring can't even be distinguished in picture). These rings arise from complicated lensing patterns, as will be explained in section 4.2. The second and smallest ring approximates what is called *the critical curve*, marking the edge of the black hole *shadow*. The shadow is essentially the result of the fact that some photons cannot escape the gravitational pull of the black hole, and will be explained in more detail in section 4.1. We will study both the shadow and photon rings in this project, for two non-Kerr metrics. This is an active field of study, and below we provide some recent results in the literature.

The black hole shadow is a first step in determining how an observer sees a black hole. The calculations that we present in 4.1 have been carried out for a number of different metrics. Extensive research has been performed on the Kerr shadow [6, 52], which is well understood. The shadow of non-Kerr metrics has been determined for e.g. the Johannsen-Psaltis metric [2] or more generally for any rotating spacetime that can be obtained through the Newman-Janis algorithm [78]. The exercise has also been made [60] for the Johannsen metric as we use it throughout this thesis (see sections 2.2.3 and 4.1.2). As another example, [35] considers the evolution of a Kerr shadow as a result of superradiance, which is a possibility to search for ultra-light scalar fields around black holes.

However, the shadow of a black hole is subject to a large degree of degeneracy, meaning that the shadows of different metrics can be very alike. As an example, [65] constructs two metrics which have the *exact* same shadow as a Kerr BH. This limits the usefulness of the shadow as observable, yet it provides a natural starting point to study the photon rings.

In this project, we will mainly focus on the **Lyapunov exponent** γ associated with the

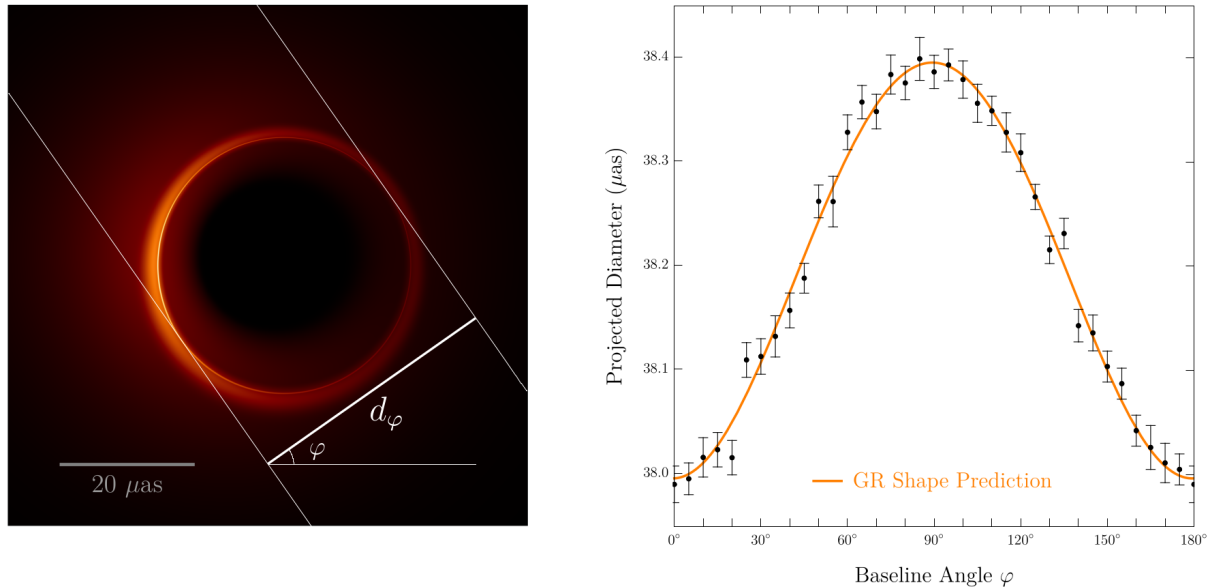


Figure 1.4: (*left*) A time-averaged simulation of M87*, which clearly shows the photon rings as the bright ring-like features. The distance d_ϕ represents the projected diameter of the second photon ring at different angles ϕ . (*right*) An example of the predicted shape of d_ϕ versus ϕ , as based on a Kerr black hole. The data points are forecasted experimental results. Figure taken from [53].

photon rings. This quantity determines the relative widths of subsequent rings, as explained in 4.2. The main benefit of the photon rings is that they provide clues about the underlying spacetime irrespective of astrophysics and the model for the accretion disk. The Lyapunov exponent is not studied as extensively as the shadow, even though this is likely to provide very accurate tests with interferometric data.

The photon rings conveniently produce strong signatures in interferometric measurements [64]. Regular telescopes are mostly sensitive to the flux, which makes it incredibly hard to dissolve the intricate substructure of the rings as the flux decreases exponentially with each ring. The benefit of interferometry is that it is inherently also very sensitive to distinct spatial wavenumbers. This means that, even though the subrings provide a negligible contribution to the total flux, they can produce a pronounced signal on long interferometric baselines. Given that the EHT collaboration has obtained their images using interferometry, this provides a promising method of measuring at least the first few photon rings. Figure 1.4 shows a proposed test based on the width of the photon rings in all directions [53]. Given the strong interferometric signatures that the photon rings can provide, the authors claim that a space-based test can conduct this experiment to test the GR prediction of the photon ring shape with a precision of 0.04%.

In addition to γ , two more critical parameters that determine the nested sequence of lensed images are identified for the Kerr metric [50]. They are denoted by δ and τ , controlling the rotation and time delay of the successive images respectively. They can be calculated analytically for Kerr, in a similar fashion as we will do for γ in the section 4.3.

Together, they govern the nearly-bound geodesics that make up the photon rings.

Last year, another observable associated with these photon rings has been put forward. Given the strong lensing effects in the vicinity of the black hole, light sources can connect to an observer along multiple distinct paths (see Figure 4.11). It is therefore expected that variations in the observed brightness are correlated across different times and positions on the observer screen. The new observable studied in [54] is the two-point correlation function (2PF) of intensity fluctuations on the photon ring. This 2PF exhibits a self-similar structure, consisting of multiple peaks, that depends universally on the underlying spacetime: the locations and heights of the peaks depend on the BH parameters, whereas the specific profile of each peak encodes statistical information about the variability in the source. The authors estimate that a measurement of this 2PF could be possible with modest improvements to the existing EHT.

Finally, another reason to study the Lyapunov exponent is that there is a nice link between the former and the so-called Quasi-Normal Modes (QNMs) in gravitational wave physics [16, 93]. These are the characteristic, resonant modes of linear perturbations on the BH spacetime satisfying certain boundary conditions. They are represented by complex frequencies $\omega = \omega_R + i\omega_I$, and it turns out that this imaginary part can be related to the Lyapunov exponent in a limiting case. We do not provide further details, but this correspondence is interesting with respect to the complementary role that gravitational waves and horizon-scale images of BHs can play in testing GR in their strong gravitational field.

In the previous sections we have motivated the study of GR in the immediate surroundings of black holes, and presented the new and exciting results that horizon-scale images can bring us. We have also introduced the specific features that we want to extract from these images, and put them in context of ongoing research. In the next section, we can finally present the research goals of this Master’s Thesis, that are worked out in the subsequent chapters.

1.4 Motivation and research objectives

With the advent of the EHT and gravitational wave observations, the possibility of studying the gravitational field around black holes on the horizon scale has become reality. This field will enable physicists to put the theory of General Relativity to test, in a regime where it may eventually break down. On the one hand, technical improvements are required to increase the resolution on the images by the EHT. On the other hand, the data has to be compared to the predictions of both GR and alternative theories. The goals of this Master’s dissertation focus on this second leg.

The main goal of the thesis is to investigate the signatures that two alternative black hole metrics would produce on horizon-scale images like the ones obtained by (an improved version of) the EHT. The motivation behind this objective is that the predictions of these

alternative descriptions of a black hole can be tested to probe possible violations of the no-hair theorem. Such violations would show that GR breaks down at some point, and could provide clues where to look beyond this theory.

Chapter 2 provides a lightning review of some essential concepts of GR, which serves as reference for the rest of the text. Afterwards, the BH spacetimes that are of relevance for this project are presented. First of all, the classical solutions of GR, the Schwarzschild and Kerr(-Newman) metric, are reviewed. Subsequently, we present the two metrics against which the Kerr solution will be compared. On the one hand, we have chosen the Johannsen metric [61], which is a metric that parametrizes certain deviations from the Kerr solution. On the other hand, we will investigate the almost-BPS black hole, as presented in [5]. The four-dimensional metric we will use is obtained from a particular supergravity theory, and is therefore a physical solution of a theory beyond GR.

Having introduced the metrics, we investigate the motion of bound null geodesics in Chapter 3. We review the existing results for the Kerr solution, and extend this analysis to the other two metrics. The results obtained in this chapter are the foundation of the following calculations.

Chapter 4 presents the two observables of interest in detail. We start by reviewing the work of Bardeen [6], deriving the apparent shape (often referred to as *the shadow*) of a Kerr black hole as seen by a distant observer. The same method is employed to derive the shadow of the Johannsen and almost-BPS black holes, and we analyze the influence of the different metric parameters on this shadow. We then turn to the photon rings that surround the BH shadow. They are a result of the severe lensing in the immediate surroundings of the BH spacetime, so that they depend heavily on the details of the metric. We investigate the Lyapunov exponent γ , associated with the relative widths of these photon rings, and present semi-analytical formulas that determine it. Once again, the effect of the metric parameters is discussed in detail by means of figures.

This analytical work is only feasible for a subset of all proposed BH metrics, namely the ones with integrable geodesic equations. To set up a framework which is more applicable to arbitrary spacetimes, we take a numerical approach in Chapter 5, where we will use a ray-tracing code to visualize the metrics of interest. We use this method to verify our analytic prediction of the BH shadow to an accuracy of a single pixel. Furthermore, we try to estimate the Lyapunov exponent from the photon rings that can be extracted from these pictures. The numerical results in this chapter are compared with the analytical values of Chapter 4.

Chapter 6 presents the overall conclusion of this project, and presents future prospects within this field of research. As part of this outlook, we present the first ever ray-traced images of BHs with a shadow that is no longer equatorially symmetric.

Chapter 2

Black Hole Metrics

This section aims to present the different black hole metrics that are of interest for this dissertation. The first section contains a brief summary of some essentials from the theory of General Relativity, with the purpose of being a reference chapter for basic concepts and notation. The next section introduces the explicit metrics, motivating their choice and relevance.

2.1 General Relativity - essentials

This section provides a lightning review of essential concepts in general relativity, in order to fix some of the notation used throughout the rest of the text. Readers who are not very familiar with Einstein's theory should consult a complete and more pedagogical introduction, e.g. [18, 56, 83]. This section does not treat the beautiful physics behind special relativity and the equivalence principle, nor does it provide a full explanation of tensor calculus; it simply presents the necessary formulas. The majority of this section is based on [18].

We are used to thinking of space and time as separate concepts. One of the essential conceptual steps in understanding GR is to drop this point of view, and to start thinking of space and time together: **spacetime** is a four-dimensional construct that encompasses both, and puts them on a more equal footing.

The central object of interest in GR is the **metric tensor** $g_{\mu\nu}$, which describes the spacetime of interest. Through this coupling of space and time, infinitely many spacetimes are possible, each with distinct properties and uses. Among these possibilities are the black hole metrics, which are the focus of this project. However, many other spacetimes exist, with some famous ones being (anti-)de Sitter space and FLRW metrics.

The indices μ, ν can take the values 0,1,2,3. The first is associated with the time-like dimension, and the others correspond to the spatial dimensions. It is important whether indices are written *up* or *down*. For example, the metric with indices down, $g_{\mu\nu}$, is called the **covariant** metric, whereas the metric with upper indices, $g^{\mu\nu}$ is called the

contravariant metric. Similarly, any covariant four-vector A_μ also has a contravariant counterpart A^μ . The metric provides the correspondence between both, as

$$A^\mu = g^{\mu\nu} A_\nu .$$

A few comments are appropriate here. First of all, the name that we give to an index, i.e. μ, ν or even α , is not important. Secondly, the formula above makes use of the **Einstein summation convention**, which dictates that repeated indices on the same side of the equality are summed over (also referred to as *contracting the indices*). Therefore, the expression above should be interpreted as

$$A^\mu = g^{\mu 0} A_0 + g^{\mu 1} A_1 + g^{\mu 2} A_2 + g^{\mu 3} A_3 .$$

This summation convention is very useful, to avoid explicitly writing all the summations that appear in formulas. The index μ is called a free index, as it appears in both sides of the equation without being summed over. Often, instead of using the numbers 0,1,2,3 the coordinates to which they refer are used as indices. Explicitly, in the case of spherical coordinates $(x^0, x^1, x^2, x^3) \equiv (t, r, \theta, \phi)$, the indices are often written as e.g. $g_{tt} \equiv g_{00}$. More rules apply to these indices, but they are not treated here.

The metric appears in the formula for the **line-element** (which is sometimes also referred to as the metric):

$$ds^2 = g_{\mu\nu}(x) dx^\mu dx^\nu . \quad (2.1)$$

The x^μ are called the coordinates, and the metric can depend on them. Coordinates are not determined uniquely, and changing them is possible if the metric is transformed along with them. This line-element determines the distance between points in spacetime. Keeping the summation convention in mind, the expression (2.1) should be interpreted as

$$ds^2 = \sum_{\mu, \nu=0}^3 g_{\mu\nu}(x) dx^\mu dx^\nu = g_{00}(x) dx^0 dx^0 + g_{10}(x) dx^1 dx^0 + \dots$$

highlighting the merit of the summation convention once again. Furthermore, it should be noted that the metric has the special property that it is *symmetric*, meaning that $g_{\mu\nu} = g_{\nu\mu}$. Arguably, the most important metric is that of **flat spacetime**. This is the metric in the absence of any mass, energy or black hole. It is often referred to as the **Minkowski metric**, and is in its simplest form written as

$$ds^2 = -c^2 dt^2 + dx^2 + dy^2 + dz^2 . \quad (2.2)$$

The constant c is the speed of light, and the coordinate t corresponds to the time. The other three coordinates can be thought of as Cartesian coordinates in a three-dimensional space. It is often written in terms of spherical coordinates:

$$ds^2 = -c^2 dt^2 + dr^2 + r^2 (d\theta^2 + \sin^2 \theta d\phi^2) . \quad (2.3)$$

This may look different, but describes the exact same flat space that is described by (2.2).

In principle one could invent any metric, but the "allowed" metrics in GR are the ones that solve the **Einstein equations**

$$R_{\mu\nu} - \frac{1}{2}Rg_{\mu\nu} = \frac{8\pi G}{c^4}T_{\mu\nu}. \quad (2.4)$$

This equation features the **Ricci tensor** $R_{\mu\nu}$ and **scalar** R on the left-hand side, which depend on the metric in a complex way. Therefore, the left-hand side describes the *geometry* - and more specifically, the *curvature* - of the spacetime. The right-hand side contains the energy-momentum tensor $T_{\mu\nu}$, which depends on the matter and energy content that is present in the spacetime. This equation has a beautiful interpretation, which can be stated as

Matter and energy curve spacetime.

The equation (2.4) reduces to the laws of Newton in the non-relativistic limit, where masses are small and speeds are small compared to the speed of light c . We will often refer to the **Einstein equations in vacuum**, which correspond to setting the energy-momentum tensor $T_{\mu\nu}$ to zero in (2.4). Contracting the indices on the left-hand side shows that these are equivalent to the equation

$$R_{\mu\nu} = 0. \quad (2.5)$$

Given the central role of the speed of light in the theory, it appears in almost every equation. In order to avoid writing it all the time, which would render equations less transparent, physicists have thought of a way to get rid of all the c 's. This is done by switching to **natural units**. Essentially, this is similar to switching from SI-units to e.g. cgs-units. The result is that we can replace every instance of c by 1. As an example, Einstein's famous equation for the rest energy E of a particle with mass m , given by $E = mc^2$, would be written as $E = m$ in natural units. There is a consistent way of recovering the original equations containing c from the ones expressed in natural units, but we will not go into these details here. To add even more complexity, the gravitational constant G can also be set to 1 along with c in a consistent way. This allows us to write equation (2.4) in natural units as

$$R_{\mu\nu} - \frac{1}{2}Rg_{\mu\nu} = 8\pi T_{\mu\nu}.$$

While the benefits of these natural units may not immediately be clear from these simple examples, the simplification they provide in more complicated formulas is significant. The main takeaway is that, as we will be using these natural units throughout the following chapters, many quantities will be expressed just in terms of the black hole mass M . Most of the time, this will correspond to distances¹, and we will refer to a radius $r = M$ as one **gravitational radius**.

¹To make this explicit, the quantity $\frac{GM}{c^2}$ has the dimensions of a length in SI units. Converting this to natural units, i.e. setting $G = c = 1$, we find that distances are given in terms of M .

The motion of test-particles is of major interest to study a certain metric. Such a test-particle has little to no mass, meaning that they have no effect on the surrounding spacetime. Its motion is governed by the **geodesic equations**

$$\frac{d^2x^\rho}{d\sigma^2} + \Gamma_{\mu\nu}^\rho \frac{dx^\mu}{d\sigma} \frac{dx^\nu}{d\sigma} = 0. \quad (2.6)$$

This equation governs the trajectory of a test-particle in spacetime. This grants another beautiful interpretation:

The curvature of spacetime dictates how matter and light move.

A trajectory that satisfies (2.6) is called a **geodesic**, and it corresponds to a generalization of "straight lines" to curved spacetimes. In the case of massive particles, σ corresponds to the proper time τ (defined as $ds^2 = -c^2 d\tau^2$), but in the case of massless particles, e.g. photons, σ is called an affine parameter. In this case, the geodesics are called **null geodesics**. In this thesis we will study the motion of light around black holes, and therefore we find ourselves studying null geodesics.

The **Christoffel symbols** $\Gamma_{\mu\nu}^\rho$ (also often called the *connection coefficients*) that appear in equation (2.6) are also present in the definition of the Ricci tensor, and are constructed from the metric as

$$\Gamma_{\mu\nu}^\rho = \frac{1}{2} g^{\rho\lambda} (\partial_\mu g_{\nu\lambda} + \partial_\nu g_{\mu\lambda} - \partial_\lambda g_{\mu\nu}). \quad (2.7)$$

In this expression we have adopted the commonly used notation $\partial_\mu = \frac{\partial}{\partial x^\mu}$.

For massive particles of mass μ , the **four-momentum** is defined as

$$p^\nu = \mu \frac{dx^\nu}{d\tau}. \quad (2.8)$$

This obeys the closing relation

$$p^\nu p_\nu = -\mu^2 c^2. \quad (2.9)$$

In the case of massless particles, the affine parameter σ is usually normalized such that

$$p^\mu = \frac{dx^\mu}{d\sigma}, \quad (2.10)$$

which obeys the closing relation (2.9) with $\mu = 0$.

Introducing the covariant derivative ∇_μ , acting on vectors as

$$\nabla_\mu A^\nu = \partial_\mu A^\nu + \Gamma_{\mu\lambda}^\nu A^\lambda, \quad \nabla_\mu A_\nu = \partial_\mu A_\nu - \Gamma_{\mu\nu}^\lambda A_\lambda, \quad (2.11)$$

we can rewrite the geodesic equation (2.6) as

$$p^\lambda \nabla_\lambda p^\mu = 0. \quad (2.12)$$

This form of the geodesic equation leads to the concept of conserved quantities. It turns out that if a vector K_μ satisfies **Killing's equation**

$$\nabla_\mu K_\nu + \nabla_\nu K_\mu = 0, \quad (2.13)$$

the quantity $K_\mu p^\mu$ is conserved along a geodesic. The vector K_μ is called a **Killing vector**, and these conserved quantities are indispensable tools to study geodesics in a particular spacetime.

2.2 Black hole metrics

This section presents the relevant BH metrics that are used during the project. First, we discuss the well-known cases of the Schwarzschild and Kerr metric in 2.2.1 and 2.2.2, largely based on [18]. The latter is the most general black hole solution of the vacuum Einstein equations (2.5) in GR. Afterwards, we present two metrics that are no longer solutions of GR in 2.2.3 and 2.2.4. The first one, called the Johannsen metric, deviates in a continuous way from the Kerr solution while retaining 3 conserved quantities associated with the geodesic motion. The second one is called the almost-BPS metric, which arises as a solution in a particular supergravity theory.

2.2.1 Schwarzschild black hole

The first black hole solution dates back to 1916, and is discovered by Karl Schwarzschild [77]. The Schwarzschild metric is usually written in the form

$$ds^2 = - \left(1 - \frac{2M}{r}\right) dt^2 + \left(1 - \frac{2M}{r}\right)^{-1} dr^2 + r^2 (d\theta^2 + \sin^2 \theta d\phi^2) \quad (2.14)$$

It is the unique spherically symmetric and asymptotically flat² solution of the vacuum Einstein equations (2.5), and one of the most important metrics overall. The spherical coordinates $\{t, r, \theta, \phi\}$ represent the time, radial coordinate, polar angle and azimuthal angle, respectively. The parameter M corresponds to the mass of the central BH, whose singularity is located at $r = 0$.

Aside from this singularity at the center, the metric poses another problem. When $r = 2M$, the component g_{rr} becomes infinite. This specific value for the radial coordinate is referred to as the Schwarzschild radius R_S . Importantly, this corresponds to the location of the event horizon, i.e. the distance below which nothing, even light, can not escape anymore. The difference with the true singularity at $r = 0$ is that the Schwarzschild radius corresponds to an *apparent singularity*: it is an artifact of the coordinate system that is used, and changing coordinates can resolve this apparent singularity. An example of these so-called horizon-penetrating coordinates are Eddington-Finkelstein coordinates, which can be found in [18].

²For large values of the radial coordinate, the metric is approximately equal to the Minkowski space-time (2.3).

2.2.2 Kerr-Newman black hole

The spherical symmetry of the Schwarzschild solution makes it relatively easy, yet unlikely to be astrophysically accurate. Objects in space typically have an angular momentum, which breaks spherical symmetry. Instead, only an axial symmetry around the rotation axis remains. Accounting for this angular momentum is quite hard, and the solution took almost 50 years after the publication of the Schwarzschild metric. Roy Kerr presented in 1963 his solution of the vacuum Einstein equations (2.5) in which he only assumed axial symmetry [67]. The result is given by

$$ds^2 = -\frac{\Delta}{\Sigma} (dt - a \sin^2 \theta d\phi)^2 + \frac{\Sigma}{\Delta} dr^2 + \Sigma d\theta^2 + \frac{\sin^2 \theta}{\Sigma} [(r^2 + a^2) d\phi - a dt]^2 \quad (2.15)$$

The coordinates are called Boyer-Lindquist (BL) coordinates, and the functions Δ and Σ are defined as

$$\Delta = r^2 - 2Mr + a^2, \quad \Sigma = r^2 + a^2 \cos^2 \theta. \quad (2.16)$$

This is the most general asymptotically flat, stationary³ solution of the vacuum Einstein equations (2.5) in GR. The parameter M still represents the mass of the black hole, and a is the angular momentum per unit mass, $a = J/M$, which we will usually simply refer to as the 'spin'. J is the angular momentum of the BH.

Setting the angular momentum equal to zero, we would expect to recover the Schwarzschild metric. This is indeed the case, as can be explicitly checked by setting $a = 0$. The solution can be extended to solve the Einstein-Maxwell equations, which describe a combination of GR and the Maxwell equations of electromagnetism. However, the energy-momentum tensor in this case is non-zero because of the electromagnetic fields and the full Einstein equations (2.4) must be solved. We will not go into the details, but the result can be obtained from (2.15) by replacing Δ in (2.16) by

$$\Delta = r^2 - 2Mr + a^2 + q^2. \quad (2.17)$$

The parameter q corresponds to the electric charge⁴, and the metric is now referred to as the Kerr-Newman (KN) metric. In the case of non-zero electric charge but zero angular momentum, the metric is called the Reissner-Nordström (RN) metric.

As in the case of the Schwarzschild metric, there is a coordinate singularity when the g_{rr} component of the metric, which is equal to $\frac{\Sigma}{\Delta}$, becomes infinite (Note that $\Sigma > 0$). This is the case when $\Delta = 0$. Solving this for r based on the expression (2.17) gives the result

$$r_{\pm} = M \pm \sqrt{M^2 - a^2 - q^2}. \quad (2.18)$$

So, we find that the KN metric has 2 event horizons when $a^2 + q^2 < M^2$. In the case of equality, both event horizons coincide: we refer to this as the BH being extremal. We recover the Schwarzschild radius when a and q are both equal to zero, and in this case the inner event horizon coincides with the true singularity. In the case $a^2 + q^2 > M^2$,

³This means that the metric components are independent of time.

⁴Sometimes, a magnetic charge p is included as well by replacing q^2 with $q^2 + p^2$.

there are no event horizons. This means that the singularity is *naked*, violating the *cosmic censorship conjecture*. We will not consider this case. The double event horizon has many interesting properties, but for our purposes in the following chapters we can just focus on the outer horizon r_+ . Aside from the event horizons, the KN metric has other interesting properties, like the ergosphere around the outer horizon.

The metric admits two Killing vectors, because the metric components are independent of the coordinates t and ϕ . They are given by $K^\mu = (1, 0, 0, 0)$ and $R^\mu = (0, 0, 0, 1)$, which provide two conserved quantities for the geodesics: the energy E and the angular momentum L . This is a general property of stationary, axisymmetric metrics.

So far, we have described both the Schwarzschild and Kerr metrics as representing BHs. However, they can also be used as an approximate model for the spacetime around e.g. stars and neutron stars. They can only model the spacetime away from the surface and interior, as the solutions are obtained in vacuum. The spacetime in the interior requires a different approach, but is not relevant in many applications.

Looking back at section 1.1, we emphasize once again that the most general description of a BH in GR (combined with the Maxwell equations) is given by this Kerr(-Newman) metric. In the next two sections we present two BH spacetimes that go beyond the theory of general relativity. Considering these metrics within the framework of GR means that they must have some pathologies⁵, or require an additional source in the energy-momentum tensor.

2.2.3 Johannsen metric

In order to test the no-hair theorem, several spacetimes that deviate continuously from KN have been proposed and analysed. A change in observables caused by these deviations is interesting to use in a null-hypothesis test that focuses on violations of the no-hair theorem. The goal of [61] was to construct a metric that deviates from the Kerr spacetime, while retaining four constants of the geodesic motion. This facilitates the analytical calculations, because the geodesic equations can be written in first-order form (also referred to as *being integrable*). The metric is used on many occasions in the literature, underlying its relevance [33, 76, 85]. It extends the idea of the Johannsen-Psaltis metric proposed in [63], which is also studied extensively.

The calculation in the original paper [61] is briefly summarised below. For a full account, the reader is referred to the original paper.

⁵Pathologies refer to certain problems that a metric can have, like a violation of the Lorentzian signature of the metric or closed timelike curves. The latter would enable an observer to meet him-/herself in the past.

Construction of the Johannsen metric

The goal is to create a stationary, axisymmetric and asymptotically flat metric that describes spinning black holes and provides four independent constants of motion. It deviates continuously from the Kerr metric, through deviation functions with an arbitrary number of parameters. It reduces to Kerr when all deviation parameters are set to zero.

Our starting point is the Hamilton-Jacobi (HJ) equation

$$-\frac{\partial S}{\partial \tau} = \frac{1}{2} g^{\alpha\beta} \frac{\partial S}{\partial x^\alpha} \frac{\partial S}{\partial x^\beta}, \quad (2.19)$$

where τ represents the proper time. Recall first that stationary and axisymmetric metrics admit at least three constants of motion. The conserved energy E and the axial angular momentum L are a result of the metric being stationary and axisymmetric, respectively. Furthermore, the normalization $p^\mu p_\mu = \mu^2$ for a test-particle of mass μ provides a third constant of motion. Finding the fourth constant of motion is much less straightforward. Carter found the solution by assuming a Hamilton-Jacobi function of the form [19]

$$S = \frac{1}{2} \mu^2 \tau - Et + L\phi + S_r(r) + S_\theta(\theta). \quad (2.20)$$

He showed that this function makes the HJ equation (2.19) separable, resulting in an additional constant of motion. To demonstrate the separability, we calculate the contravariant form of the Kerr metric (2.15)

$$\begin{aligned} g^{\alpha\beta} \frac{\partial}{\partial x^\alpha} \frac{\partial}{\partial x^\beta} &= -\frac{1}{\Delta\Sigma} \left[- (r^2 + a^2) \frac{\partial}{\partial t} + a \frac{\partial}{\partial \phi} \right]^2 + \frac{1}{\Sigma \sin^2 \theta} \left[\frac{\partial}{\partial \phi} - a \sin^2 \theta \frac{\partial}{\partial t} \right]^2 \\ &+ \frac{\Delta}{\Sigma} \left(\frac{\partial}{\partial r} \right)^2 + \frac{1}{\Sigma} \left(\frac{\partial}{\partial \theta} \right)^2 \end{aligned} \quad (2.21)$$

and use this together with (2.20) in (2.19) to find

$$\begin{aligned} -\Sigma \mu^2 &= -\frac{1}{\Delta} \left[- (r^2 + a^2) E + aL \right]^2 + \Delta \left(\frac{\partial S_r}{\partial r} \right)^2 \\ &+ \frac{1}{\sin^2 \theta} \left[L - aE \sin^2 \theta \right]^2 + \left(\frac{\partial S_\theta}{\partial \theta} \right)^2. \end{aligned} \quad (2.22)$$

The function Δ depends only on r , and if we use the expression (2.16) for Σ , we see that we can indeed separate this equation in a part that depends only on r and a part that depends only on θ . Therefore, both parts must be equal to a constant, since r and θ can vary independently. This allowed Carter to define a constant k as

$$k = -r^2 \mu^2 + \frac{1}{\Delta} \left[- (r^2 + a^2) E + aL \right]^2 - \Delta \left(\frac{\partial S_r}{\partial r} \right)^2, \quad (2.23)$$

$$k = a^2 \mu^2 \cos^2 \theta + \frac{1}{\sin^2 \theta} \left[L - aE \sin^2 \theta \right]^2 + \left(\frac{\partial S_\theta}{\partial \theta} \right)^2. \quad (2.24)$$

The quantities $\frac{\partial S_r}{\partial r}$ and $\frac{\partial S_\theta}{\partial \theta}$ correspond to the momentum components p_r and p_θ , respectively. Instead of the constant k , one can also define the *Carter constant* $Q = k - (L - aE)^2$.

This is the fourth constant of motion, required to ensure the integrability of the geodesic equations.

The goal is now to extend this metric such that we can still separate the HJ equations in order to find this Carter constant. To do so, we have a look at (2.21) and note that we could insert some scalar functions depending on either r or θ , depending on which of the two separated parts they will end up in. It is the structure of the contravariant metric that in the end dictates whether we still have separability. We define functions $f(r), g(\theta), A_i(r), A_j(\theta)$ with $i = 1, 2, 5$ and $j = 3, 4, 6$, and define a new metric by⁶

$$g_J^{\alpha\beta} \frac{\partial}{\partial x^\alpha} \frac{\partial}{\partial x^\beta} = -\frac{1}{\Delta \tilde{\Sigma}} \left[-A_1(r) (r^2 + a^2) \frac{\partial}{\partial t} + A_2(r) a \frac{\partial}{\partial \phi} \right]^2 + \frac{1}{\tilde{\Sigma} \sin^2 \theta} \left[A_3(\theta) \frac{\partial}{\partial \phi} - A_4(\theta) a \sin^2 \theta \frac{\partial}{\partial t} \right]^2 \quad (2.25)$$

$$+ A_5(r) \frac{\Delta}{\tilde{\Sigma}} \left(\frac{\partial}{\partial r} \right)^2 + A_6(\theta) \frac{1}{\tilde{\Sigma}} \left(\frac{\partial}{\partial \theta} \right)^2, \quad (2.26)$$

where $\tilde{\Sigma} = \Sigma + f(r) + g(\theta)$. The rest of the analysis is now exactly the same. Due to the choice of deviation functions, the HJ equations are still separable by construction, and a fourth conserved quantity can be found. We will refer to this constant as Carter constant as well.

However, this is not the end. If we want the metric to be asymptotically flat, the deviation functions can not be chosen arbitrarily. It turns out⁷ that this implies that the functions $A_j(\theta)$ must be equal to 1. Expanding the functions $A_i(r)$ as a power series in M/r

$$A_i(r) = \sum_{n=0}^{\infty} \alpha_{in} \left(\frac{M}{r} \right)^n,$$

the constraint of asymptotic flatness requires the first terms in these sums to be $\alpha_{i0} = 1$. Additional subtleties result in $g(\theta)$ being equal to zero, as well as α_{i1} and α_{12} . Finally, $f(r)$ is expanded as

$$f(r) = \sum_{n=3}^{\infty} \epsilon_n \frac{M^n}{r^{n-2}}.$$

In this thesis we will not consider the infinite sums as presented above, but only their leading order corrections to the Kerr metric. From the contravariant metric (2.25), the covariant metric can be obtained. In the end, the Johannsen metric as we will use it in this project reads

⁶As T. Johannsen indicates in his paper, this may not be the most general way to extend the Kerr metric and keep the separability, as one could also introduce functions that depend on both variables and still preserve separability. The choice here however is the most general one when the deviation functions depend only on 1 variable.

⁷We will not go in the details here, but they can be found in the original paper [61].

$$\begin{aligned}
ds^2 = & -\tilde{\Sigma} \frac{\Delta - a^2 A_2(r)^2 \sin^2 \theta}{[(r^2 + a^2) A_1(r) - a^2 A_2(r) \sin^2 \theta]^2} dt^2 + \frac{\tilde{\Sigma}}{\Delta A_5(r)} dr^2 + \tilde{\Sigma} d\theta^2 \\
& - 2a\tilde{\Sigma} \sin^2 \theta \frac{(r^2 + a^2) A_1(r) A_2(r) - \Delta}{[(r^2 + a^2) A_1(r) - a^2 A_2(r) \sin^2 \theta]^2} dt d\phi \\
& + \tilde{\Sigma} \sin^2 \theta \frac{(r^2 + a^2)^2 A_1(r)^2 - a^2 \Delta \sin^2 \theta}{[(r^2 + a^2) A_1(r) - a^2 A_2(r) \sin^2 \theta]^2} d\phi^2,
\end{aligned} \tag{2.27}$$

where

$$\begin{aligned}
A_1(r) &= 1 + \alpha_{13} \left(\frac{M}{r} \right)^3, \\
A_2(r) &= 1 + \alpha_{22} \left(\frac{M}{r} \right)^2, \\
A_5(r) &= 1 + \alpha_{52} \left(\frac{M}{r} \right)^2, \\
\tilde{\Sigma} &= r^2 + a^2 \cos^2 \theta + f(r), \\
f(r) &= \epsilon_3 \frac{M^3}{r}.
\end{aligned}$$

This new metric depends on four additional parameters: α_{13} , α_{22} , α_{52} and ϵ_3 . The latter will not be of much interest, since we will only consider null geodesics in what follows. Equation (2.22) shows that Σ , and therefore $\tilde{\Sigma}$, is coupled only to μ , which is zero in the case of null geodesics.

Properties of the Johannsen metric

By construction, the metric is stationary, asymptotically flat, axisymmetric and reduces continuously to Kerr when the deviation parameters go to zero. It is also shown in the paper that the event horizon of the new black hole coincides with that of the Kerr black hole (2.18).

There are some bounds on the parameters, that we can derive by demanding regularity of the exterior domain [62]. It is possible that the deviation functions introduce singularities or other pathologies, like a violation of Lorentzian signature or the existence of closed timelike curves. Avoiding these problems will give us restrictions on the parameters that are present in the first order deviation functions of the Johannsen metric.

First of all, we note that g_{rr} is proportional to $1/A_5(r)$. This leads us to impose the requirement $A_5(r) > 0$ outside the horizon, to avoid creating additional singularities. In terms of the first-order parameter, this bound gives

$$\alpha_{52} > -\frac{r_\pm^2}{M^2}. \tag{2.28}$$

Additionally, we want to make sure that the determinant of the metric itself is negative definite to maintain the Lorentzian signature outside the horizon. The determinant is given by

$$\det(g_{\mu\nu}) = -\frac{\tilde{\Sigma}^4 \sin^2 \theta}{A_5(r) [A_1(r)(r^2 + a^2) - a^2 A_2(r) \sin^2 \theta]^2}. \quad (2.29)$$

This clearly cannot be positive, and demanding that it remains finite requires

$$A_1(r)(r^2 + a^2) - a^2 A_2(r) \sin^2 \theta \neq 0. \quad (2.30)$$

In terms of the first-order deviation parameters, this is explicitly rewritten as

$$\alpha_{13} \neq \frac{a^2 r (r^2 + \alpha_{22} M^2) \sin^2 \theta - r^3 (r^2 + a^2)}{M^3 (r^2 + a^2)}. \quad (2.31)$$

Furthermore, we want to avoid closed timelike curves in the exterior domain. This corresponds to avoiding that the $g_{\phi\phi}$ element of the metric is negative. This requires that for all θ, r outside the horizon $\tilde{\Sigma} > 0$ and

$$\begin{aligned} A_1(r)^2 (r^2 + a^2)^2 - a^2 \Delta \sin^2 \theta &> 0 \\ \Leftrightarrow A_1(r)^2 (r^2 + a^2)^2 - a^2 \Delta &> 0. \end{aligned}$$

To lowest order, we can rewrite both as

$$\begin{aligned} \epsilon_3 &> -r \frac{r^2 + a^2 \cos^2 \theta}{M^3}, \\ \alpha_{13} &> \frac{r^3}{M^3} \frac{a^2 \Delta - (r^2 + a^2)^2}{(r^2 + a^2)^2} \end{aligned}$$

These have to hold for all $r > r_+$. Therefore, the first condition becomes

$$\epsilon_3 > -\frac{r_+^3}{M^3}, \quad (2.32)$$

while the second one reduces to⁸

$$\alpha_{13} > -\frac{r_+^3}{M^3}. \quad (2.33)$$

It is also interesting to investigate (2.31) for the case that only one of the parameters is non-zero [84]. In the case that $\alpha_{13} = 0$, we can rewrite this condition as

$$\alpha_{22} < \frac{r_+^4}{a^2 M^2}. \quad (2.34)$$

In the case where $\alpha_{22} = 0$ we find the bound

$$\alpha_{13} > -\frac{r_+^4}{2M^4}. \quad (2.35)$$

This is somewhat more restrictive than the bound (2.33).

⁸The author derives a lower bound on α_{22} as well, which is stated to follow from (2.33) and (2.31). However, a lower bound does not follow from these equations.

2.2.4 Almost-BPS black hole

The second black hole metric beyond GR that we study in this dissertation is one that finds its origin in *supergravity*⁹. It is presented in [5], which is the main reference for what follows.

Once again, the metric describes a spinning black hole, which is now also extremal (meaning that it has zero temperature) and non-supersymmetric. This second property is reflected in the name: almost-BPS refers to the Bogomol'nyi–Prasad–Sommerfield (BPS) bound, which is a bound that is satisfied by supersymmetric solutions. The black hole in this section does not fulfill this requirement, and is therefore not supersymmetric. However, as the name suggests, this is *almost* the case. The name applies to solutions that satisfy the BPS-bound locally, but not globally. The benefit is that the associated equations of motion remain of first order, which is not the case for general non-supersymmetric solutions [47].

In contrast to their supersymmetric cousins, which are non-rotating and carry very large charges, the geometries studied in this section can have angular momentum and smaller charges. This makes these almost-BPS solutions more phenomenologically relevant.

The BH that we consider here is originally constructed in [10], but [5] added the parameter h which has interesting consequences. The four-dimensional metric is given by

$$ds^2 = -\frac{\rho^2}{\Delta} \left(dt - \alpha \frac{\sin^2 \theta}{\rho} d\phi \right)^2 + \Delta \left[\frac{d\rho^2}{\rho^2} + d\theta^2 + \sin^2 \theta d\phi^2 \right], \quad (2.36)$$

where Δ is the *warp factor*, defined by

$$\begin{aligned} \Delta &= \rho^2 \sqrt{VZ_1Z_2Z_3 - \mu^2 V^2}, \\ Z_I &= \frac{1}{h} + \frac{Q_I}{\rho} \quad (I = 1, 2, 3), \\ V &= h + \frac{Q_0}{\rho}, \\ \mu V &= m_\infty + \alpha \frac{\cos \theta}{\rho^2}. \end{aligned} \quad (2.37)$$

This metric is given in isotropic coordinates, where the horizon is located at $\rho = 0$. Outside this horizon, the radial coordinate ρ increases to $+\infty$. The expression for μV tells us that this metric is not symmetric with respect to the equatorial plane, which was the case for the BHs that we have encountered so far. We will see this explicitly in the ray-traced images of Chapter 5.

⁹The relevant theory of supergravity is beyond the scope of this research, and will therefore not be discussed. The interested reader can however take on the challenge of working through [42], which is an excellent presentation of this beautiful physical theory - which in itself is a low-energy limit of string theory. The theory that relates to this section is $\mathcal{N} = 2$ four-dimensional supergravity.

We want the warp factor to be real in order to have a physical solution. A necessary condition is that the product $VZ_1Z_2Z_3$ is strictly positive if $\mu V \neq 0$. This means that the functions V, Z_I cannot have zeroes for $\rho > 0$. This means that h and Q_0, Q_I must all have the same sign, since ρ takes on all positive values. Without loss of generality, we take all these signs to be positive.

We also want to impose asymptotic flatness on this metric, which requires $\Delta \rightarrow \rho^2$ as $\rho \rightarrow \infty$. This comes down to relating the parameters m_∞ and h as

$$h^{-2} - m_\infty^2 = 1. \quad (2.38)$$

The mass M and angular momentum J of the black hole can be obtained from the asymptotical behaviour, and are equal to

$$M = \frac{Q_0 + h^2(Q_1 + Q_2 + Q_3)}{4h^3}, \quad J = -\frac{\alpha}{2}. \quad (2.39)$$

Furthermore, the event horizon at $\rho = 0$ has the topology of an S^2 -sphere, with horizon area equal to

$$A_H = 4\pi\sqrt{Q_0Q_1Q_2Q_3 - \alpha^2}. \quad (2.40)$$

From this expression we see that we have a bound on the charges given a value for the spin α :

$$Q_0Q_1Q_2Q_3 > \alpha^2. \quad (2.41)$$

In what follows, we will often write $\mathbf{Q} \equiv (Q_0, Q_1, Q_2, Q_3)$.

The expressions (2.39) show that the mass depends on the charges and h . In what follows, we will always assume $M = 1$ black holes, to facilitate comparison between different metrics and sets of parameters. To avoid intricate fine-tuning between the different charges and h , we will proceed as follows:

1. We pick simple values for the charges Q_Λ ($\Lambda \in \{0, 1, 2, 3\}$) and the spin parameter α such that (2.41) is satisfied. We also pick a value for h .
2. We calculate the original mass M^* based on our choice of parameters according to (2.39).
3. We rescale the charges as $Q_\Lambda \rightarrow Q_\Lambda/M^*$. As a result, the mass based on these rescaled charges and the original choice for h is now equal to 1.
4. In order to avoid violating the condition (2.41), we rescale $\alpha \rightarrow \alpha/(M^*)^2$.

As it is usually easier to compare the parameters before rescaling, we will introduce the *rescaling factor* ζ as follows: starting from a set \mathbf{Q}, α, h we will denote the rescaled parameters as

$$\mathbf{Q}\zeta, \alpha\zeta^2, h.$$

From the discussion above, it follows of course that $\zeta = 1/M^*$, i.e. the inverse of the mass before rescaling.

As stated before, the almost-BPS black hole is a solution to a specific four-dimensional supergravity theory. The Lagrangian of this theory does not only contain the metric, but includes four vector gauge fields \mathcal{A}^Λ and three complex scalar fields z^I as well. The gauge fields give rise to the charges, of which Q_0 is magnetic and the Q_I are electric. All these fields are coupled to each other in an intricate way. The result is that the energy-momentum tensor is non-zero for the almost-BPS metric, meaning that it is not a solution of the vacuum Einstein equations and therefore not subject to the no-hair theorem.

The authors have added the parameter h in [5] to dial the ratio of the charges versus the mass. This makes it possible to create extremal black holes with very small charges. Furthermore, the parameter h also influences the relative size of the horizon with respect to the mass. The horizon area can be made very small by taking small values of h . We will come back to this in Chapter 4, as Figure 4.9 shows that the black hole shadow becomes small for small values of h as well. Another interesting feature of the parameter h is that setting $h = 1$ results in the *purest spinning black hole*. The reason is that almost all multipoles, except M_0 and S_1 , vanish. We do not discuss this in detail, but they can be found in the paper itself.

Chapter 3

Geodesic Motion in Black Hole Spacetimes

In this chapter we will discuss bound geodesics in some of the different spacetimes we introduced in the previous chapter. This will be useful in Chapter 4, when we will investigate geodesics that deviate slightly from the bound ones we consider here. We present the relevant analysis for the Kerr metric in section 3.1, largely based on [66]. Subsequently we extend the ideas to the Johannsen and almost-BPS metrics in sections 3.2 and 3.3, which are mostly novel derivations. Many of the analytic results are obtained with *Mathematica* 12.

3.1 Bound geodesics in the Kerr metric

We will start by taking a closer look at the geodesic motion in the Kerr metric (2.15), using the approach from [66]. As is always the case when trying to describe geodesics, conserved quantities of the geodesic motion are of great use. In general, we can always employ the relation (2.9) which gives us a first conserved quantity. As discussed in section 2.2.2, the Kerr metric admits two conserved quantities associated with the independence of the metric components of t and ϕ : these are the standard angular momentum $L \equiv p_\phi$ and the energy $E = -p_t$. The Carter constant, discussed in section¹ 2.2.3 provides an additional conserved quantity. We will work here both with k as in (2.24) and Q itself, and refer to both as Carter constant.

Consider a geodesic for a massless particle, with momentum given by (2.10). We now define two new functions, $\mathcal{R}(r)$ and $\Theta(\theta)$ as follows:

$$p \equiv p_\mu dx^\mu = -E dt \pm_r \frac{\sqrt{\mathcal{R}(r)}}{\Delta} dr \pm_\theta \sqrt{\Theta(\theta)} d\theta + L d\phi. \quad (3.1)$$

¹There is actually an alternative way of finding this conserved quantity: In a similar way as we defined Killing vectors in (2.13), we can define a Killing tensor $K_{\mu\nu}$ as one that satisfies $\nabla_{(\lambda} K_{\mu\nu)} = 0$. Such a non-trivial Killing tensor is known for the Kerr metric, and the associated conserved quantity $K^{\mu\nu} p_\mu p_\nu$ is equal to k . [66]

The \pm signs here are to allow for both signs of the momentum component. From the expression for the Carter constant (2.24) we find that

$$\Theta(\theta) \equiv p_\theta^2 = k - a^2\mu^2 \cos^2 \theta - [L \csc \theta - aE \sin \theta]^2 . \quad (3.2)$$

Furthermore, the relation (2.9) with $\mu = 0$ gives

$$\mathcal{R}(r) \equiv \Delta^2 p_r^2 = [E(r^2 + a^2) - aL]^2 - \Delta(k + \mu^2 r^2) . \quad (3.3)$$

We will refer to these two functions as the angular and radial potential, respectively. They describe the radial and polar motion of the geodesic, and are positive by definition. They must be investigated in order to know how the geodesics behave, and are thus the central objects of interest in this chapter.

From the p_μ as defined above, one can raise the indices with the contravariant metric (2.21) to obtain the equations²

$$\Sigma \frac{dr}{d\sigma} = \pm_r \sqrt{\mathcal{R}(r)} , \quad (3.4)$$

$$\Sigma \frac{d\theta}{d\sigma} = \pm_\theta \sqrt{\Theta(\theta)} . \quad (3.5)$$

One can now see that

$$\pm_r \frac{1}{\sqrt{\mathcal{R}(r)}} \frac{dr}{d\sigma} = \frac{1}{\Sigma} = \pm_\theta \frac{1}{\sqrt{\Theta(\theta)}} \frac{d\theta}{d\sigma} ,$$

which we can integrate along the geodesic from $\sigma = \sigma_i$ to $\sigma = \sigma_f$. This corresponds to the coordinates $(t_i, r_i, \theta_i, \phi_i)$ and $(t_f, r_f, \theta_f, \phi_f)$, respectively. This gives

$$\int_{\sigma_i}^{\sigma_f} \pm_r \frac{1}{\sqrt{\mathcal{R}(r)}} \frac{dr}{d\sigma} d\sigma = \int_{\sigma_i}^{\sigma_f} \pm_\theta \frac{1}{\sqrt{\Theta(\theta)}} \frac{d\theta}{d\sigma} d\sigma .$$

The slash through the integral indicates that it is evaluated along the geodesic, meaning the integral increases monotonically along the trajectory. The \pm sign can change along this geodesic (for example, in the case of oscillatory behaviour where the momentum changes direction.), and this has to be taken into account when calculating the integral. Performing a change of variables, the result is

$$\int_{r_i}^{r_f} \pm_r \frac{1}{\sqrt{\mathcal{R}(r)}} dr = \int_{\theta_i}^{\theta_f} \pm_\theta \frac{1}{\sqrt{\Theta(\theta)}} d\theta . \quad (3.6)$$

Null geodesics have the special property that only the ratios $\chi = k/E^2$ and $\lambda = L/E$ are physically relevant. This manifests itself for example in the following cases:

²These are only two out of the four geodesic equations, and the only ones we will need. More relations, similar to (3.6) can be found. For a full account, see [66].

- Equations (3.2) and (3.3), with $\mu = 0$ can be rewritten as

$$\begin{aligned}\frac{\Theta(\theta)}{E^2} &= \chi - [\lambda \csc \theta - a \sin \theta]^2 , \\ \frac{\mathcal{R}(r)}{E^2} &= [(r^2 + a^2) - a\lambda]^2 - \Delta\chi ,\end{aligned}\quad (3.7)$$

where we defined $\chi = k/E^2$ and $\lambda = L/E$. We see that the shape of both potentials depends only on two ratios instead of 3 constants.

- The equation (3.6) is invariant under rescaling of E , since both sides depend on E in the same way.
- The condition (3.14) we apply for bound orbits is also invariant under rescaling of E .

Of course, this only makes sense if $E \neq 0$, but this is not possible for massless particles due to the relation $p^\mu p_\mu = 0$. In what follows we will therefore work with the ratios χ (or equivalently $\eta \equiv Q/E^2$) and λ .

3.1.1 The angular integral

Let us first focus on the angular integral in (3.6). We will see that bound geodesics in the Kerr spacetime exhibit oscillations between two turning points θ_\pm . This will be relevant when we extend the ideas to nearly bound geodesics in Chapter 4.

We start by rewriting the angular potential (3.2) as

$$\Theta(\theta) = \eta + a^2 \cos^2 \theta - \lambda^2 \cot^2 \theta .$$

Note that this allows us to give a physical interpretation to the constant η : in the equatorial plane we have that $\Theta(\pi/2) = \eta$, such that the geodesic equation (3.5) reduces to $r^2 \dot{\theta} = \pm_\theta \sqrt{\eta}$. This means that η is related to the angular velocity of the photon in the θ -direction when it passes through the equatorial plane. Since Θ has to be positive by definition, no geodesic can reach the poles $\theta \in \{0, \pi\}$ unless $\lambda = 0$, since $-\lambda^2 \cot^2 \theta$ can be made arbitrarily negative close to the poles. We defer the special case $\lambda = 0$ to the end of this section. For $\lambda \neq 0$, the polar motion is restricted between points θ_\pm in the open interval $(0, \pi)$, with $\Theta(\theta_\pm) = 0$. Define the variable $u = \cos^2 \theta$. Then we can rewrite the angular potential as

$$\begin{aligned}\Theta(u) &= \eta + a^2 u - \lambda^2 \frac{u}{1-u} \\ &= \frac{a^2}{1-u} \left[-u^2 + \left(1 - \frac{\eta + \lambda^2}{a^2} \right) u + \frac{\eta}{a^2} \right] .\end{aligned}\quad (3.8)$$

This is a quadratic polynomial for which we can find the roots u_\pm , and the result is

$$\Theta(u) = \frac{a^2}{1-u} (u_+ - u) (u - u_-) ,\quad (3.9)$$

where we defined

$$u_{\pm} = \Delta_{\theta} \pm \sqrt{\Delta_{\theta}^2 + \frac{\eta}{a^2}}, \quad \Delta_{\theta} = \frac{1}{2} \left(1 - \frac{\eta + \lambda^2}{a^2} \right). \quad (3.10)$$

We will show later that $\eta \geq 0$ for our purposes, which implies that both roots are real. Furthermore, it is clear that $u_- \leq 0 < u_+$, with the first inequality being strict if $\eta > 0$. Assume the latter is the case for now, and since there must be turning points $\theta_{\pm} \in (0, \pi)$ we will have that $u_+ < 1$. So, we have the correspondence $\theta_{\pm} = \cos^{-1}(\mp\sqrt{u_+})$, implying that the geodesic passes through the equator.

We can now work out the angular integral in (3.6). We will split this integral along the geodesic in pieces from the equator to the turning points, and denote the piece from the equator ($\theta = \pi/2$) to θ_+ as $G_{\theta}/2$. Note that on this domain, we have the correspondence $\cos \theta = -\sqrt{u}$. Using $du = -2 \sin \theta \cos \theta d\theta = 2\sqrt{(1-u)u} d\theta$, we can now write (note that $\pm_{\theta} \equiv +$ since θ increases)

$$\begin{aligned} \frac{G_{\theta}}{2} &= \int_{\pi/2}^{\theta_+} \frac{d\theta}{\sqrt{\Theta(\theta)}} \\ &= \int_0^{u_+} \frac{du / (2\sqrt{(1-u)u})}{\sqrt{\frac{a^2}{1-u}(u_+ - u)(u - u_-)}} \\ &= \frac{1}{2\sqrt{a^2}} \int_0^{u_+} \frac{du}{\sqrt{u(u_+ - u)(u - u_-)}}, \end{aligned}$$

and upon making the substitution $u = u_+ t^2$ we find

$$\begin{aligned} \frac{G_{\theta}}{2} &= \frac{1}{2\sqrt{a^2}} \int_0^1 \frac{2u_+ t dt}{\sqrt{u_+ t^2 (u_+ - u_+ t^2) (u_+ t^2 - u_-)}} \\ &= \frac{1}{\sqrt{a^2}} \int_0^1 \frac{dt}{\sqrt{(1-t^2)(u_+ t^2 - u_-)}} \\ &= \frac{1}{\sqrt{-a^2 u_-}} \int_0^1 \frac{dt}{\sqrt{(1-t^2)\left(1 - \frac{u_+}{u_-} t^2\right)}}. \end{aligned}$$

Note that this integral is in fact finite: since $u_+/u_- < 0$, the only root of the denominator in the interval $[0,1]$ is located at $t = 1$, where the integrand diverges only as $(1-t)^{-1/2}$.

This integral is positive, as we implicitly took the plus in \pm_{θ} here since θ increases. If we were to calculate the integral along the geodesic from θ_+ to the equator, we would have to manually add the minus sign from \pm_{θ} (because θ decreases), which would then cancel against the interchanged integration boundaries. Therefore, the integral does not cancel out starting from the equator, going up to θ_+ and back, but rather this gives two identical contributions. By symmetry, the same story holds for the trajectory down to θ_- (since $\theta_+ = \pi - \theta_-$). Therefore, the integral G_{θ} we just computed is one half of the

integral along a full oscillation, and describes the motion in the θ -direction.

We can rewrite the integral as³

$$G_\theta = \frac{2}{\sqrt{-a^2 u_-}} K \left(\sqrt{\frac{u_+}{u_-}} \right). \quad (3.11)$$

The function K is called *the complete elliptic integral of the first kind*, and is given by

$$K(k) = \int_0^1 \frac{dt}{\sqrt{(1-t^2)(1-k^2 t^2)}}. \quad (3.12)$$

Treatment of special cases

The previous calculation relies on the assumptions $\eta > 0$ and $\lambda \neq 0$, which we justify now. These assumptions break down when either $\eta = 0$ or $\lambda = 0$. In practice, we do not need to worry about this measure-zero set, but we briefly discuss these two cases.

First of all, we address the bound orbits with $\eta = 0$. They have the property $u_- = 0$, meaning that $\theta = \pi/2$ becomes a zero of the angular potential. Figure 3.1 shows the qualitative behaviour of η in the region where it is positive, along with u_+ . The radii r_{\pm}^γ (see equation (3.22) below) where $\eta = 0$ mark the boundaries of this region. In these points, u_+ also goes to zero, which means we actually have a double root of the angular potential in $u = 0$. This means that $\Theta(\theta)$ is only non-negative in the equatorial plane, such that the geodesic is confined to it. For such geodesics, the angular integral becomes irrelevant, as there is no angular motion. As is clear from the figure, these equatorial orbits occur for the boundary cases $r \rightarrow r_{\pm}^\gamma$. Therefore, results for the general case can be interpreted for these equatorial geodesics in this limit.

We also neglected the case $\lambda = 0$. This corresponds to an orbit that passes over the poles. As we can see in Figure 3.1, this happens for an intermediate radius r_3 ($r_-^\gamma < r_3 < r_+^\gamma$), which is given by [81]

$$r_3 = M + 2\sqrt{M^2 - \frac{1}{3}a^2} \cos \left[\frac{1}{3} \cos^{-1} \left(\frac{M(M^2 - a^2)}{(M^2 - \frac{1}{3}a^2)^{3/2}} \right) \right]. \quad (3.13)$$

The angular potential for these orbits is given by

$$\Theta(\theta) = \eta + a^2 \cos^2 \theta,$$

which is always positive since $\eta(r_3) > 0$. At the poles we have that $\Theta(\pm\pi/2) = \eta + a^2$. The fact that this is positive even though θ should decrease afterwards is a result of the coordinate singularity at the poles. However, the limits $\lim_{r \rightarrow r_3} u_+ = 1$ and $\lim_{r \rightarrow r_3} \eta$ exist and are finite as can be seen in Figure 3.1. These functions are continuous, and therefore we can also calculate the angular integral as given in (3.11) for this geodesic. The difference is that u_+ now does not correspond to a zero of the angular potential, but it is an imposed bound on θ due to the coordinate singularity.

³Note that the argument for the function K is imaginary, as $u_- < 0$. This is however not a problem, as it becomes real in the integral, but this notation is most used in the literature.

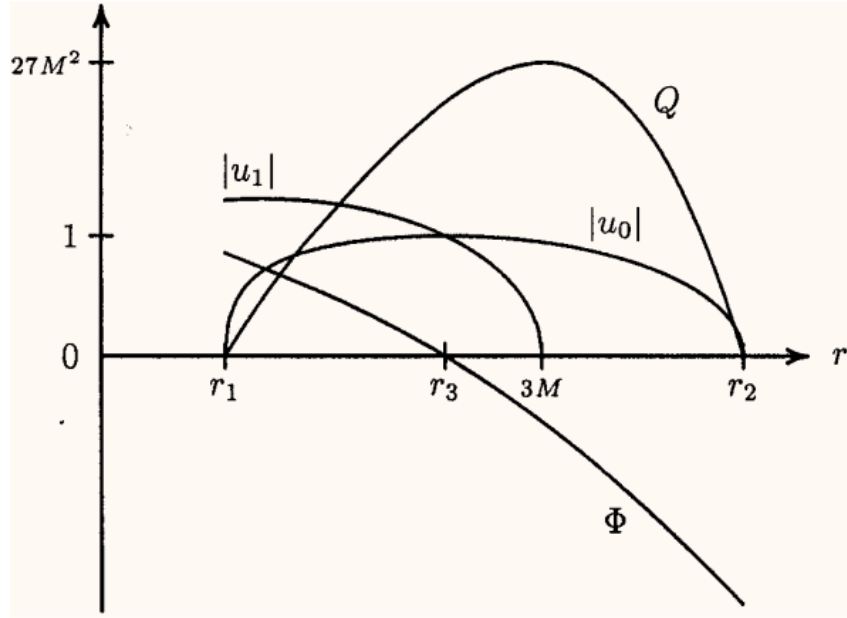


Figure 3.1: Qualitative plots for the constants of motion η and λ , here depicted as respectively Q and Φ , in the photon sphere of the Kerr metric. The maximum of η is located at $r = 3M$, with a value of $27M^2$. The radii r_1 and r_2 correspond to r_-^γ and r_+^γ respectively. The latitude $u_0 \leq 1$ corresponds to u_+ in this work. The parameter u_1 is not of interest here. Figure taken from [81]

3.1.2 The radial potential

Having discussed the polar motion, equation (3.6) shows that we still need to investigate the radial motion. In Chapter 4 an approximate solution to this integral is needed, based on the properties of the radial potential (3.3) for bound null geodesics. Therefore, this section is devoted to studying some properties of these trajectories.

First of all, [51] provides us with an argument to prove that bound orbits in the Kerr metric have a fixed radius, i.e. there are no bound null geodesics that oscillate in the radial direction. The authors also prove that the root structure of the radial potential (which is a quartic polynomial in r with real coefficients) belongs to one of four cases (assume $a \neq 0$ so that $r_- \neq r_+$):

1. Four real roots, of which two outside the horizon,

$$r_1 \leq r_2 \leq r_- < r_+ \leq r_3 \leq r_4 .$$

2. Four real roots, all inside the horizon,

$$r_1 \leq r_2 \leq r_3 \leq r_4 \leq r_- < r_+ .$$

3. Two real roots, both inside the horizon,

$$r_1 \leq r_2 \leq r_- < r_+ \text{ and } r_3 = \bar{r}_4 .$$

4. No real roots.

The essential idea behind the classification above is that real roots must occur in 'pairs', i.e. r_3 and r_4 (resp. r_1 and r_2) can not be separated by the event horizons, because the radial potential must be non-negative in between the two horizons and at $+\infty$. The allowed range for r in each of the four cases corresponds to the range where the radial potential is positive, since $p_r \propto \sqrt{\mathcal{R}(r)}$. Since this is always the case for $r \rightarrow \pm\infty$, the allowed range outside the horizon for case 1 is $[r_+, r_3] \cup [r_4, +\infty)$, and is equal to $[r_+, +\infty)$ for all the other cases. The first interval corresponds to some trajectory emerging from the horizon turning at r_3 and falling back in, and the second corresponds to an approach from infinity, with a turning point at r_4 before going off to infinity again. The third interval corresponds to falling in from / flying out to infinity.

Therefore, there is no case in which a photon can be found between two turning points outside the horizon. Therefore, the only bound orbits that do not fall in correspond to fixed- r orbits⁴, meaning that

$$\mathcal{R}(r) = \mathcal{R}'(r) = 0. \quad (3.14)$$

This second condition follows from the requirement that $d^2r/d\lambda^2 = 0$ for the geodesic, so that it remains on a fixed radius. Using (3.4) we find that

$$\begin{aligned} \frac{d\Sigma}{d\sigma} \frac{dr}{d\sigma} + \Sigma \frac{d^2r}{d\sigma^2} &= \pm_r \frac{\mathcal{R}'(r)}{2\sqrt{\mathcal{R}(r)}} \frac{dr}{d\sigma} \\ &= \pm_r \frac{\mathcal{R}'(r)}{2\Sigma} \end{aligned}$$

Evaluating this at a radius r_B that permits a bound orbit, such that $\mathcal{R}(r_B) \propto dr/d\sigma|_{r_B} = 0$, we have

$$\Sigma^2(r_B) \frac{d^2r}{d\sigma^2} \Big|_{r_B} = \frac{\mathcal{R}'(r_B)}{2}.$$

So, this shows that the derivative of \mathcal{R} has to be zero for a spherical orbit.

The two conditions in (3.14) fix both constants in the radial potential entirely in terms of r . We find two possible solutions for the energy-rescaled angular momentum and Carter constant⁵. On the one hand, we find that

$$\lambda = \frac{r^2 + a^2}{a}, \quad (3.15)$$

$$\eta = -\frac{r^4}{a^2}, \quad (3.16)$$

and on the other hand we have

$$\lambda = \frac{M(r^2 - a^2) - r\Delta}{a(r - M)}, \quad (3.17)$$

$$\chi = \frac{4r^2\Delta}{(r - M)^2}. \quad (3.18)$$

⁴Note that the radial integral in (3.6) does not make much sense in this case. In the next chapters we will study *nearly*-bound geodesics, for which this integral does make sense after all.

⁵The two versions of the Carter constant, $\chi \equiv k/E^2$ and $\eta \equiv Q/E^2$ are of course related by $\eta = \chi - (\lambda - a)^2$.

As we will see in a moment, the first set of expressions can be ruled out as unphysical.

We return to why the Carter constant is positive for these spherical orbits [81]. Suppose that $\eta < 0$. Note that in this case the angular potential (3.8) cannot have a positive root for u unless

$$1 - \frac{\eta + \lambda^2}{a^2} > 0. \quad (3.19)$$

But, it turns out that this is impossible when $\eta < 0$. Upon inserting the solutions (3.17,3.18) we find that

$$\begin{aligned} 1 - \frac{\eta + \lambda^2}{a^2} &= \frac{-\chi - 2\lambda a + 2a^2}{a^2} \\ &= -2r \frac{r^3 - 3M^2r + 2a^2M}{a^2(r - M)^2}. \end{aligned}$$

Define $N(r) = r^3 - 3M^2r + 2a^2M$, and observe that $N'(r) = 3r^2 - 3M^2$. Since the asymptotic behaviour of N is $N \sim r^3$, we find that $r = M$ is a minimum of the function $N(r)$, and thus that $N(r) \geq N(r_+)$ if $r \geq r_+ \geq M$. Therefore we have that

$$\begin{aligned} 1 - \frac{\eta + \lambda^2}{a^2} &\leq -2r_+ \frac{r_+^3 - 3M^2r_+ + 2a^2M}{a^2(r - M)^2} \\ &= -2r_+^2 \frac{M^2 - a^2}{a^2(r - M)^2} \\ &\leq 0. \end{aligned}$$

This means that we can have no positive roots for u if $\eta < 0$, meaning that this possibility is ruled out. We then have that the allowed range of r -values for bound, spherical orbits is given by the range over which $\eta \geq 0$. By this reasoning we can also see that the first set of expressions for λ, χ has to be excluded, since $\eta < 0$ everywhere.

The zeroes of η can be found analytically. Starting from (3.17 3.18), we find that

$$\eta = -r^3 \frac{r^3 - 6Mr^2 + 9M^2r - 4a^2M}{a^2(r - M)^2}. \quad (3.20)$$

Disregarding the r^3 factor in front, this is a cubic equation for which the general formula is known. Defining $r' = r - 2M$, this equation is transformed into the depressed cubic

$$r'^3 - 3M^2r' + 2M^3 - 4a^2M = 0.$$

This has the general solutions

$$r'_k = 2\sqrt{-\frac{p}{3}} \cos \left[\frac{1}{3} \cos^{-1} \left(\frac{3q}{2p} \sqrt{-\frac{3}{p}} \right) - \frac{2\pi k}{3} \right], \quad k \in \{0, 1, 2\},$$

where $p = -3M^2$ and $q = 2M^3 - 4a^2M$. The solution is then

$$r_k = 2M \left(1 + \cos \left[\frac{1}{3} \cos^{-1} \left(-1 + \frac{2a^2}{M^2} \right) - \frac{2\pi k}{3} \right] \right), \quad k \in \{0, 1, 2\}.$$

Using the trigonometric identity $2\cos^2\theta - 1 = \cos 2\theta$, we can rewrite this as

$$r_k = 2M \left(1 + \cos \left[\frac{2}{3} \cos^{-1} \left(\pm \frac{a}{M} \right) - \frac{2\pi k}{3} \right] \right), \quad k \in \{0, 1, 2\}. \quad (3.21)$$

The expression above describes a priori 6 different solutions, but since the original equation was of degree 3 some of these should overlap. The different solutions can be seen in Figure 3.2, from which it is clear that we only need two of these solutions

$$r_{\pm}^{\gamma} = 2M \left[1 + \cos \left(\frac{2}{3} \cos^{-1} \left(\pm \frac{a}{M} \right) \right) \right]. \quad (3.22)$$

This formula is derived in [7], in which a different approach is followed. The method I introduced here is more straightforward, and can easily be extended to other metrics. It should be emphasized that the radii (3.22) do *not* correspond to the inner and outer horizon r_{\pm} in the Kerr metric, which is why they are given the additional label γ referring to a photon. The radius r_-^{γ} is also referred to as the ISCO. Figure 3.2 nicely reproduces the bound photon orbit at $r = 3M$ for the Schwarzschild BH. Furthermore, it shows that in the case of the extremal Kerr BH the bound photon orbits are restricted between $r_-^{\gamma} = M$ and $r_+^{\gamma} = 4M$.

For bound orbits, using (3.17, 3.18) in (3.10), we find that u_{\pm} can be expressed in terms of the radius r of the bound orbit:

$$u_{\pm}(r) = \frac{r}{a^2(r-M)^2} \left[-r^3 + 3M^2r - 2a^2M \pm 2\sqrt{M\Delta(2r^3 - 3Mr^2 + a^2M)} \right]. \quad (3.23)$$

Given a radius r_B in the range $[r_-^{\gamma}, r_+^{\gamma}]$, the above formula provides the turning points $\theta_{\pm}(r_B) = \cos^{-1}(\mp\sqrt{u_{\pm}(r_B)})$ of the polar motion of the bound orbit at r_B . This parametrizes the region of spacetime that contains bound null geodesics, which is referred to as the *photon shell*. It is visualized in Figure 4.4 in a later chapter.

This is all we need for our further purposes. The next sections will extend these results to the other metrics, focusing mostly on the differences with Kerr.

3.1.3 Extension to Kerr-Newman

The discussion in the previous section can easily be extended to the KN metric [38]. As was the case for the regular Kerr BH, we still have three conserved quantities L, E and k in addition to (2.9). The Carter constant is given once again⁶ by (2.24). Furthermore, the radial and angular potentials have the same form as (3.3, 3.2), now including the charge q in the expression (2.16) for Δ . The geodesic equations retain their form, which means we still have the equation (3.6).

⁶It can once again also be derived from a Killing tensor: this can for example be found in [18]. Such a Killing tensor is also known for the KN-AdS-dS black hole, which is a solution of the Einstein-Maxwell equations with a non-vanishing cosmological constant [44].

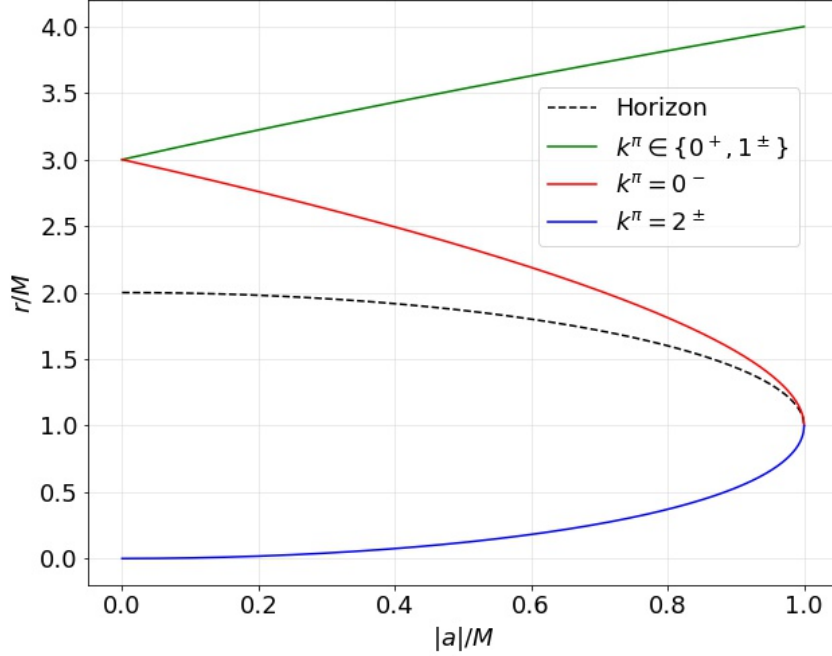


Figure 3.2: The different solutions (3.21) to the cubic equation $\eta = 0$ as a function of the reduced spin. The symbol π denotes the sign in the expression for the solution. This Figure shows that there is overlap between the different possibilities, such that we only need two different expressions r_{\pm}^{γ} . The blue line is excluded as it is contained within the event horizon.

We still don't have bound orbits that oscillate in the radial direction, as a consequence of the root structure of the radial potential. The argument to prove this is completely analogous to the argument given for the Kerr metric in the previous section. So, the bound orbits are fixed- r orbits once again, subject to the condition (3.14).

The condition (3.14) still implies expressions for the ratios λ and χ . The result (3.18) for χ remains the same - with the expression (2.17) for Δ that includes the charge q - and λ becomes

$$\lambda = \frac{M(r^2 - a^2) - q^2r - r\Delta}{a(r - M)}, \quad (3.24)$$

which obviously reduces to (3.17) for zero charge. Again we can prove that $\eta \geq 0$ for bound orbits, which is the reason that the other set of solutions (3.15,3.16) is omitted. The condition (3.19) for a positive root of the angular potential (if $\eta < 0$) remains unchanged,

and similarly we find a contradiction:

$$\begin{aligned} 1 - \frac{\eta + \lambda^2}{a^2} &\leq -2r_+ \frac{r_+^3 - 3M^2r_+ + 2M(a^2 + q^2)}{a^2(r_+ - M)^2} \\ &= -2r_+^2 \frac{M^2 - a^2 - q^2}{a^2(r_+ - M)^2} \\ &\leq 0. \end{aligned}$$

The zeroes of η , which now correspond to a double root at 0 and the roots of a quartic equation, are not so useful to express analytically. A general solution to the quartic equation exists, but the expressions are cumbersome. Figure 3.3 shows the two solutions outside the horizon for varying values of the parameters a and q . They once again represent the bound equatorial null geodesics. First of all, we recover the behaviour of the solutions to the similar problem in the Kerr spacetime by looking at the horizontal axis. Furthermore, we notice that the charge in general decreases the first (i.e. the largest) solution, up until the point $q = M, a = 0$ where the outer solution approaches $2M$. The second solution also approaches $2M$ in the same point, and is in general smaller closer to extremality. While determining these solutions numerically, the other solutions were also found: they are bound above by M , i.e. they are inside the horizon. Figures A.1 and A.2 in Appendix A show both.

Finally, the integral over the angular potential is solved with the exact same method, but the expressions for u_{\pm} change due to the new expressions for χ and λ . They are now given by

$$u_{\pm}(r) = \frac{r}{a^2(r - M)^2} \left[-r^3 + 3M^2r - 2M(a^2 + q^2) \right. \\ \left. \pm 2\sqrt{\Delta(2Mr^3 - 3M^2r^2 + a^2M^2 - q^2r^2 + 2Mq^2r)} \right]. \quad (3.25)$$

Having extended everything to include a charge in the metric, we should again point out the subtleties we neglected in the previous analysis. However, the comments on the cases $\lambda = 0$ and $\eta = 0$ are identical to the discussion for the Kerr spacetime.

3.2 Extension to the Johannsen metric

The goal is now to extend the analysis of section 3.1 to the Johannsen metric, again for null geodesics. We will perform the same calculations, starting from the same assumptions. A priori, some of these assumptions can be violated. However, since the Johannsen metric deviates from Kerr in a continuous manner we expect these assumptions to remain valid at least for small deviations. The results that we obtain will be compared to numerical results in Chapter 5, where it becomes clear that the correct results are obtained analytically.

The general procedure remains the same: we start again with the same 3 conserved quantities L, E and k (still given by (2.24)) and the relation (2.9), and determine the

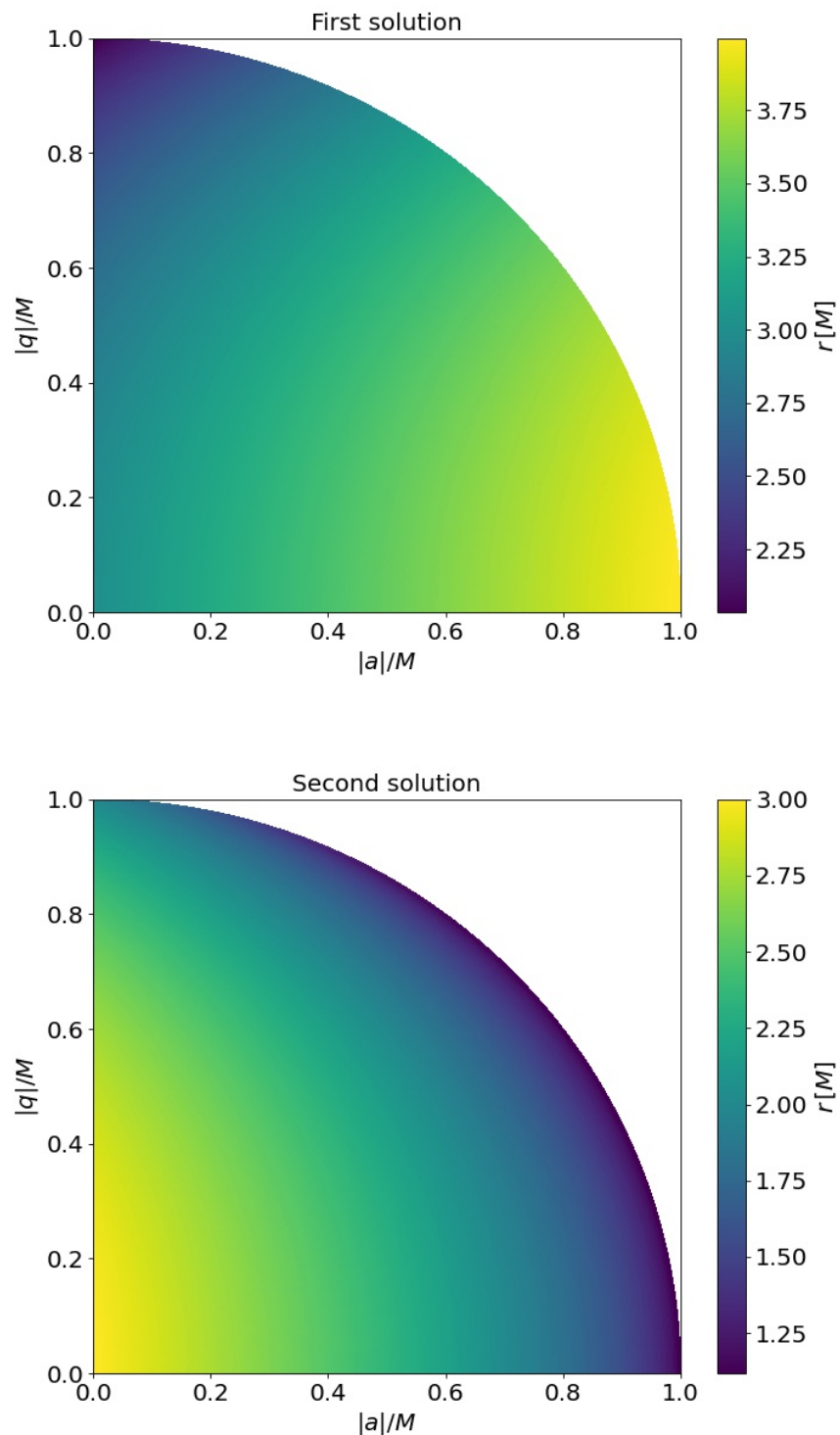


Figure 3.3: The largest two solutions to the equation $\eta = 0$ for the Kerr-Newman metric for varying parameters a and q . The color corresponds to the value of the solution, expressed in gravitational radii. Note the different scales on the colorbars.

radial and angular potentials. Since the expression for k did not change, neither will $\Theta(\theta)$. The radial potential, however, is given by

$$\mathcal{R}(r) \equiv A_5(r)\Delta^2 p_r^2 = [A_1(r)(a^2 + r^2)E - A_2(r)aL]^2 - \Delta k. \quad (3.26)$$

We have a modified version of (3.6) since the form of the geodesic equations changes, which looks like

$$\pm_r \int_{r_i}^{r_f} \frac{dr}{\sqrt{A_5(r)\mathcal{R}(r)}} = \pm_\theta \int_{\theta_i}^{\theta_f} \frac{d\theta}{\sqrt{\Theta(\theta)}}. \quad (3.27)$$

The new expressions for χ and λ obtained from the bound orbit condition (3.14) are

$$\lambda = \frac{[M(a^2 - r^2) + q^2r + r\Delta]A_1 + (a^2 + r^2)\Delta A'_1}{a(M - r)A_2 + a\Delta A'_2}, \quad (3.28)$$

$$\chi = \frac{\Delta [(a^2 + r^2)(A_2 A'_1 - A_1 A'_2) + 2rA_1 A_2]^2}{[(M - r)A_2 + \Delta A'_2]^2}. \quad (3.29)$$

We did not write the functional dependence here, but of course A_1, A_2 and Δ depend on r . These expressions all nicely reduce to the values for KN, if the deviation functions A_1 and A_2 are set to 1, i.e. in the limit of no deviation.

The angular integral is still of the same form as (3.11) and solving it is therefore still possible. This assumes that the Carter constant is positive for all bound spherical null geodesics, but we will precisely use the range of r -values for which this is the case. We will not find any evidence that we are missing null geodesics that have $\eta < 0$. Given the expressions (3.28, 3.29) for the constants of motion we can again calculate u_\pm that are needed in the angular integral, but the analytic expression is too long to be enlightening.

3.3 Extension to the almost-BPS metric

The last metric that is of interest for this chapter is the almost-BPS black hole. First of all, we need three constants of motion in addition to (2.9) if we want to apply a method that is similar to what we did in the previous sections. It is obvious that E and L are two conserved quantities once again, due to the metric components being independent of t and ϕ . A Carter-like conserved quantity can once again be found by separating the Hamilton-Jacobi equations. However, we will show that *this is only possible for geodesics of massless particles*. This is a phenomenon that is derived for other string-theory based BHs, which are related to the almost-BPS metric considered here [10, 68]. Therefore, one could have expected this separability for the BH of interest, which we check explicitly here.

Assuming once again a Hamilton-Jacobi function of the form (2.20), we find that the HJ equations (2.19) read

$$\begin{aligned} -\frac{\mu^2}{2} &= \frac{\alpha^2 \sin^2 \theta - \Delta^2}{\rho^2 \Delta} E^2 + \frac{\rho^2}{\Delta} p_r^2 + \frac{1}{\Delta} p_\theta^2 + \frac{L^2}{\Delta \sin^2 \theta} - 2EL \frac{\alpha}{\rho \Delta} \\ \Leftrightarrow -\frac{\mu^2}{2} \Delta &= \frac{\alpha^2 \sin^2 \theta - \Delta^2}{\rho^2} E^2 + \rho^2 p_r^2 + p_\theta^2 + \frac{L^2}{\sin^2 \theta} - 2EL \frac{\alpha}{\rho}. \end{aligned} \quad (3.30)$$

We rewrite (2.37) as

$$\Delta \equiv \sqrt{f(\rho) - (m_\infty \rho^2 + \alpha \cos \theta)^2}, \quad (3.31)$$

where $f(\rho) = (h\rho + Q_0)\Pi_I (\frac{\rho}{h} + Q_I)$. As a result, we have

$$\Delta^2 = f(\rho) - m_\infty^2 \rho^4 - 2m_\infty \alpha \rho^2 \cos \theta - \alpha^2 \cos^2 \theta. \quad (3.32)$$

The first term on the right-hand side of (3.30) becomes separable in ρ and θ :

$$\frac{\alpha^2 \sin^2 \theta - \Delta^2}{\rho^2} E^2 = \left[\frac{\alpha^2 + m_\infty^2 \rho^4 - f(\rho)}{\rho^2} + 2m_\infty \alpha \cos \theta \right] E^2.$$

Therefore, the entire right-hand side of (3.30) is separable in ρ and θ , as opposed to the left-hand side due to the factor Δ which is in itself not separable. Therefore, setting $\mu = 0$ allows us to separate the entire HJ equation as

$$-\rho^2 p_r^2 + 2EL \frac{\alpha}{\rho} - \frac{\alpha^2 + m_\infty^2 \rho^4 - f(\rho)}{\rho^2} E^2 = k = p_\theta^2 + 2m_\infty \alpha E^2 \cos \theta + \frac{L^2}{\sin^2 \theta}. \quad (3.33)$$

This shows that the HJ equations are only separable for null geodesics.

The result (3.33) leads us to define the following radial and angular potential:

$$\mathcal{R}(r) \equiv \frac{\rho^4}{E^2} p_r^2 = f(\rho) - \alpha^2 - m_\infty^2 \rho^4 + 2\lambda \alpha \rho - \chi \rho^2, \quad (3.34)$$

$$\Theta(\theta) \equiv \frac{1}{E^2} p_\theta^2 = -2m_\infty \alpha \cos \theta - \lambda^2 \csc^2 \theta + \chi, \quad (3.35)$$

where we again defined the energy-rescaled angular momentum $\lambda = L/E$ and Carter constant $\chi = k/E^2$.

In order to find the geodesic equations, we just raise the indices:

$$\frac{d\rho}{d\lambda} \equiv p^\rho = g^{\rho\rho} p_\rho = \pm_\rho \frac{\sqrt{\mathcal{R}(\rho)}}{\Delta}, \quad (3.36)$$

$$\frac{d\theta}{d\lambda} \equiv p^\theta = g^{\theta\theta} p_\theta = \pm_\theta \frac{\sqrt{\Theta(\theta)}}{\Delta}. \quad (3.37)$$

This gives us the following equality for integrals along the geodesic:

$$\pm_\rho \int_{\rho_i}^{\rho_f} \frac{d\rho}{\sqrt{\mathcal{R}(\rho)}} = \pm_\theta \int_{\theta_i}^{\theta_f} \frac{d\theta}{\sqrt{\Theta(\theta)}}. \quad (3.38)$$

We discuss the left- and right-hand side separately.

Radial Potential

The radial potential (3.34) is a polynomial of degree 4, and can therefore have 4 distinct real roots. We want to check if bound orbits that oscillate in the radial direction are possible. This is only possible if the radial potential is positive on an interval bounded by 2 distinct positive roots. Note however that the coefficient of the ρ^4 -term is equal to 1: $f(\rho)$ has a term ρ^4/h^2 , which combines with the other ρ^4 term in (3.34) because of (2.38). This fixes the sign of the potential to be positive for $\rho \rightarrow \pm\infty$. Therefore, at least three positive roots are needed to allow bound orbits that oscillate in the radial direction. Furthermore, the constant term is $\Pi_\Lambda Q_\Lambda - \alpha^2$, which is strictly positive because of (2.41). As a result, the number of positive roots and the number of negative roots must be even (including multiplicity). This gives us the following sufficient condition to eliminate radially oscillating bound orbits:

If there exists a $\rho^* < 0$ such that $\mathcal{R}(\rho^*) \leq 0$, the radial potential has at least 2 negative roots (including multiplicity), implying that radially oscillating orbits are impossible.

Once parameters for the metric are chosen, this criterion can quickly determine whether radially oscillating bound orbits are impossible for any value of the conserved quantities, by simply plotting the radial potential over a sufficiently large range of negative ρ . For now, we continue assuming that only fixed- ρ bound orbits are allowed.

The condition for a bound stable orbit (3.14), for the variable ρ this time, is unchanged. This results in expressions for the two independent constants of motion,

$$\begin{aligned} \lambda &= \frac{\alpha^2 - \prod Q_\Lambda}{\alpha\rho} - \frac{Q_0(Q_1Q_2 + Q_1Q_3 + Q_2Q_3) + h^2Q_1Q_2Q_3}{2h\alpha} \\ &\quad + \frac{Q_0 + h^2(Q_1 + Q_2 + Q_3)}{2h^3\alpha}\rho^2 + \frac{\rho^3}{\alpha}, \end{aligned} \tag{3.39}$$

$$\begin{aligned} \chi &= Q_1Q_2 + Q_1Q_3 + Q_2Q_3 + \frac{\alpha^2 - \prod Q_\Lambda}{\rho^2} + \frac{2Q_0\rho}{h^3} + 2\rho\frac{Q_1 + Q_2 + Q_3}{h} \\ &\quad - 3m_\infty^2\rho^2 + \frac{Q_0(Q_1 + Q_2 + Q_3) + 3\rho^2}{h^2}, \end{aligned} \tag{3.40}$$

where the product $\prod Q_\Lambda$ is the product over all the charges $\Lambda = 0, 1, 2, 3$.

The question is now again what range of ρ permits these bound orbits. Contrary to the previous metrics, this question cannot be answered by looking for the range over which $\Theta(\pi/2)$ is positive: this was a result of the equatorial symmetry ($\theta \leftrightarrow \pi - \theta$) which is no longer present here. Therefore, it can be that there is an angle θ_m for which the allowed range of ρ is larger. We will therefore determine the contourplot of $\Theta(\theta, \chi(\rho), \lambda(\rho)) = 0$, and find the minimal and maximal value of ρ . This gives the range $[\rho_-^\gamma, \rho_+^\gamma]$.

Figure 3.4 shows a typical 3D plot of the angular potential of the bound orbits in the region where it is positive. The width in the θ -direction corresponds to the amplitude of the oscillation that the geodesic performs. This reaches a maximum in an intermediate

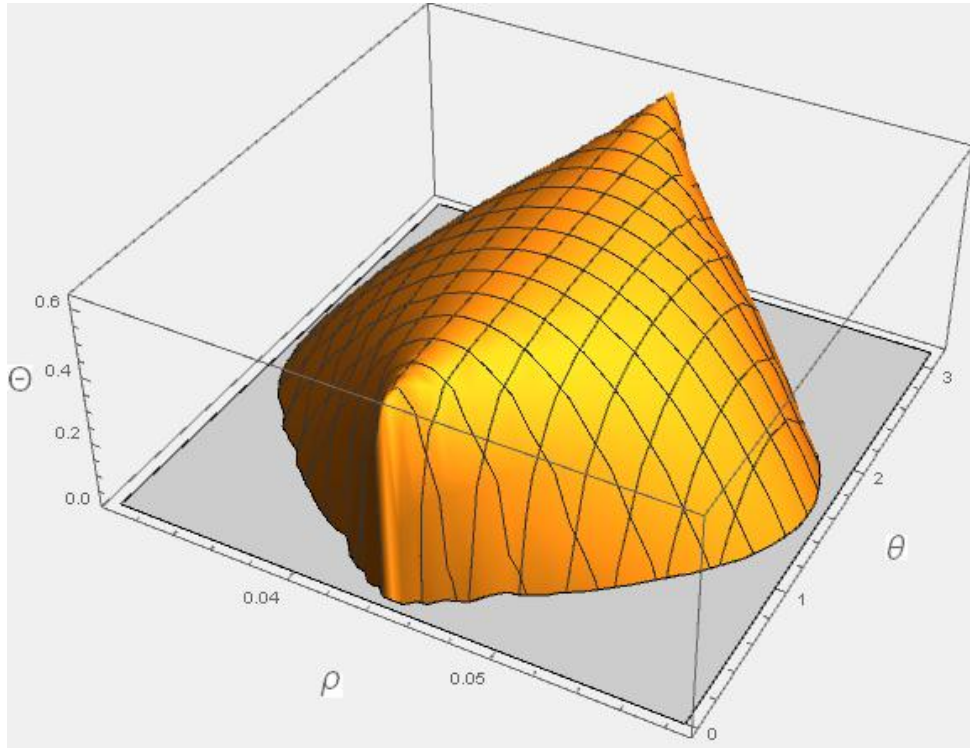


Figure 3.4: 3D-visualization of the region where $\Theta(\rho, \theta) \geq 0$, where the dependence on ρ is through the constants of motion. The parameters of the metric are $\mathbf{Q} = (2, 2, 2, 2)$, $h = 0.3$, $\alpha = 2$.

value for ρ , which corresponds to $\lambda = 0$.

The angular integral, however, is different this time. This is due to the angular potential having a different form, which cannot easily be recast as a quadratic polynomial. In practice, for the rest of this project we will calculate it numerically under the assumption that the motion in the θ -direction is constrained between two turning points. Below, we briefly investigate some properties of the potential to support this.

The angular potential

First of all, we note once again that the movement cannot go over the poles unless the angular momentum is zero. We defer this special case to the end of the argument. Let us now rewrite the angular potential (3.35) as a polynomial. Making the substitution $u = \cos \theta$, we find that

$$\begin{aligned}\Theta(u) &= \chi - 2m_\infty \alpha u - \frac{\lambda^2}{1-u^2} \\ &= \frac{2m_\infty \alpha u^3 - \chi u^2 - 2m_\infty \alpha u - \lambda^2 + \chi}{1-u^2}.\end{aligned}$$

The numerator is given by a cubic polynomial, of which we can analyse the 3 roots. The asymptotic behaviour is determined by the sign of $m_\infty \cdot \alpha$. Since we have real coefficients, we either must have 3 real roots or 1 real root and 2 conjugated complex roots.

Let us first consider geodesics that do move in the polar directions. These must have two different turning points $0 < \theta_- < \theta_+ < \pi$, which correspond to two different values $u_- > u_+ \in (-1, 1)$ since the relation $u = \cos \theta$ is one-to-one for $\theta \in [0, \pi]$. This means all three roots of $\Theta(u)$ must be real. The local maximum of the cubic potential must lie in the interval $[u_+, u_-]$, and the local minimum must lie to the left of this interval for negative $m_\infty \alpha$ and to the right for positive values of the latter. Since $\Theta(u = \pm 1)$ must be negative for nonzero angular momentum, the third root u_3 must lie outside the interval $[-1, 1]$. This means that we cannot have double roots in this case. So, we can numerically determine the three roots of the potential, and discard either the largest or smallest root depending on the sign of $m_\infty \alpha$. For these geodesics that move in the polar direction, the angular integral is thus given by

$$G_\theta = \int_{u_-}^{u_+} \frac{du}{\sqrt{2\alpha m_\infty(u - u_-)(u - u_+)(u - u_3)}}. \quad (3.41)$$

Consider now geodesics at a fixed $\theta_0 \in (0, \pi)$. As stated before, we do not longer expect these planar orbits to be in the equatorial plane as the spacetime does not have equatorial symmetry. These planar orbits must have angular momentum, and thus extending the foregoing analysis, this can only be the case if $u_0 = \cos \theta_0$ is a double root of the angular potential and corresponds to the local maximum of the cubic. It therefore corresponds to the limit $u_- \rightarrow u_+$. This provides a constraint on these fixed- θ orbits

$$\Theta \left(u = \frac{\chi \pm \sqrt{\chi^2 + 12\alpha^2 m_\infty^2}}{6\alpha m_\infty} \right) = 0, \quad (3.42)$$

where $\pm = -\text{sign}(\alpha m_\infty)$. This condition defines a curve in the λ, χ -plane given the parameters of the BH. Also, if we are looking for fixed- ρ orbits, this becomes an equation for the allowed values of ρ through (3.39, 3.40). This equation therefore allows us to determine the range of ρ in which the bound orbits exist. Note that the solutions to the equation are subject to $|u(\rho)| < 1$, which eliminates unphysical solutions.

Finally, in the case of zero angular momentum the potential becomes

$$\Theta(\theta) = \chi - 2m_\infty \alpha \cos \theta.$$

This may be non-zero in the poles, which is again an artifact of the coordinate singularity at the poles. Given that the expression (3.39) for $\lambda(\rho)$ can have at most 4 roots, we can conclude that we will not encounter points with $\lambda = 0$ in our numerical methods. This would give a problem when determining the roots of the potential. The angular integral at these points is therefore given by interpolation. This corresponds to the numerical integration of the true potential between 0 and π .

Chapter 4

Black Hole Shadows and Photon Rings

Having studied some of the geodesics in the spacetimes of interest, the next goal is to investigate two observables that can help determine which type of BH best describes observations. On the one hand, the apparent shape of a black hole can distinguish relatively crudely between different models, or at least between different sets of parameters. Nevertheless, this *shadow* suffers from a certain degree of degeneracy (see Table 4.1) and is therefore not a very accurate observable - especially in the context of realistic observations. On the other hand, light that approaches the black hole sufficiently close will be subject to extensive lensing effects. This results in so-called *photon rings* around the black hole shadow, with properties that depend heavily on the underlying spacetime. The second observable under consideration is the Lyapunov exponent associated with these photon rings. We will show that it can help lift the degeneracy associated with the black hole shadow (see Table 4.2).

Throughout this chapter, we will start each section by explaining the main concepts through the existing literature for the Kerr(-Newman) metric. Afterwards, the extension to the Johannsen and almost-BPS metrics is presented. The explicit spacetimes that are considered in this chapter all¹ have $M = 1$.

4.1 Black hole shadow

First of all, we address the question of how a distant observer sees a black hole. This brings up the concept of the *black hole shadow*, which is what the observer would perceive as being the 'black part' of the black hole itself. Importantly, this is *not* the same as the event horizon, as will be explained. It is interesting to see how the different metric parameters influence the shadow, which is the main goal of this section. We follow [6] throughout most of the section on the Kerr shadow.

¹For the almost-BPS metric we will write the parameters using the rescaling factor ζ , as introduced in section 2.2.4. Therefore, the parameters in this chapter should be considered primarily in comparison to each other.

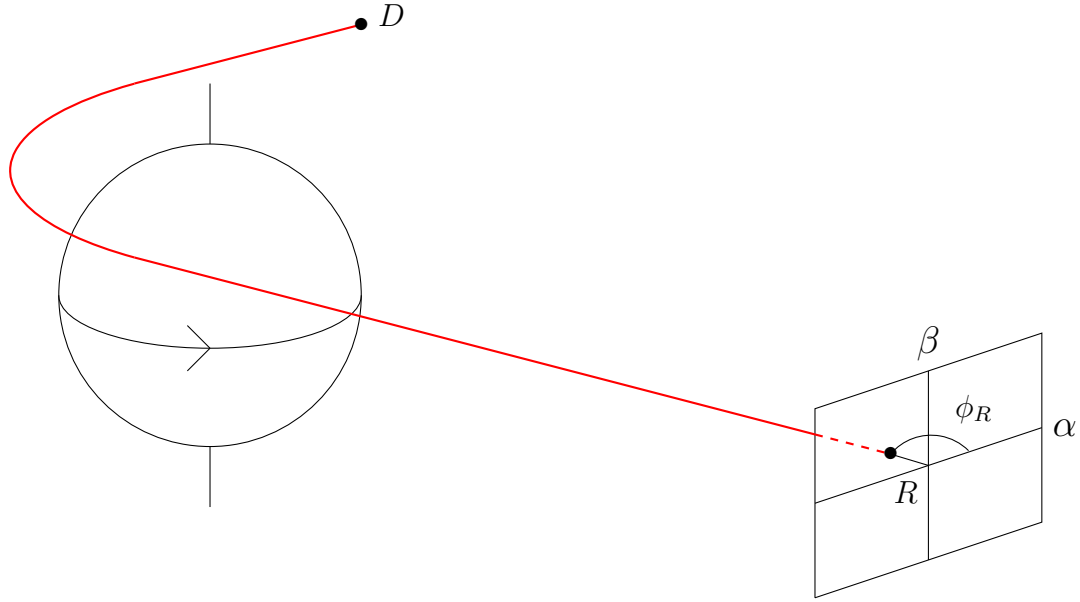


Figure 4.1: Geometry as described in the text. An observer screen with impact parameters (α, β) is located far away from the black hole, at coordinates (r_0, θ_0, ϕ_0) . The β -axis is aligned with the rotation axis of the black hole. The α -axis is perpendicular to the latter. A geodesic (red), originating from the distant point D strikes the observer screen after being deflected by the black hole. The coordinates (R, ϕ_R) are polar coordinates on the observer screen.

Let us consider for a moment a standard form for the line element of an axisymmetric, stationary metric:

$$ds^2 = -e^{2\nu}dt^2 + e^{2\psi}(d\phi - \omega dt)^2 + e^{2\lambda}dr^2 + e^{2\mu}d\theta^2. \quad (4.1)$$

In this spacetime, let us imagine an observer screen whose center is aligned with the center of symmetry of the asymptotic gravitational field (see Figure 4.1). This observer sets up a frame of reference represented by an orthonormal tetrad:

$$\begin{aligned} e_{(t)} &= e^{-\nu} \left[\frac{\partial}{\partial t} + \omega \frac{\partial}{\partial \phi} \right], \\ e_{(\phi)} &= e^{-\psi} \frac{\partial}{\partial \phi}, \\ e_{(r)} &= e^{-\lambda} \frac{\partial}{\partial r}, \\ e_{(\theta)} &= e^{-\mu} \frac{\partial}{\partial \theta}. \end{aligned}$$

From this, we find that the local measured energy of a test particle moving on a geodesic with 4-momentum p_μ (recall that we have the conserved quantities $E = -p_t$ and $L = p_\phi$) is given by

$$p^{(t)} \equiv -e_{(t)}^\mu p_\mu = e^{-\nu} (E - \omega L). \quad (4.2)$$

The physical momentum in the angular directions is given by

$$p^{(\phi)} = e^{-\psi} L, \quad (4.3)$$

$$p^{(\theta)} = e^{-\mu} p_\theta. \quad (4.4)$$

On the observer screen, we use coordinates (α, β) representing the impact parameters in the directions perpendicular to and along the axis of symmetry, respectively. Suppose the observer is located at a large distance r_0 and an inclination θ_0 . Then these impact parameters are given by [6]

$$\alpha = \lim_{r_0 \rightarrow \infty} -r_0 \frac{p^{(\phi)}}{p^{(t)}}, \quad (4.5)$$

$$\beta = \lim_{r_0 \rightarrow \infty} r_0 \frac{p^{(\theta)}}{p^{(t)}}. \quad (4.6)$$

Let us now consider a source of illumination behind the BH, whose angular size is large in comparison with the BH itself². The BH is now seen as a 'shadow' on the observer screen. Light with impact parameters close to $\alpha, \beta = 0$ will be absorbed by the BH. The rim of the shadow is determined by photons that get marginally trapped by the gravitational pull, being on the verge of getting absorbed. *It is worth stressing that this black hole shadow does not correspond to the event horizon.* The event horizon is determined by the condition that the entire future light cone is directed inward, but this need not be the case for the shadow edge. Photons that are directed outwards inside the shadow boundary may be able to escape after all. The shadow is a boundary for light that falls in from infinity, distinguishing between the light rays that fall in inevitably and the ones that escape to infinity once again. It is the apparent shape of this shadow that we want to know.

The expressions (4.5, 4.6) can be calculated for the Kerr metric. Comparing (4.1) with (2.15), we see that

$$\begin{aligned} e^{2\nu} &= \frac{\Delta\Sigma}{B}, \\ e^{2\psi} &= \frac{B}{\Sigma} \sin^2 \theta, \\ e^{2\mu} &= \Sigma, \\ \omega &= \frac{2aMr}{B}, \\ B &= (r^2 + a^2)^2 - \Delta a^2 \sin^2 \theta. \end{aligned}$$

²In principle, to get the exact definition of the shadow we should consider a light source that surrounds the black hole and observer completely so that light comes from all directions. However, the essential idea is easier to capture if we just imagine a source behind the black hole.

Then we calculate that, in the large- r_0 limit

$$\begin{aligned} \lim_{r_0 \rightarrow \infty} \frac{p^{(\phi)}}{p^{(t)}} &= \lim_{r_0 \rightarrow \infty} e^\nu e^{-\psi} \frac{L}{E - \omega L} \\ &= \lim_{r_0 \rightarrow \infty} \frac{\Sigma}{B} \sqrt{\Delta} \frac{\lambda}{1 - \omega \lambda} \frac{1}{\sin \theta_0} \\ &= \lim_{r_0 \rightarrow \infty} \frac{\Sigma \sqrt{\Delta} \lambda}{B - 2aMr_0 \lambda} \frac{1}{\sin \theta_0} \\ &= \frac{r_0^2 \sqrt{r_0^2} \lambda}{r_0^4} \frac{1}{\sin \theta_0} \\ &= \frac{\lambda}{r_0 \sin \theta_0}, \\ \lim_{r_0 \rightarrow \infty} \frac{p^{(\theta)}}{p^{(t)}} &= \lim_{r_0 \rightarrow \infty} e^{-\mu} e^\nu \frac{p_\theta}{E - \omega L} \\ &= \lim_{r_0 \rightarrow \infty} p_\theta \frac{\sqrt{\Delta B}}{BE - 2aMr_0 L} \\ &= \frac{p_\theta}{r_0 E}. \end{aligned}$$

This means that for the Kerr metric³ (using $p_\theta/E = \pm \sqrt{\Theta(\theta)}$)

$$\alpha = -\frac{\lambda}{\sin \theta_0}, \quad (4.7)$$

$$\beta = \pm \sqrt{\eta + a^2 \cos^2 \theta_0 - \lambda^2 \cot^2 \theta_0}. \quad (4.8)$$

Here we used $\eta = Q/E^2$ instead of χ . We can transform this into dimensionless polar coordinates (R, ϕ_R) on the screen (see Figure 4.1) by using the angles $\alpha/r_0, \beta/r_0$:

$$R = r_0^{-1} \sqrt{\alpha^2 + \beta^2}, \quad (4.9)$$

$$\cos \phi_R = \frac{\alpha/r_0}{R}. \quad (4.10)$$

Plugging in the expressions (4.7,4.8) gives

$$R = r_0^{-1} \sqrt{a^2 \cos^2 \theta_0 + \eta + \lambda^2}, \quad (4.11)$$

$$\phi_R = \pm \arccos \left(-\frac{\lambda}{R r_0 \sin \theta_0} \right). \quad (4.12)$$

As is clear from (4.7, 4.8), the impact parameters are completely determined by the coordinates of the observer, along with the conserved quantities of the geodesic and the physical parameters of the spacetime. Therefore, for a fixed spacetime and observer, the geodesic conserved quantities (λ, η) are in one-to-one correspondence with the impact parameters⁴ $(\alpha, |\beta|)$. So the question now is: which of these conserved quantities are

³Note that the original expression for β in [6] was incorrect.

⁴We take the absolute value to avoid the sign in (4.8). Due to the symmetry $\beta \leftrightarrow -\beta$, the correspondence is essentially one-to-one.

associated with the shadow edge on the observer screen?

The region inside the shadow corresponds to impact parameters of geodesics that fall into the BH when traced backwards from the observer. On the other hand, the region outside the shadow corresponds to impact parameters of geodesics that approach the black hole, but manage to escape to infinity in the end. The boundary of the shadow, often referred to as *the critical curve*, thus corresponds to the impact parameters of the *bound* geodesics, as they are in between both regimes. In the previous chapter we have studied these bound, fixed- r orbits and their associated conserved quantities. We have seen that these constants of motion are parametrized by r , in the range $[r_-^\gamma, r_+^\gamma]$, defined in equation (3.22), that allows bound orbits to exist. Thus, we conclude that the shadow edge is parametrized by $r \in [r_-^\gamma, r_+^\gamma]$ through the polar coordinates (4.11, 4.12), which depend on r via the constants of motion (3.17, 3.20) of the spherical orbits.

We should remark however that the range of parametrization is only equal to $[r_-^\gamma, r_+^\gamma]$ in the case of an observer in the equatorial plane. The expression (4.8) for β is only real if $\Theta(\theta_0) \geq 0$, which corresponds to the range $[r_-^\gamma, r_+^\gamma]$ if $\theta_0 = \pi/2$. For off-equatorial observers, the actual range of r will be a subset of the previous range, that we denote by $[r_-^{\theta_0}, r_+^{\theta_0}]$. These limits are determined by $\Theta(r_\pm^{\theta_0}, \theta_0) = 0$, where the dependence of Θ on r is through the constants of motion. This makes sense, since the bound geodesics at a radius outside this restricted range never reach $\theta = \theta_0$, and so we expect orbits that deviate slightly to not reach the observer. Therefore, they do not contribute to the shadow, as seen by the observer at θ_0 . This restricted range still parametrizes the entire shadow, since the boundaries of the range give $\beta = 0$, leading to $\cos \phi_R = \pm 1$ in (4.10).

Figure 4.2 shows the Kerr shadow for different values of the spin parameter a , as observed by an observer in the equatorial plane. Evidently, we recover the Schwarzschild BH when $a = 0$, and increasing the spin has a drastic effect on the shadow. The center of the observer screen no longer corresponds to the center of the shadow, and the left side gets compressed for large values of the spin. Changing the sign of the spin would flip the shadow around the vertical axis.

The effect of moving the observer away from the equatorial plane can be seen in Figure 4.3. As the observer moves closer to the poles, the asymmetry in the shadow reduces until it becomes circular. This was to be expected as the spacetime is axisymmetric, and therefore the observer at the poles no longer sees the asymmetry. Figure 4.4 shows the same effect, along with a visualisation of the photon sphere of the Kerr metric.

Before we move on to the next section, we briefly address one subtlety that we glossed over. The method as described above is not sufficient to determine the shadow of the extremal Kerr BH, with $a = M$. It will only give a part of the shadow: the vertical part at $\alpha = -2M$ (as can be seen in Figure 4.2) has to be obtained in a different way, that we do not discuss here. An explanation is given in section IIIC of [6].

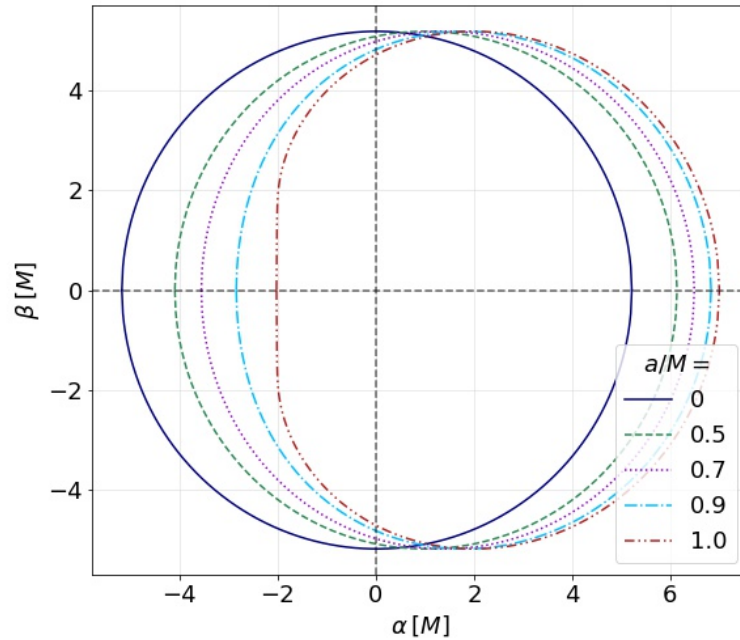


Figure 4.2: The shadow of the Kerr BH for different values of the spin parameter a . The observer is located in the equatorial plane.

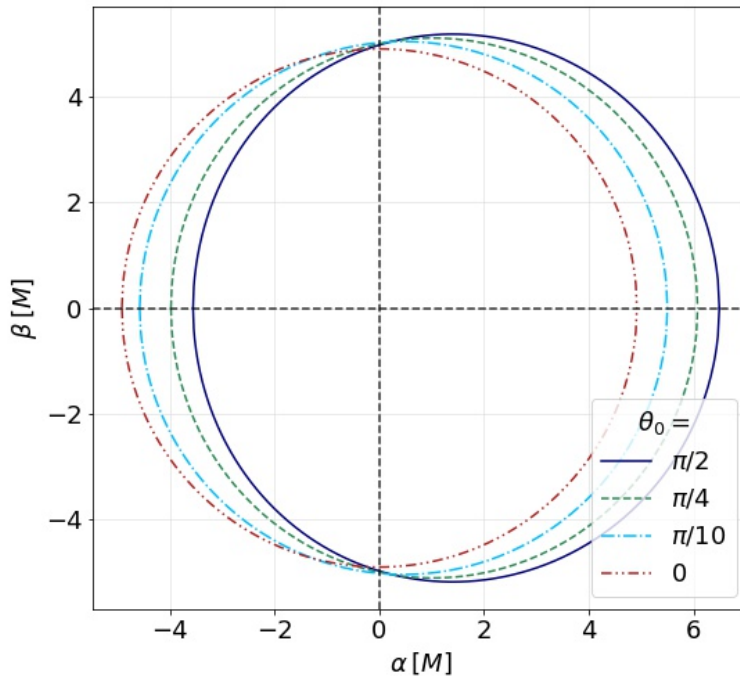


Figure 4.3: The effect of changing the observing angle θ_0 for a Kerr BH with $a = 0.7$. Moving the observer closer to the poles reduces the asymmetry in the shadow.

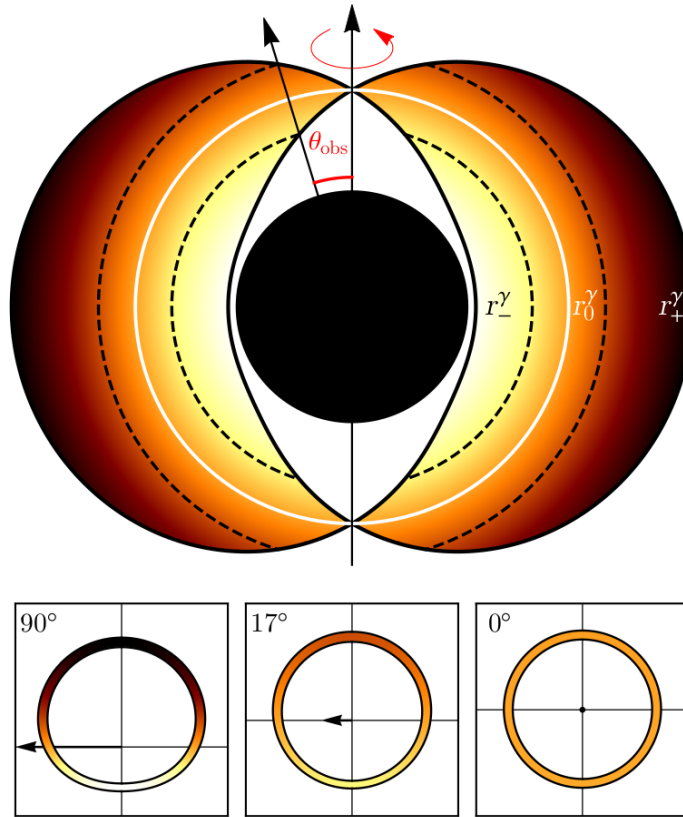


Figure 4.4: (top) The photon shell of a Kerr black hole with spin $a/M = 0.94$. The boundaries r_\pm^γ are shown, as well as the orbit at r_3 (see (3.13)) with zero angular momentum, denoted here as r_0^γ . An observer at $\theta_0 = 17^\circ$ only observes the part of the photon ring that corresponds to the intersection of his/her line of sight with the photon sphere. (bottom) The photon ring (see section 4.2) as viewed by observers at different inclinations. The color matches that of the radii that contribute to the image. Only an observer in the equatorial plane observes the photon ring associated with the entire photon shell. The face-on observer at $\theta_0 = 90^\circ$ only observes photons associated with the bound orbit at r_0 . The arrow denotes the projection of the spin axis on the plane perpendicular to the line of sight. This is Figure 2 from [64]

4.1.1 Extension to Kerr-Newman

The discussion of the previous section immediately generalizes to the case where we include a charge q . The formulas (4.11, 4.12) are still valid, but require the expression (3.24) instead of (3.17), which also changes the expression for $\eta = \chi - (\lambda - a)^2$.

The effect of the charge on the BH shadow can be seen in Figure 4.5. Increasing the charge (for a fixed mass) shrinks the BH shadow. Figure 4.6 shows several extremal shadows in the KN metric.

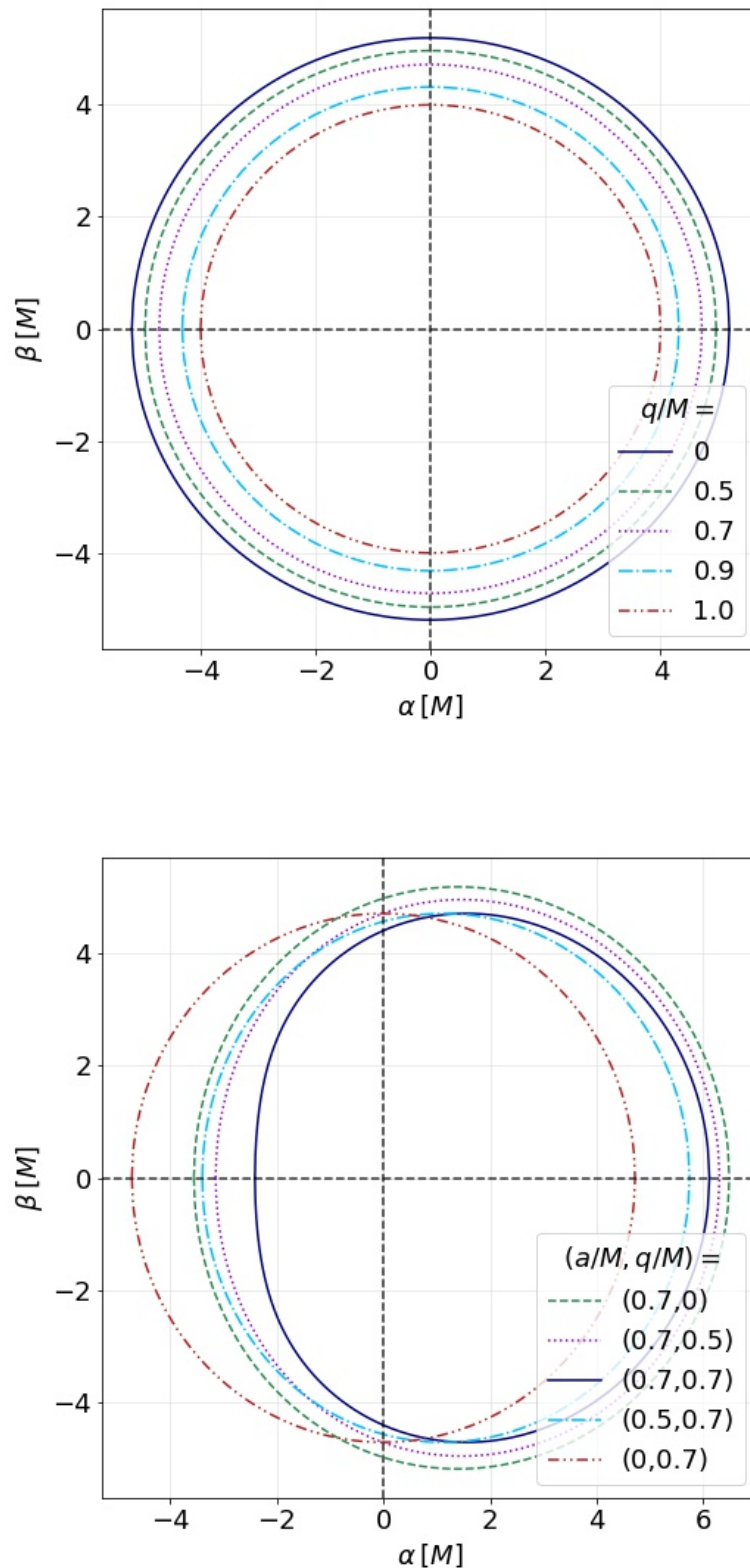


Figure 4.5: (top) Influence of the charge q on the shadow of a Reissner-Nordström BH, for an observer in the equatorial plane. (bottom) The shadow of a Kerr-Newman BH for different values of the spin a and charge q , for an observer in the equatorial plane.

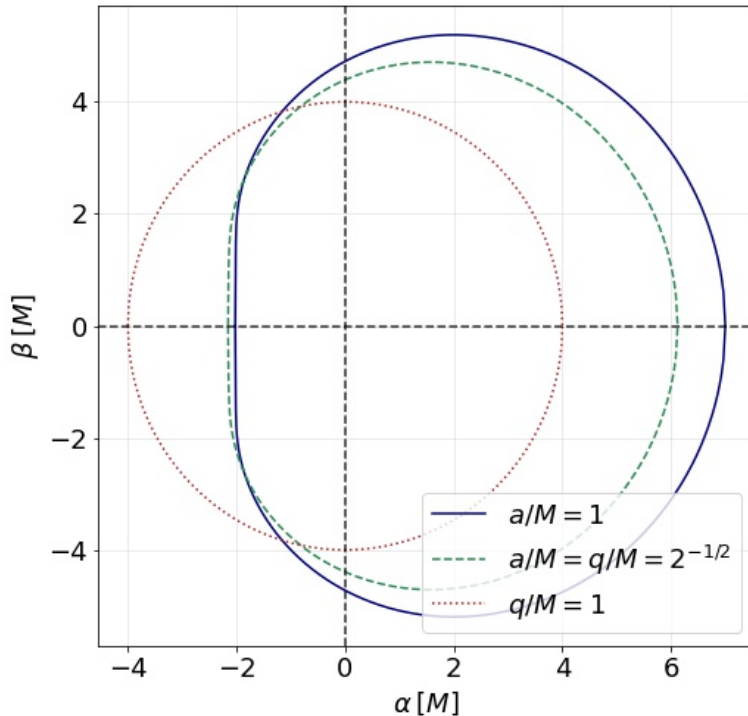


Figure 4.6: The shadow of some extremal Kerr-Newman black holes. The observer is located in the equatorial plane.

4.1.2 Johannsen metric

The calculation for the Johannsen shadow edge is very similar to the one of the Kerr metric. The results (4.11, 4.12) still hold, be it with the associated expressions (3.28, 3.29) that do cause observable differences in the shadow. This is to be expected, since the deviation function vanish at large distances and should therefore not influence the calculations in the limit $r_0 \rightarrow \infty$. The range of parametrization $[r_-^\gamma, r_+^\gamma]$ changes as well. As was explained in section 3.2, this is determined by calculating the zeroes of $\eta(r)$, for which we do not have an analytic expression. For off-equatorial observers, the appropriate subrange has to be determined as well.

We compare the shadow of the Johannsen BH with Kerr in Figure 4.7, where we fix the parameters $M = 1, a = 0.7M$. We clearly see that increasing the parameter α_{13} makes the shadow larger. For negative values of this parameter, the shadow is smaller as compared to the Kerr BH. The plot also includes the shadow of a BH with $\alpha_{13} = -4.316$, just slightly larger than the lower limit imposed by (2.35). An interesting observation is that the impact parameter on the left-hand side of the BH is smaller in absolute value than the r -coordinate of the horizon, which equals $r_+ \approx 1.71M$ for $a = 0.7M$. One could say that "the shadow is smaller than the horizon" at this point, a feature that is not present in Kerr spacetimes. This indicates very strong lensing, which we will investigate further in Chapter 5.

The parameter α_{22} has a similar effect on the shadow as the spin. A large positive value (taking into account the upper limit (2.34) since $\alpha_{13} = 0$ in the bottom plot) mimics the effect of increasing the spin. Taking a large negative value makes the shadow look as if the spin was negative. Interestingly, we also see that the shadow at $\alpha = 0$ is not influenced by the parameter α_{22} . Again, we observe that large absolute values of the deviation parameter render "the shadow smaller than the horizon", indicating very strong lensing effects.

Finally, we note that the parameter α_{52} does not influence the shadow of the BH. This is trivial, given that there is no dependence on this parameter in either (3.28, 3.29, 4.11, 4.12).

4.1.3 Almost-BPS metric

The almost-BPS BH requires some special attention, as again the method is not immediately transferrable from the Kerr metric. The metric is still of the form (4.1), with the correspondences

$$\begin{aligned} e^{2\lambda} &= \frac{\Delta}{\rho^2}, \\ e^{2\mu} &= \Delta, \\ e^{2\psi} &= -\frac{\alpha^2 \sin^4 \theta}{\Delta} + \Delta \sin^2 \theta, \\ \omega &= -\frac{\alpha \rho \sin^2 \theta}{\Delta} e^{-2\psi}, \\ e^{2\nu} &= \frac{\rho^2}{\Delta} + \omega^2 e^{2\psi}. \end{aligned}$$

The relevant asymptotic behaviour for $\rho \rightarrow \infty$ is

$$\begin{aligned} \Delta &\sim \rho^2, \\ e^\psi &\sim \rho \sin \theta, \\ \omega &\sim -\alpha \rho^{-3}, \\ e^\nu &\sim 1, \end{aligned}$$

which results in

$$\alpha \sim -\frac{\lambda}{\sin \theta_0}, \quad \beta \sim \frac{p_\theta}{E}$$

as before. However, the angular potential now has a different structure, such that we find

$$\beta = \pm \sqrt{\chi - 2m\alpha \cos \theta_0 - \lambda^2 \csc^2 \theta_0}. \quad (4.13)$$

As a result, we get different expressions for the polar coordinates on the screen in function of ρ :

$$R(\rho) = r_0^{-1} \sqrt{\chi - 2m\alpha \cos \theta_0}, \quad (4.14)$$

$$\phi_R(\rho) = \pm \arccos \left(-\frac{\lambda}{Rr_0 \sin \theta_0} \right). \quad (4.15)$$

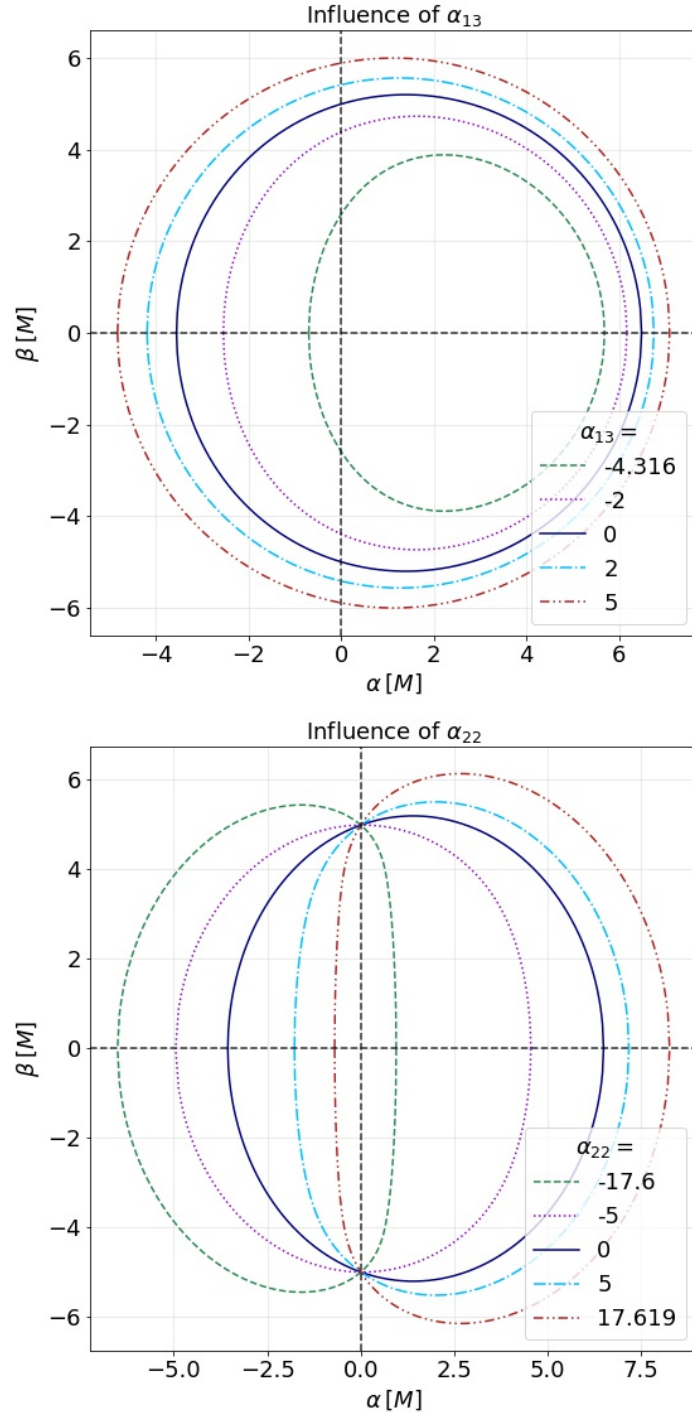


Figure 4.7: Influence of the parameters α_{13} and α_{22} on the shadow of a Johannsen BH, with $a = 0.7M$. Only one of the deviation parameters is switched on at a time. The parameter α_{52} does not influence the shadow, and is set to zero. The values $\alpha_{13} = -4.316$ and $\alpha_{22} = 17.619$ correspond to the limiting cases (2.35) and (2.34). The shadow of these limiting cases is "smaller than the horizon", as explained in the text.

Interestingly, we observe that the expression for $R(\rho)$ is not invariant under the transformation $\theta_0 \rightarrow \pi - \theta_0$. This indicates that the shadow is not the same when viewed from above as from below, for the simple reason that the spacetime itself is not invariant under the transformation $\theta \rightarrow \pi - \theta$. The shadow itself, as observed on the screen, is still equatorially symmetric⁵. This is a non-trivial result of the integrability of the geodesic equations [37], which we have explicitly demonstrated here for the almost-BPS metric. This effect can be seen in Figure 4.8. The constants of motion are given by (3.40, 3.39), and we have already explained how to find the range $[\rho_-^\gamma, \rho_+^\gamma]$ for bound orbits in section 3.3. Once again, the appropriate subrange should be considered for off-equatorial observers, such that only bound orbits that effectively reach $\theta = \theta_0$ are included.

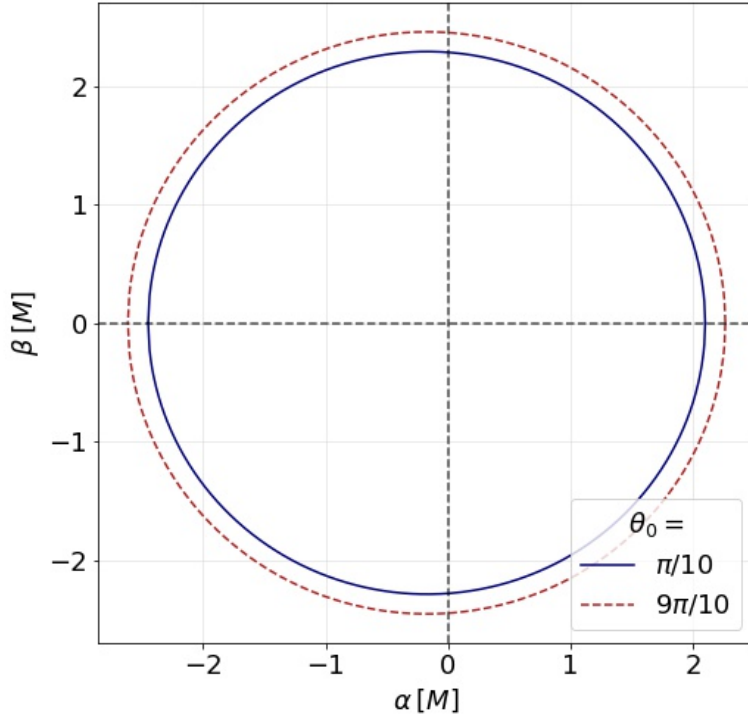


Figure 4.8: Difference in size of the almost-BPS black hole shadow for an observer located above or below the equatorial plane. The shadow itself still possesses equatorial symmetry. The parameters of the BH are $\mathbf{Q} = (2, 1, 1, 1) \cdot \zeta$, $\alpha = 1.3\zeta^2$, $h = 0.7$.

Figure 4.9 shows the effect of the spin parameter α and the parameter h on the shadow of the almost-BPS shadow. The metric parameters are rescaled so that $M = 1$, and therefore one should consider the relative size of the parameters. The effect of the spin is as expected from previous results, deforming the shadow with increasing absolute value of the spin. Note however that the sign of the parameter α is the opposite of what one would expect based on the previous sections. This is simply due to the definition (2.39).

⁵In chapter 6 we will briefly discuss black hole shadows that exhibit asymmetry in the shadow itself.

| Effect on the black hole shadow | Johannsen metric | almost-BPS metric |
|----------------------------------|------------------|-------------------|
| Compress the shadow horizontally | a, α_{22} | α |
| Change overall scale | q, α_{13} | h, Q_0, Q_I |

Table 4.1: Summary of the primary influence of the different parameters ($I = 1, 2, 3$) on the black hole shadow for the Johannsen and almost-BPS metrics. The Kerr-Newman metric is contained within the Johannsen metric. The inclination of the observer is not included, as it is no metric parameter.

The effect of h is clear: decreasing it compresses the shadow drastically.

Figure 4.10 shows what changing the charges does to the shadow. Again, the parameters are rescaled so that $M = 1$. The charges Q_2, Q_3 have the same influence on the shadow as Q_1 , since they are treated equally in the metric. The first observation we make is that for large values of the charge, the shadow is compressed for increasing charge. This is similar to the influence of the charge q in the Kerr-Newman metric (see Figure 4.5). However, note that for small values of the charge (satisfying the constraint (2.41)) the shadow grows in size along with an increasing charge. For these charges, that are small compared to α , the effect of the spin dominates. This is reflected in the apparent horizontal shift of the shadow, with respect to the vertical axis. In between both regimes, there is a range of charges in which the area of the shadow is maximized. The behaviour of the shadow size with respect to the charges is therefore not monotonic, unlike any parameter that we have discussed before.

The effect of the different metric parameters is summarized in Table 4.1. This table reflects how the BH shadow is subject to a large degree of degeneracy, as we have pointed out before. Therefore, we will present another observable in section 4.3, which can be used complementary to the shadow in order to determine the metric parameters.

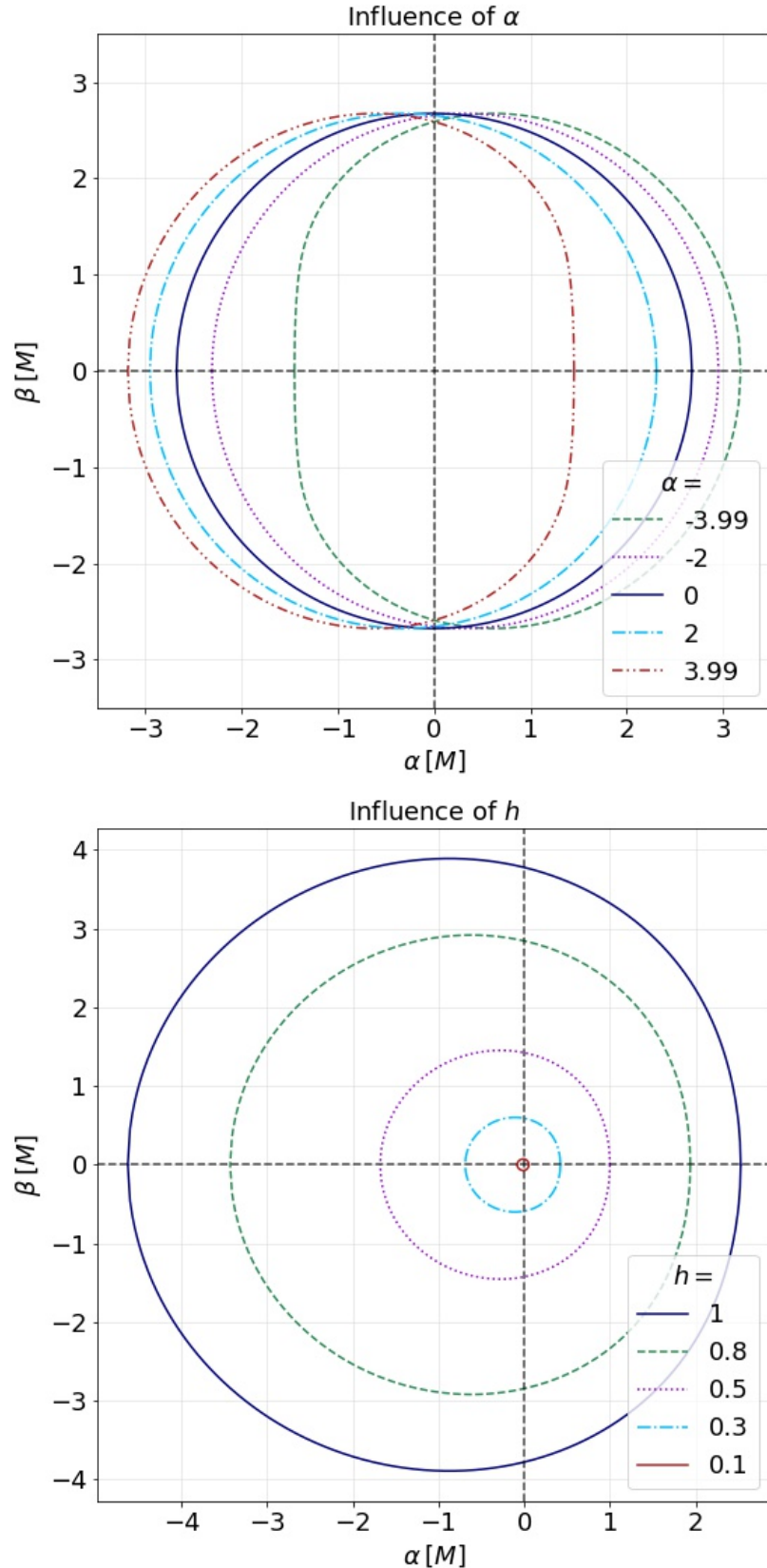


Figure 4.9: Influence of the spin α and parameter h on the almost-BPS black hole shadow. In the upper plot, the other BH parameters are $\mathbf{Q} = (2, 2, 2, 2) \cdot \zeta$, $h = 0.7$. The values form α in the legend of this plot are given before rescaling, and should be multiplied with ζ^2 . In the lower plot, the other BH parameters are $\mathbf{Q} = (2, 1, 1, 1) \cdot \zeta$, $\alpha = \zeta^2$.

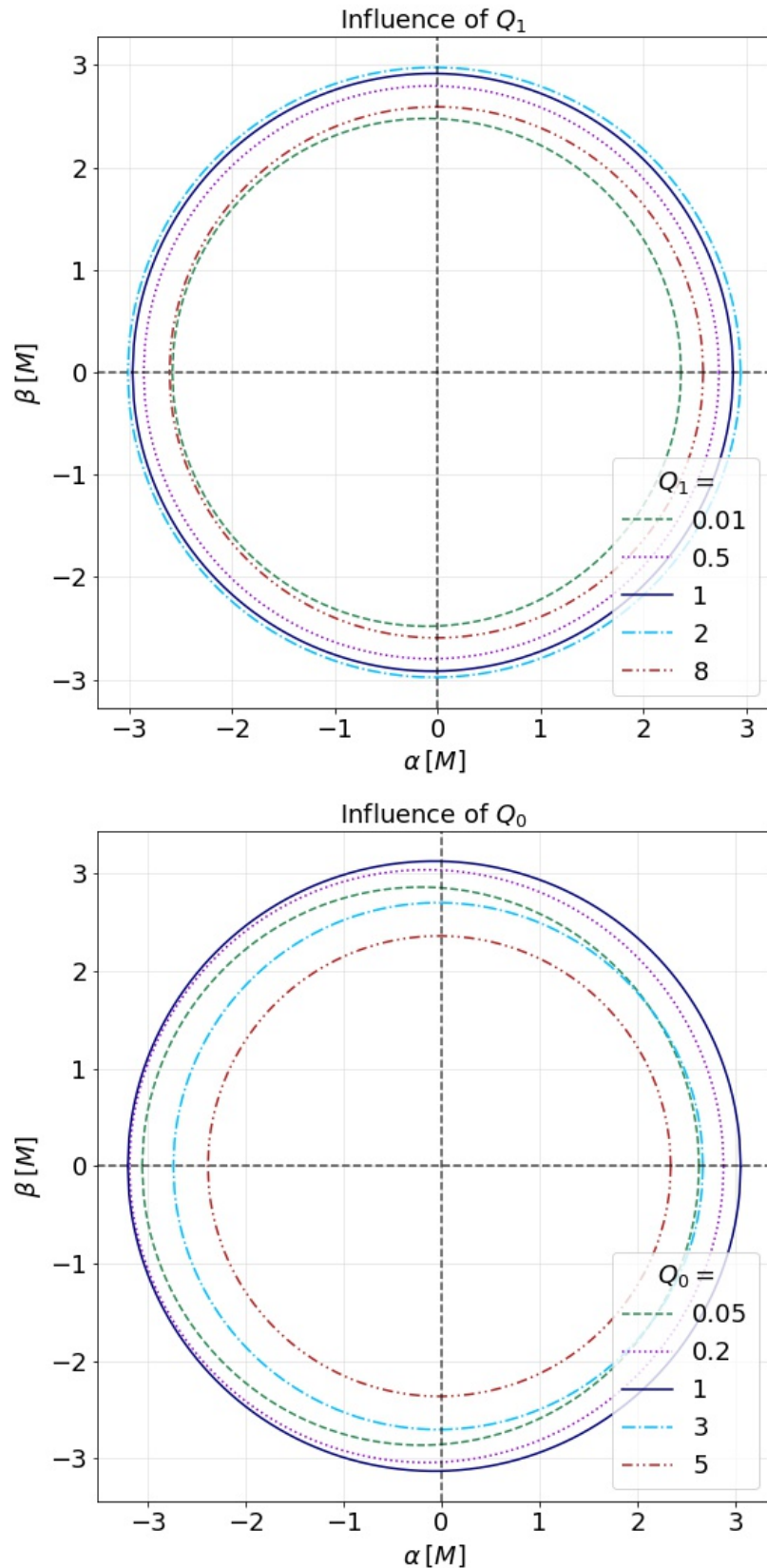


Figure 4.10: Influence of the charges Q_0, Q_1 on the almost-BPS black hole shadow. In the upper plot, the BH parameters are $\mathbf{Q} = (2, Q_1, 1, 1) \cdot \zeta$, $\alpha = 0.1\zeta^2$, $h = 0.8$. In the lower plot the BH parameters are $\mathbf{Q} = (Q_0, 1, 1, 1) \cdot \zeta$, $\alpha = 0.1\zeta^2$, $h = 0.8$.

4.2 Photon rings

Aside from the shadow that a BH projects on the observer screen, the light rays that escape the gravitational attraction contain a lot of information as well. The closer a geodesic comes to falling in, the closer to the shadow it will hit the observer screen. The geodesics that hit close to the shadow have completed many *orbits* around the BH. However, the concept of an orbit is ambiguous. In this section, two distinct approaches are presented to classify the null geodesics that escape in distinct *rings*. Regardless of the method, the general features remain the same. The shadow of a BH, which is lit either by a background source or an accretion disk, is surrounded by an infinite sequence of self-similar rings indexed by the number of orbits around the black hole. The width of these rings decreases exponentially in size, in a way that depends universally on the underlying spacetime. This exponential decay is characterized by the *Lyapunov exponent* γ . If measured accurately, this quantity provides a powerful probe of black hole spacetimes [50, 64].

4.2.1 Number of oscillations in polar direction

In a first instance, we will define an orbit with respect to the oscillation in the θ -direction. A full orbit corresponds to one full oscillation, e.g. from θ_- to itself in the notation of section 3.1.1. Classifying the geodesics with respect to this definition is the natural choice if we consider a black hole surrounded by an accretion disk, because each passage through the disk corresponds to half an orbit. The information in this section is found in [64], unless stated otherwise.

Consider two geodesics, one being a bound geodesic at a radius r_B and the other one initially slightly displaced from this bound one, with a separation equal to δr_0 . As will be shown in the next section, their separation δr_n after n half-orbits grows as

$$\delta r_n = e^{\gamma n} \delta r_0. \quad (4.16)$$

The parameter γ is called the *Lyapunov exponent*, and it quantifies the instability of the bound null geodesics in the photon sphere. The remainder of this chapter is devoted to its calculation.

As mentioned before, one half-orbit corresponds to one passage of the geodesic through the equator and a possible accretion disk. Assuming optically thin matter, this means that a light ray that completes n half-orbits can collect $\sim n$ times more photons in comparison to one that only completes one half-orbit. As a result, the intensity is expected to be larger by a factor $\sim n$. A visualization of two geodesics belonging to different photon rings is given in Figure 4.11 (left). The image on the cover page of this thesis corresponds to the trajectory of a $n = 4$ geodesic around a Kerr BH, where the red surface denotes the event horizon and the units on the axes are gravitational radii.

Focusing on the image screen, a light-ray that is aimed at a small distance δR outside the shadow edge at R_c will typically cross the equatorial plane a number of times on the order of

$$n \approx -\frac{1}{\gamma} \ln \frac{\delta R}{R_c}. \quad (4.17)$$

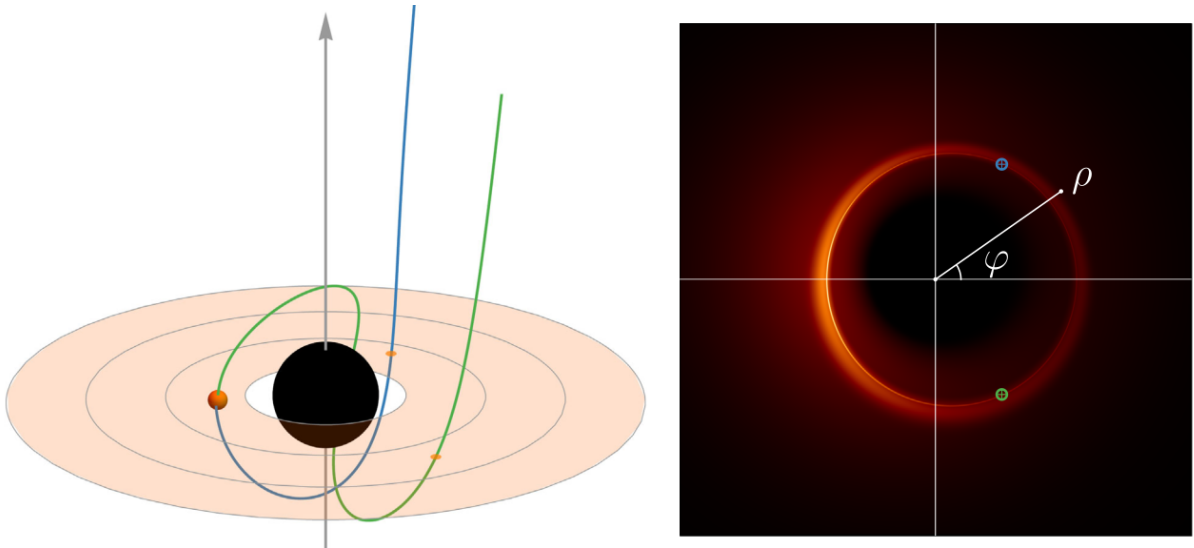


Figure 4.11: (*left*) Kerr BH with $a/M = 0.94$, surrounded by a geometrically and optically thin accretion disk. The small orange sphere is an emitting region in the disk, from which two light rays depart on distinct geodesic trajectories at equal times. The blue geodesic is part of the $n = 1$ photon ring, as it passes through the disk once after emission, whereas the green geodesic belongs to $n = 2$. (*right*) The black hole as seen by an observer located at $\theta_0 = 17^\circ$. The bright photon rings are clearly visible. The arrival points of the two geodesics on the observer screen are indicated. As the light rays can arrive at different times, a time-averaged image displays autocorrelations in the photon ring. Figure taken from [54].

Therefore, geodesics that complete n half-orbits must be aimed at a distance closer than

$$\delta R \approx e^{-\gamma n} R_c \quad (4.18)$$

to the black hole shadow edge. Therefore, the subrings do indeed decrease exponentially in width. It is with respect to this definition of orbit that we calculate the Lyapunov exponent γ for the different metrics of interest in section 4.3.

4.2.2 Number of orbits around the symmetry axis

The second approach uses a different definition of orbit. Now, we distinguish null geodesics by the change in azimuthal angle $\Delta\phi$ they have experienced. Consider a geodesic that comes in from infinity and escapes the gravitational pull after being deflected. Label its initial and final ϕ -coordinate as ϕ_i and ϕ_f , respectively. Note that the range of ϕ corresponds to the real numbers. The change in azimuthal angle is simply given by $\Delta\phi = \phi_f - \phi_i$. A geodesic that misses the BH by a large distance is barely affected by its gravity. For such a geodesic, the change in azimuthal angle will approximately be equal to $\Delta\phi = \pm\pi$, depending on the direction of travel. Therefore, we will work with the deflection angle $|\Delta\phi| - \pi$. We define the number of *azimuthal orbits* N_ϕ as

$$N_\phi = \frac{|\Delta\phi| - \pi}{2\pi}. \quad (4.19)$$

This can be any real number, which reflects the number of times that the geodesic has travelled an angle 2π around the axis of symmetry. Consider an observer at a large distance, at an angle ϕ_0 , and consider only geodesics that go to infinity in the direction ϕ_0 . We can then classify these geodesics into *rings*, based on the integer number of half-orbits n that have been completed, i.e.

$$n_\phi = \lfloor 2N_\phi \rfloor, \quad (4.20)$$

where the brackets denote the floor-function⁶. Essentially, defining the rings with respect to this criterion divides the spacetime far away from the black hole in two parts: one part from which geodesics with even n originate, and one part from which the odd- n geodesics depart.

It is also possible to divide the spacetime into different parts, by picking another value for the reference point in the deflection angle. For example, we can take

$$N_\phi = \frac{|\Delta\phi| - \frac{\pi}{2}}{2\pi}.$$

Using this new definition, the geodesics can still be classified into rings according to (4.20). This is shown in Figure 4.12, where the black geodesics correspond to $n = 0$, the orange ones to $n = 1$ and the red ones to $n = 2$. The two 'parts' in which the sky is divided correspond roughly to a part at the 'back side' of the BH, and one at the 'front side', with respect to the observer. This is interesting, as the rings now alternate between lensing the light originating from the back side and the light that comes from the front side. For that reason, this is a natural choice for a black hole in between an observer and, say, a galaxy. The galaxy will be visible in the even- n rings.

This will be the definition that we follow in chapter 5.

4.3 Lyapunov exponent

The goal of this section is to calculate the Lyapunov exponent, with respect to orbits as defined in section 4.2.1. First, the calculation for the Kerr metric is given, as derived in [64]. Subsequently, we present the extension to the metrics that we have been considering so far in this chapter. To this end, we will again consider photons on nearly bound geodesics, relying on results from the previous sections.

4.3.1 Kerr metric

Consider a photon on a nearly bound geodesic, i.e. initially at a radius $r = r_B + \delta r_0$ with $0 < \delta r_0 \ll 1$ and r_B in the open interval (r_-^γ, r_+^γ) of allowed bound orbits. We distinguish between the radial potential (3.3) for the bound orbit, i.e. with constants of motion given by (3.17, 3.18) at r_B , which we denote by $\mathcal{R}_B(r_B)$ and the radial potential $\mathcal{R}(r)$ for the nearly bound geodesic. The constants of motion of the nearly bound geodesic

⁶This function rounds a real number r to the largest integer k with $k \leq r$.

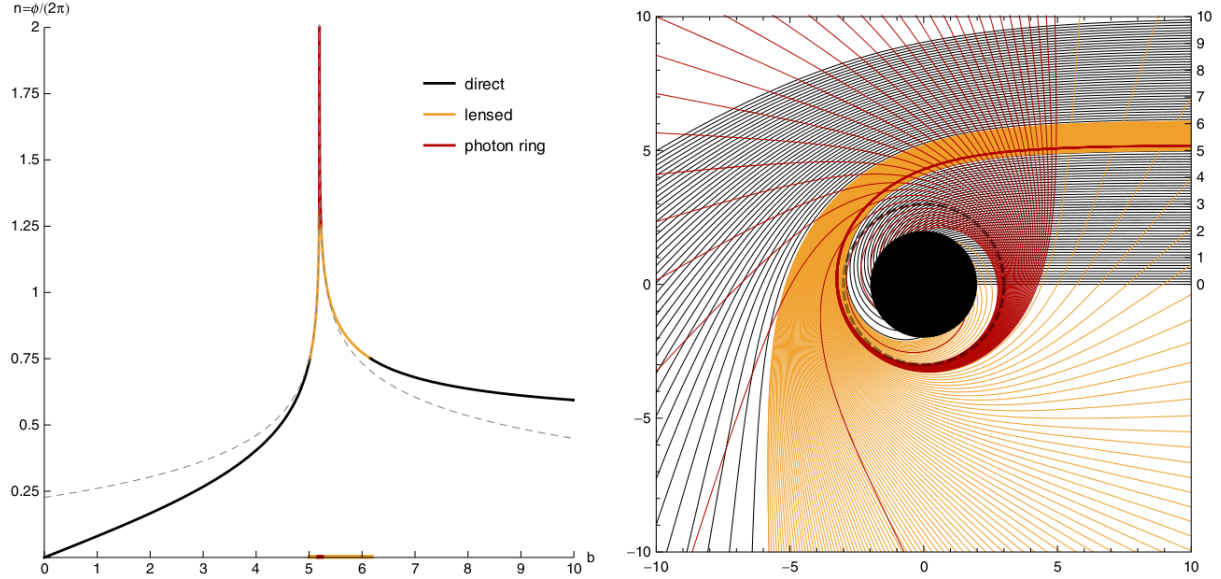


Figure 4.12: Visualization of the subdivision of null geodesics in different photon rings along the criterion for the azimuthal angle. The metric used here is Schwarzschild, but the idea extends to other black holes. (*right*) The trajectory of different geodesics that start out from infinity (where the observer is located, to the right) with an impact parameter b in the range $[0,10]$. The coordinates r, θ are treated as Euclidean polar coordinates. The geodesics are colored depending on where they end up after lensing. The dashed black circle corresponds to the critical radius (bound photon orbit), beyond which photons coming from infinity fall in. (*left*) The fractional number of orbits n as a function of the impact parameter. The solid line is the exact value, whereas the dashed line is an approximation that is not relevant here. This is Figure 2 in [49].

approximately match those of the bound one. Therefore, both radial potentials are very similar. This means that we can approximate

$$\mathcal{R}(r) \approx \frac{1}{2} \mathcal{R}''(r_B) (\delta r_0)^2 ,$$

since $\mathcal{R}_B(r_B) = \mathcal{R}'_B(r_B) = 0$. Let the photon start in the equatorial plane. After n half-orbits, the photon has advanced to the (slightly) larger radius $r_B + \delta r_n$, such that according to (3.6)

$$\int_{r_B + \delta r_0}^{r_B + \delta r_n} \frac{dr}{\sqrt{\mathcal{R}(r)}} \approx n G_\theta(r_B) . \quad (4.21)$$

We can now approximate the radial integral as

$$\begin{aligned} \int_{r_B + \delta r_0}^{r_B + \delta r_n} \frac{dr}{\sqrt{\mathcal{R}(r)}} &\approx \int_{r_B + \delta r_0}^{r_B + \delta r_n} \frac{dr}{\sqrt{\frac{1}{2} \mathcal{R}''(r_B) (r - r_B)^2}} \\ &= \sqrt{\frac{2}{\mathcal{R}''(r_B)}} \int_{r_B + \delta r_0}^{r_B + \delta r_n} \frac{dr}{r - r_B} \\ &= \sqrt{\frac{2}{\mathcal{R}''(r_B)}} \ln \left(\frac{\delta r_n}{\delta r_0} \right) . \end{aligned}$$

So, we find that

$$\frac{1}{n} \ln \left(\frac{\delta r_n}{\delta r_0} \right) = \sqrt{\frac{\mathcal{R}''(r_B)}{2}} G_\theta(r_B). \quad (4.22)$$

This proves the statement (4.16), and we note that the left-hand side is precisely the Lyapunov exponent γ . Plugging in the expressions (3.3, 3.17, 3.18) gives

$$\frac{\mathcal{R}''(r)}{8} = r^2 - \frac{Mr\Delta}{(r-M)^2}. \quad (4.23)$$

So, using (3.11) we find that the **Lyapunov exponent for the Kerr metric** is given by

$$\gamma(r) = \frac{4}{a} \sqrt{r^2 - \frac{Mr\Delta}{(r-M)^2}} \frac{1}{\sqrt{-u_-}} K \left(\sqrt{\frac{u_+}{u_-}} \right). \quad (4.24)$$

Other than the metric parameters a and M , the only variable in this expression is the radial coordinate r . The BH shadow is parametrized by the same variable, which means that we can combine (4.12) and (4.24) into a parametric curve $\gamma(\phi_\rho)$. This curve describes the variation of the Lyapunov exponent as we go along the BH shadow. Interestingly, this means that every angle on the observer screen probes the structure of the metric at a specific radial coordinate r .

For the Schwarzschild metric, the Lyapunov exponent is equal to π for all angles. This can be obtained as the limit of (4.24) for $a \rightarrow 0$. For the Kerr metric with $a \neq 0$, the behaviour of γ in function of the on-screen angle is not constant. This can be seen in Figure 4.13.

For large values of the spin, the variation of the Lyapunov exponent along the shadow is large. For an observer in the equatorial plane, the boundary values of this curve are always equal to π . In between, the function shows a local minimum that gets more pronounced as the spin increases. We do not show the curve for an extremal BH with $a = M$, as the method we discussed only applies to the 'curved part' of its shadow. The vertical line, as discussed at the end of section 4.1, requires a special treatment not discussed here. The resulting curve can be found in Figure 6 of [64]. It is a limiting case of the ones that are shown here, where the minimum is stretched all the way to $\gamma = 0$.

The relation (4.24) does not depend on the coordinates of the observer. This makes sense, since γ is a property of the bound null geodesics in the photon sphere which is independent of any observer. On the other hand, the range of r -values that contributes to the shadow on the observer screen is dependent on the observer's inclination θ_0 (see 3.22). This range of r is 'smeared out' over the black hole shadow, and as a consequence this is also the case for the Lyapunov exponent. Therefore, the information in the function $\gamma(\phi_R)$ for an off-equatorial observer will always be 'contained' within the function $\gamma(\phi_R)$ as determined by an equatorial observer. This is indicated in Figure 4.13 by means of the dashed lines: they show which part of the function $\gamma(\phi_R)$ as determined by the equatorial observer is seen by an observer at an inclination $\theta_0 = 17^\circ$.

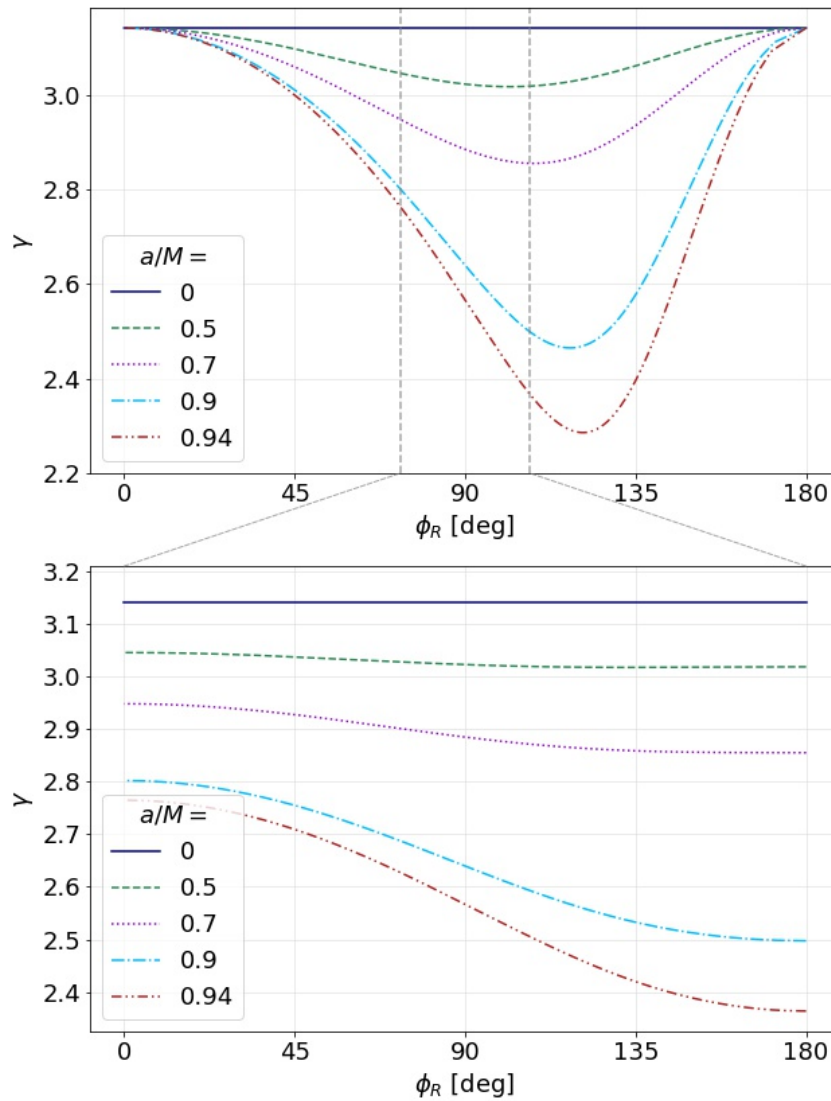


Figure 4.13: The Lyapunov exponent γ as function of the on-screen angle ϕ_R for different values of the spin parameter a/M in the Kerr metric. (bottom) An observer located at an inclination $\theta_0 = 17^\circ$ determines a function that is contained within (top) the function as determined by an equatorial observer.

The position of these boundaries can be determined analytically. Consider two observers at a distance r_0 , one in the equatorial plane and the other one at an inclination θ^* . For the inclined observer, the geodesics that hit the horizontal axis on the observer screen at $\beta = 0$ obey the relation

$$(\lambda^*)^2 = \eta^* \tan^2 \theta^* + a^2 \sin^2 \theta^*. \quad (4.25)$$

Since λ^* is a quantity associated with the geodesic itself and not with the observer, we can use this expression to determine where the equatorial observer registers this geodesic on their screen. Using the expressions (4.11, 4.12) with $\theta_0 = \pi/2$, we find that a geodesic subject to (4.25) hits the screen of the equatorial observer at

$$\begin{aligned} R^* &= r_0^{-1} \sqrt{a^2(1 + \sin^2 \theta^*) + \eta^* \sec^2 \theta^*}, \\ \phi_R^* &= \arccos\left(-\frac{\lambda^*}{R^* r_0 \sin \theta^*}\right). \end{aligned}$$

We can rewrite the second relation as

$$\sin\left(\frac{\pi}{2} - \phi_R^*\right) = \pm \sin(\theta^*) \sqrt{1 - \frac{a^2 \sin^2 \theta^*}{a^2(1 + \sin^2 \theta^*) + \eta^* \sec^2 \theta^*}}. \quad (4.26)$$

If we assume that the second term in the square root is small, we can approximate

$$\sin\left(\frac{\pi}{2} - \phi_R^*\right) \approx \pm \sin(\theta^*),$$

with the result that

$$\phi_R^* \approx \left(\frac{\pi}{2} \pm \theta^*\right) \bmod \pi. \quad (4.27)$$

This approximation is better⁷ for values of the spin close to zero or observers close to the poles, where it becomes exact. Looking back at the example in Figure 4.13, this approximation tells us that the observer at $\theta_0 = 17^\circ$ observes the part of the plot for the equatorial observer that is contained between approximately 73° and 107° . We will come back to this approximation in Chapter 6. We conclude that we can restrict to observers in the equatorial plane if we want to study this Lyapunov exponent for the Kerr metric. This conclusion, the equation (4.26) and the approximation (4.27) have not been explicitly remarked on in the literature.

4.3.2 Extension to Kerr-Newman

We have seen in section 3.1.3 that the analysis does not change much by including the charge q . The second derivative of the radial potential $\mathcal{R}(r)$ is still given by (4.23), now including the charge q in Δ . The rest of the calculation remains unchanged, and we have also seen that the angular integral is of the same form (section 3.1.3). The conclusion is that the Lyapunov exponent for Kerr-Newman is still given by (4.24), but the functional dependencies of u_\pm on r have changed to (3.25), and Δ includes the charge as well. The result (4.26) still holds.

⁷We have explicitly checked this approximation for a few models. The largest deviation we have encountered between the exact value for ϕ_R^* and the approximation (4.27) was on the order of 2° .

The effect of the charge on the Lyapunov exponent is shown in Figure 4.14. In the case where $a = 0$, the function is still constant, but its value depends on the charge: increasing the charge lowers γ . This effect is also seen when we include spin, as is shown in the bottom plot. But, as the spin is non-zero the function is no longer constant. The minimum is once again more pronounced when the BH gets closer to extremality.

4.3.3 Johannsen metric

Section 3.2 showed that the calculations for the Johannsen metric resemble those for Kerr. The relation (3.27) is different, but we can still approximate the radial integral. As $A_5(r)$ is strictly positive outside the horizon, the zeroes of the denominator in the radial integral are still the zeroes of $\mathcal{R}(r)$. So, for a nearly-bound geodesic at radius $r = r_B + \delta r_0$ we have that

$$(A_5 \cdot \mathcal{R})(r) \approx \frac{1}{2} A_5(r_B) \cdot \mathcal{R}''(r_B) (\delta r_0)^2 .$$

After n half-orbits, we approximate the radial integral

$$\int_{r_B + \delta r_0}^{r_B + \delta r_n} \frac{dr}{\sqrt{A_5(r)\mathcal{R}(r)}} \approx \sqrt{\frac{2}{A_5(r_B) \cdot \mathcal{R}''(r_B)}} \ln \left(\frac{\delta r_n}{\delta r_0} \right) . \quad (4.28)$$

From the expressions (3.26, 3.28, 3.29) the second derivative of the radial potential $\mathcal{R}''(r)$ for a bound orbit can be calculated, but the analytic expression is cumbersome. It was also shown that the angular integral remains of the same form (3.11). We have to take the new expressions for u_{\pm} into account, which can also be found analytically. However, these expressions are too long and cumbersome to write down here, and they do not provide any additional insight.

The **Lyapunov exponent for the Johannsen metric** is thus given by

$$\gamma(r) = \frac{1}{a} \sqrt{-\frac{2A_5(r)\mathcal{R}''(r)}{u_-}} K \left(\sqrt{\frac{u_+}{u_-}} \right) ,$$

(4.29)

parametrized over the range $[r_-^\gamma, r_+^\gamma]$, which has to be determined numerically.

Having studied the apparent shape of the BH shadow in (4.1.2), we can again determine the parametric curve $\gamma(\phi_R)$. The effect of the different parameters on the Lyapunov exponent are shown in Figure 4.15.

First of all, the parameter α_{52} does have a measurable influence now: increasing it makes the Lyapunov exponent grow overall. It does so in an angle-dependent way, meaning that the value in 0 and π no longer need to be equal.

The influence of α_{22} is again similar to the effect of changing the spin. The function gets a more pronounced minimum for large values of the deviation parameter. For large absolute values, the exponent becomes very large but remains finite, which is not shown

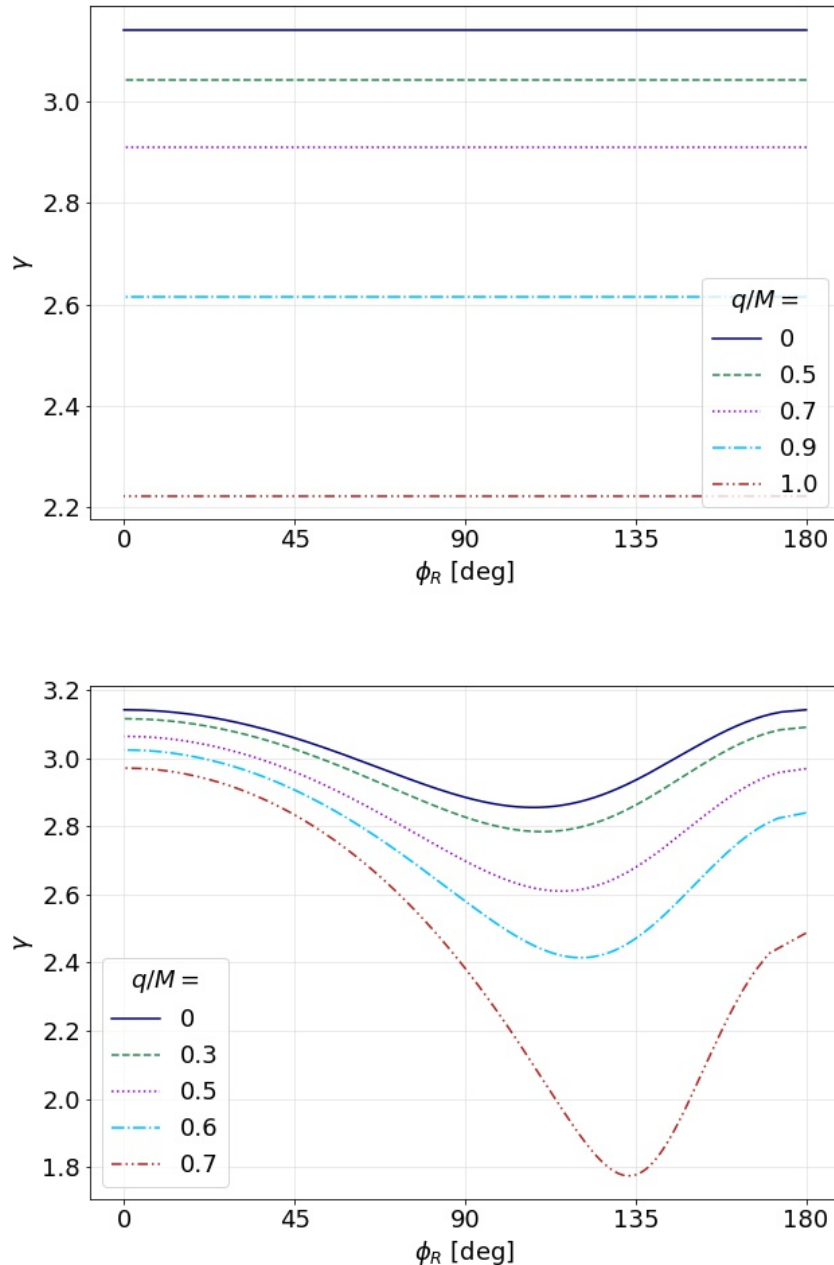


Figure 4.14: The Lyapunov exponent in function of the on-screen angle ϕ_R , for varying values of the charge q (*top*) in the Reissner-Nordström metric and (*bottom*) in the Kerr-Newman metric with $a/M = 0.7$. The observer is located in the equatorial plane.

on the plot for clarity. The curve corresponding to $\alpha_{22} = 17.619$ reaches a value $\gamma \approx 4734$ in $\phi_R = \pi$. This is due to the upper limit (2.34) being nearly saturated.

The effect of α_{13} is not very pronounced for positive values of this parameter. For negative values, however, the exponent becomes large when $\phi_R \rightarrow \pi$. In the case $\alpha_{13} = -4.316$, just slightly above the lower bound (2.35), the curve reaches a value $\gamma \approx 549$ for $\phi_R \rightarrow \pi$.

Finally, we note that the result (4.26) still holds, since the expressions for the impact parameters (4.7, 4.8) are unchanged.

4.3.4 Almost-BPS metric

Finally, we calculate the Lyapunov exponent for the almost-BPS black hole. The general approach is once again very similar, but the calculations do not immediately carry over from the Kerr and Johannsen metric. The procedure is clear though: we calculate the angular integral, and approximate the radial integral.

From the expressions (3.34, 3.39, 3.40), we obtain the second derivative of the radial potential for a bound geodesic

$$\mathcal{R}''(\rho) = -2\frac{\alpha^2}{\rho^2} + 6\rho^2 + Q_0 \left(2\frac{Q_1 Q_2 Q_3}{\rho^2} + \frac{2\rho}{h^3} \right) + 2\frac{Q_1 + Q_2 + Q_3}{h}\rho. \quad (4.30)$$

The equation (3.38) still holds, and so we have that

$$\gamma(\rho) = \sqrt{\frac{\mathcal{R}''(\rho)}{2}} G_\theta(\rho).$$

(4.31)

As mentioned in section 3.3, the angular integral (3.41) is calculated numerically by determining the zeroes of $\Theta(\theta)$ and integrating between them. Using the equations (4.14, 4.15) we can again transform (4.31) into a parametric curve $\gamma(\phi_R)$. Since the shadow is still symmetric with respect to the equatorial plane, we can again restrict to $\phi_R \in [0^\circ, 180^\circ]$.

Contrary to the other metrics we discussed, the equatorial plane is no longer the preferred location for an observer. It follows from the discussion in section 3.3 that the full range $[\rho_-^\gamma, \rho_+^\gamma]$ is only observed at a certain angle θ_m that typically differs from $\pi/2$. Ideally, we would therefore plot the curve $\gamma(\phi_R)$ as perceived by an observer at this specific inclination. The curves obtained at different polar angles are contained within the curve for this specific observer, since the shadow at a general inclination is determined by a subrange of $[\rho_-^\gamma, \rho_+^\gamma]$. However, we will present the plots for an observer in the equatorial plane, since changing the parameters of the spacetime changes the angle θ_m , which is not ideal for comparison between different models.

Figures 4.16 and 4.17 show the influence of the different metric parameters on the curve. Recall that these parameters are subject to rescaling such that $M = 1$, meaning that the parameters in the following figures should be considered relative to each other.

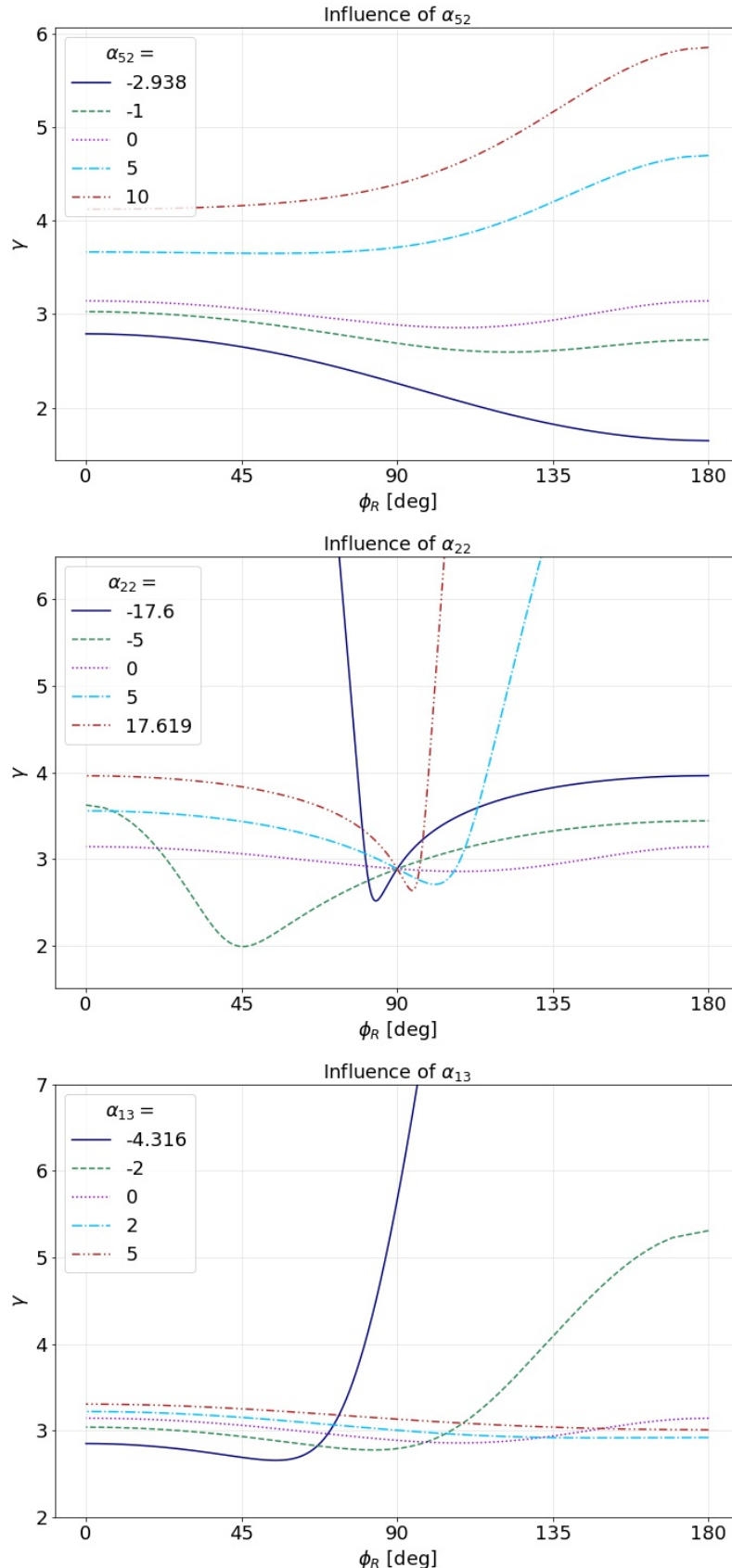


Figure 4.15: The Lyapunov exponent in function of the on-screen angle ϕ_R , for varying values of the deviation parameters α_{13} , α_{22} , α_{52} in the Johannsen metric. In all cases, only one deviation parameter is non-zero, and the spin is equal to $a = 0.7M$. The observer is located in the equatorial plane.

| Effect on the Lyapunov exponent | Johannsen metric | almost-BPS metric |
|---|----------------------------|-------------------|
| Make the minimum more pronounced | a, q, α_{22} | α |
| Change the value in $\phi_R = 0, \pi$ equally | q | h |
| Change the value in $\phi_R = 0, \pi$ differently, in opposite direction | α_{13} | / |
| Change the value in $\phi_R = 0, \pi$ differently, in the same direction | α_{22}, α_{52} | Q_0, Q_I |

Table 4.2: Summary of the primary influence of the different parameters ($I = 1, 2, 3$) on the black hole shadow for the Johannsen and almost-BPS metrics. The Kerr-Newman metric is contained within the Johannsen metric. The inclination of the observer is not included, as it is no metric parameter.

The effect of the spin parameter α is as expected from the previous cases, giving rise to a minimum that is more pronounced for large absolute values of the spin. The boundary values are fixed to a value that depends on the other metric parameters.

The parameter h has a rescaling effect on the curve, similar to its effect on the black hole shadow (see Figure 4.9).

The influence of the charges is non-monotonic, as was the case for the shadow (see Figure 4.10). The plots also show that decreasing the charge leads to metrics in which the spin dominates due to the rescaling process: this manifests itself through the non-constant behaviour of the function.

A summary of the effects of the different parameters in the Johannsen and almost-BPS metrics on the Lyapunov exponent are summarized in Table 4.2. Comparing this to Table 4.1, we note that the Lyapunov exponent can indeed be used to break the degeneracy associated with the black hole shadow.

The approximation (4.27) is still valid⁸, as we can derive a relation that is similar in spirit to (4.26). The angles ϕ_R^* , between which an observer located in the equatorial plane⁹ observes the information contained in the curve $\gamma(\phi_R)$ as determined by an observer at an inclination θ^* , are given by

$$\sin\left(\frac{\pi}{2} - \phi_R^*\right) = \pm \sin(\theta^*) \sqrt{1 - \frac{2m_\infty \alpha \cos \theta^*}{\chi}}. \quad (4.32)$$

The approximation (4.27) thus becomes more accurate when $\alpha \rightarrow 0$ or $h \rightarrow 1$ (as this

⁸Again, the models we have tested so far show differences between the exact and approximate values of no more than a few degrees.

⁹As mentioned before, the equatorial plane is no longer the preferred position, so it may be more sensible to do this exercise for an observer located at θ_m . This is done in the same way, but the answer contains a few more terms since $\cos \theta_m$ need not be zero. Also, for the metric parameters studied in this research, the angle θ_m was approximately equal to $\pi/2$ (but crucially, not exactly).

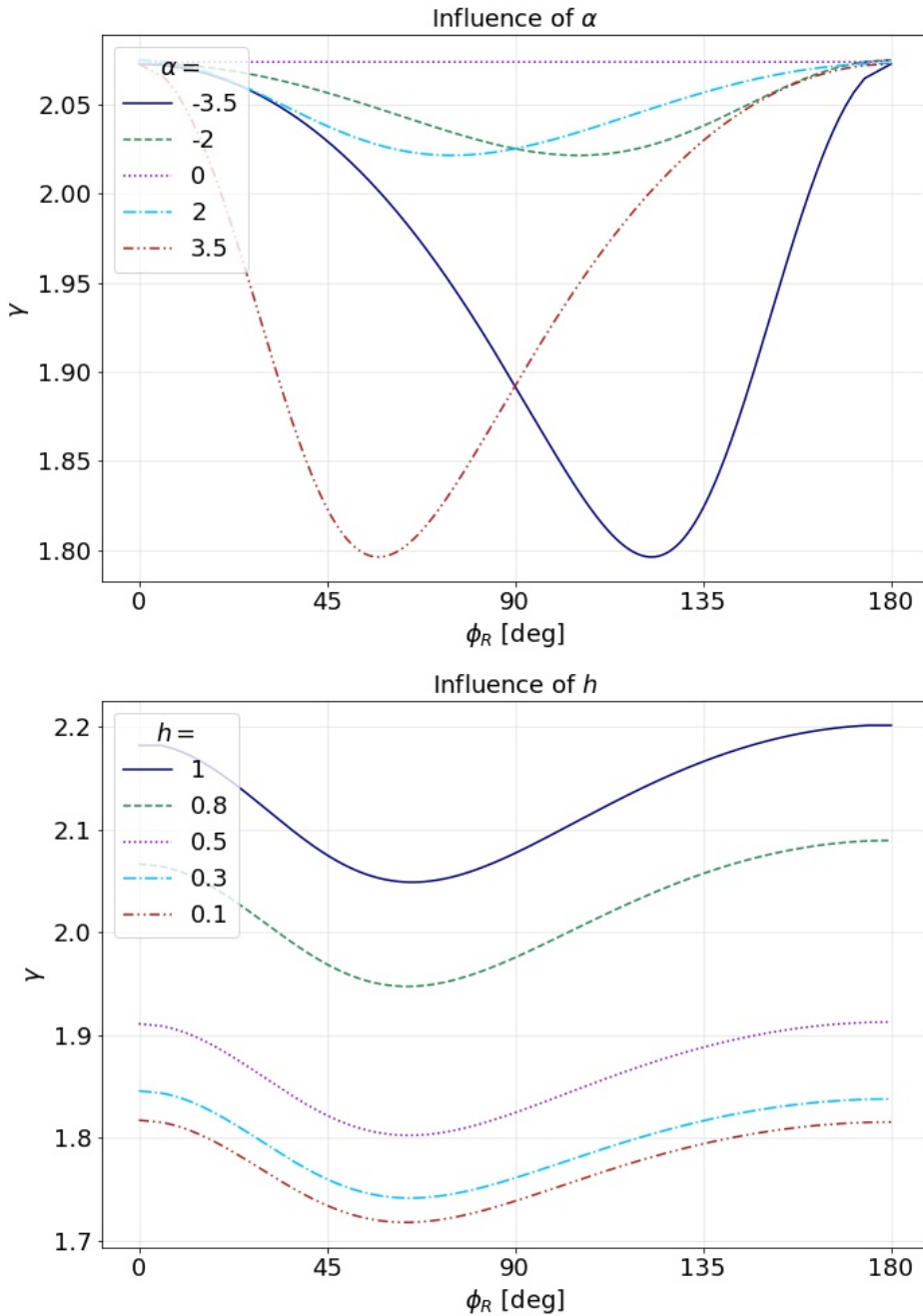


Figure 4.16: The Lyapunov exponent in function of the on-screen angle ϕ_R , for varying values of h and the spin parameter α in the almost-BPS metric. In the upper plot, the other BH parameters are $\mathbf{Q} = (2, 2, 2, 2) \cdot \zeta$, $h = 0.7$. In the lower plot, the other BH parameters are $\mathbf{Q} = (2, 1, 1, 1) \cdot \zeta$, $\alpha = \zeta^2$.

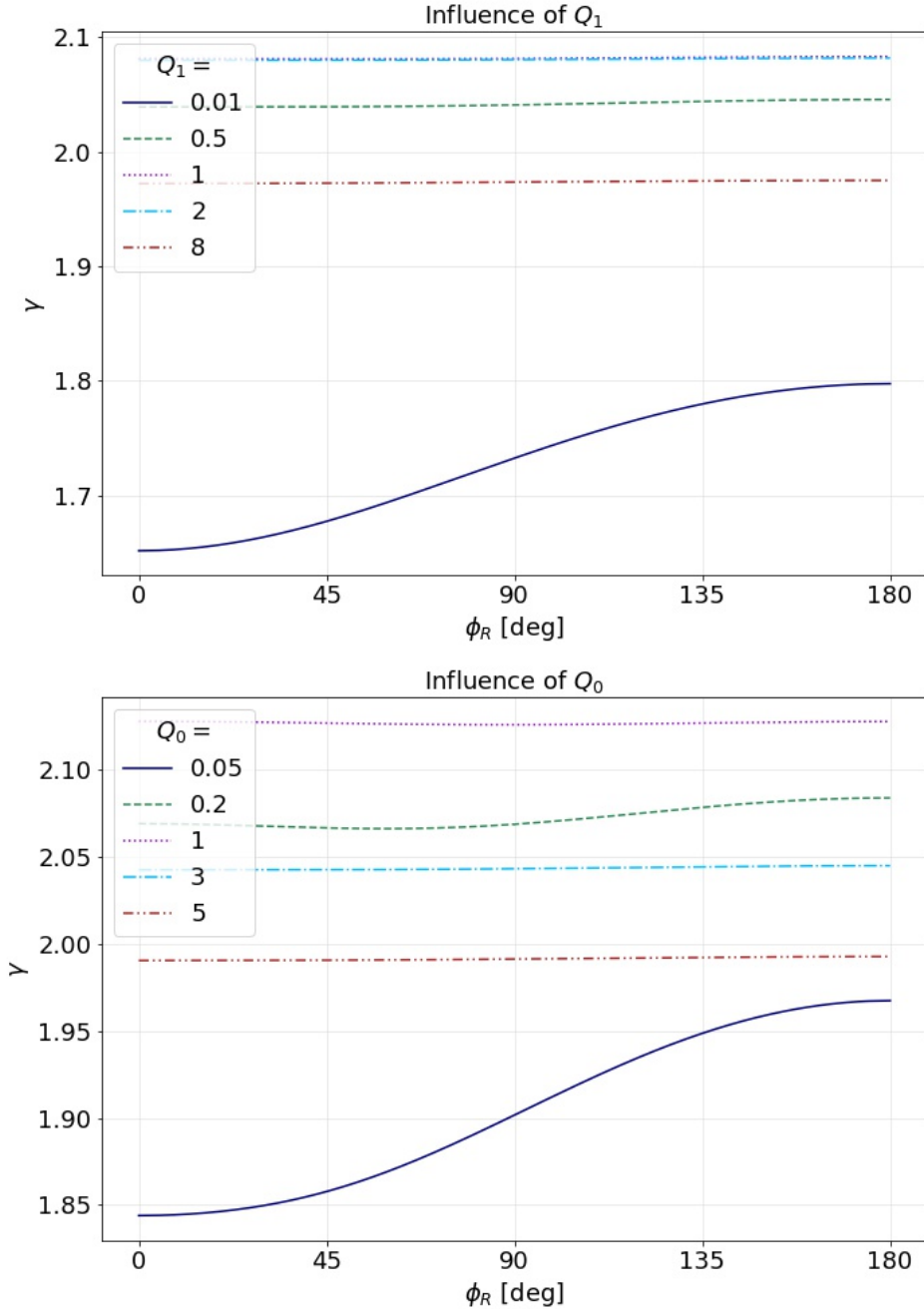


Figure 4.17: The Lyapunov exponent in function of the on-screen angle ϕ_R , for varying values of the charges Q_0, Q_1 in the almost-BPS metric. In the upper plot, the BH parameters are $\mathbf{Q} = (2, Q_1, 1, 1) \cdot \zeta$, $\alpha = 0.1\zeta^2$, $h = 0.8$. In the lower plot the BH parameters are $\mathbf{Q} = (Q_0, 1, 1, 1) \cdot \zeta$, $\alpha = 0.1\zeta^2$, $h = 0.8$. In the upper plot, the curves for $Q_1 = 1, 2$ approximately coincide.

implies $m_\infty \rightarrow 0$).

Chapter 5

Ray Tracing

An advantage of the BH metrics we have considered so far is that they can be studied with a semi-analytical approach. We have seen that the geodesic equations are integrable due to the existence of sufficient conserved quantities, which has enabled us to derive the results that have been presented so far. However, many spacetimes of interest are less well-behaved. The previous calculations become much harder - if not impossible - when only two conserved quantities are present. Therefore, this chapter aims to present a numerical approach to the questions we have addressed so far. In section 5.1 we explain the basics of ray tracing, and present the `RAPTOR` code which we will employ. Section 5.2 presents the comparison of the BH shadow as obtained by `RAPTOR` and the semi-analytic results of section 4.1. Subsequently, we investigate the possibility of extracting photon rings from these ray-traced images, and see if we can estimate the Lyapunov exponent.

5.1 Numerical ray tracing with RAPTOR

The central idea to ray tracing is that we position an observer at the edge of a celestial sphere, centered around the object of interest [3, 50]. We then follow geodesics starting at the observer's position in their motion towards the center, with the observer's view covering a certain solid angle on the observer sky (see Figure 5.1). Additionally, we register where the geodesics end up on the celestial sphere. If a geodesic escapes the gravitational pull of the BH within a maximum integration time, it will end up on the celestial sphere again. The celestial sphere is divided into four regions, represented by different colors. If a geodesic does not reach the celestial sphere within this integration time, it is colored black. This is normally¹ due to the geodesic falling into the event horizon.

Given that the geodesic equations (2.6) are time-reversible, the light rays that depart from the observer, ending up in a specific point on the celestial sphere, correspond equally well to light rays originating from that point and ending up at the camera. Therefore, a ray-traced image can also be interpreted as depicting the origin of a set of light rays captured by the camera.

¹In principle, this can also be the case for geodesics that orbit the BH for a very long time. They have an impact parameter very close to the critical one. In order to make sure only infalling geodesics are colored black, we repeat the experiments with increasing maximum integration time until the obtained image does not vary anymore.

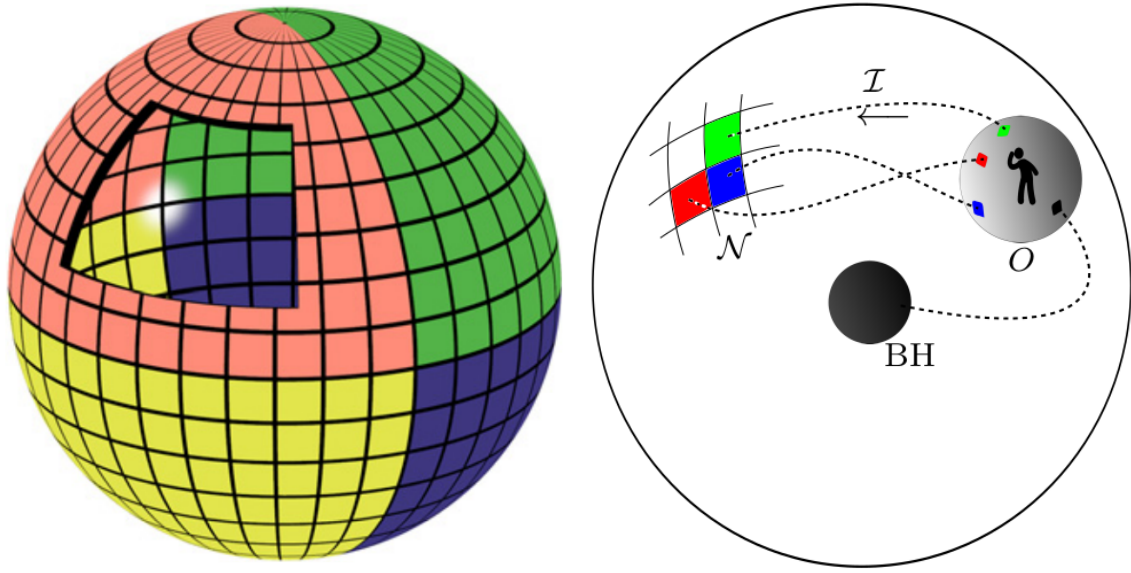


Figure 5.1: (*left*) Visualization of the celestial sphere in the geometry of ray tracing. The four colors represent different parts of the sphere, and the observer is located on the great circle that divides the sphere in a left and right half. When a BH is placed in the center of the celestial sphere, the equatorial plane will correspond to the one that divides the circle in an upper half and lower half. In this way, the sphere is naturally divided in 4 quadrants. The attribution of colors is arbitrary, and does not correspond to the images produced in this project (we fix the colors in Figure 5.2). Figure taken from [11]. (*right*) Formal correspondence between the different elements in the geometry of ray tracing. The observer has a local sky \mathcal{O} , in which it observes a certain solid angle. The patches in this local sky map to different parts of the celestial sphere \mathcal{N} , surrounding the observer and the BH. The map $\mathcal{I} : \mathcal{O} \rightarrow \mathcal{N}$ is not well defined in the presence of a BH, as some patches of \mathcal{O} correspond to light rays that would have originated from the BH. Figure taken from [36].

It is enlightening to look at some example images. Figure 5.2 shows a picture of flat space versus that of a Kerr BH. Note that the flat space image defines the color of the quadrants as we use them throughout this chapter. The image essentially shows that, in flat space, what is emitted in the direction of a certain quadrant will end up in that same quadrant. This changes drastically when a BH is placed in the middle of the sphere. The equatorial plane associated with the black hole corresponds to the plane that separates the blue and yellow quadrants from the red and green quadrants. The inclusion of this BH has some interesting effects. The most prominent feature is of course the BH shadow in the middle of the figure. This corresponds to the light rays that end up inside the event horizon in the process of backwards ray tracing. Second of all, the colors in the corners no longer correspond to those of flat space. The reason is that light rays aimed at the BH (perpendicular to the page) deviate at least a little bit, changing their course to end up in another quadrant. If we would zoom out further, we would eventually see that the corners correspond again to their original colors. Furthermore, peculiar features appear just outside the BH shadow. There is a green zone between the large red zone and the

shadow, where the geodesics experience strong lensing. Even more structure can be seen close to the Kerr shadow, which can be further resolved at high resolution.

The appearance of a black hole, as determined with a ray-tracing code, helps to visualize how the null geodesics behave in its strong gravitational field. Before we start analyzing the images of the different BH metrics in section 5.2, we present the *RAPTOR* code that was used throughout this project.

5.1.1 The *RAPTOR* code

RAPTOR is a public code capable of imaging relativistic plasmas in strong gravity regimes. The developers have published two accompanying papers [14, 15], which are the main reference for this section. The code calculates the trajectory of light rays by numerically integrating the geodesic equations (2.6) that govern them. Also, it is capable of performing time-dependent radiative transfer calculations along the rays, allowing the study of spectra of these relativistic plasmas. The use of the code extends beyond the study of light propagation in BH spacetimes, as it can also be used, for example, to investigate radiative transfer near neutron stars or even the propagation of radiation in expanding FLRW-universes. It can be applied to any analytical or numerical metric, making it an ideal numerical probe for complicated spacetimes. Interestingly, *RAPTOR* was one of the codes used to make simulations for the EHT [20]

The code itself is implemented in the programming language C, making it very fast while still maintaining a high level of accessibility. Making basic changes to the code is thus fairly straightforward, which is advantageous when implementing complicated metrics like the Johannsen and almost-BPS BHs. The code can be compiled both on CPUs and GPUs, irrespective of the hardware. It is OMP-parallelized, meaning that the code can run on multiple computing threads at once. This speeds up the calculations by large factors. Furthermore, the code is designed to efficiently work in various coordinate systems, not just in BL coordinates. We will focus in particular on the propagation of light rays in BH spacetimes, meaning that we will not exploit the radiative transfer features that the code provides.

To initialize a simulation, we fix the distance to the celestial sphere and the observer, and determine a solid angle that the observer investigates in its local sky. In our simulations, these distances are fixed to 2500 and 1500 gravitational radii², respectively. These values are mostly arbitrary, provided that they are much larger than the typical size of the horizon. The solid angle is varied according to what order n of photon rings is of interest. For images that encompass the entire shadow and the low- n rings, the solid angle was usually fixed to observe a patch corresponding to 15 by 15 gravitational radii at the distance of the BH. Finally, the number of geodesics being followed towards the BH needs to be specified. The solid angle is then equally divided into the required amount of pixels, such that each pixel corresponds to one geodesic.

²Recall that one gravitational radius corresponds to $r = M$ in natural units, as explained in section 2.1.

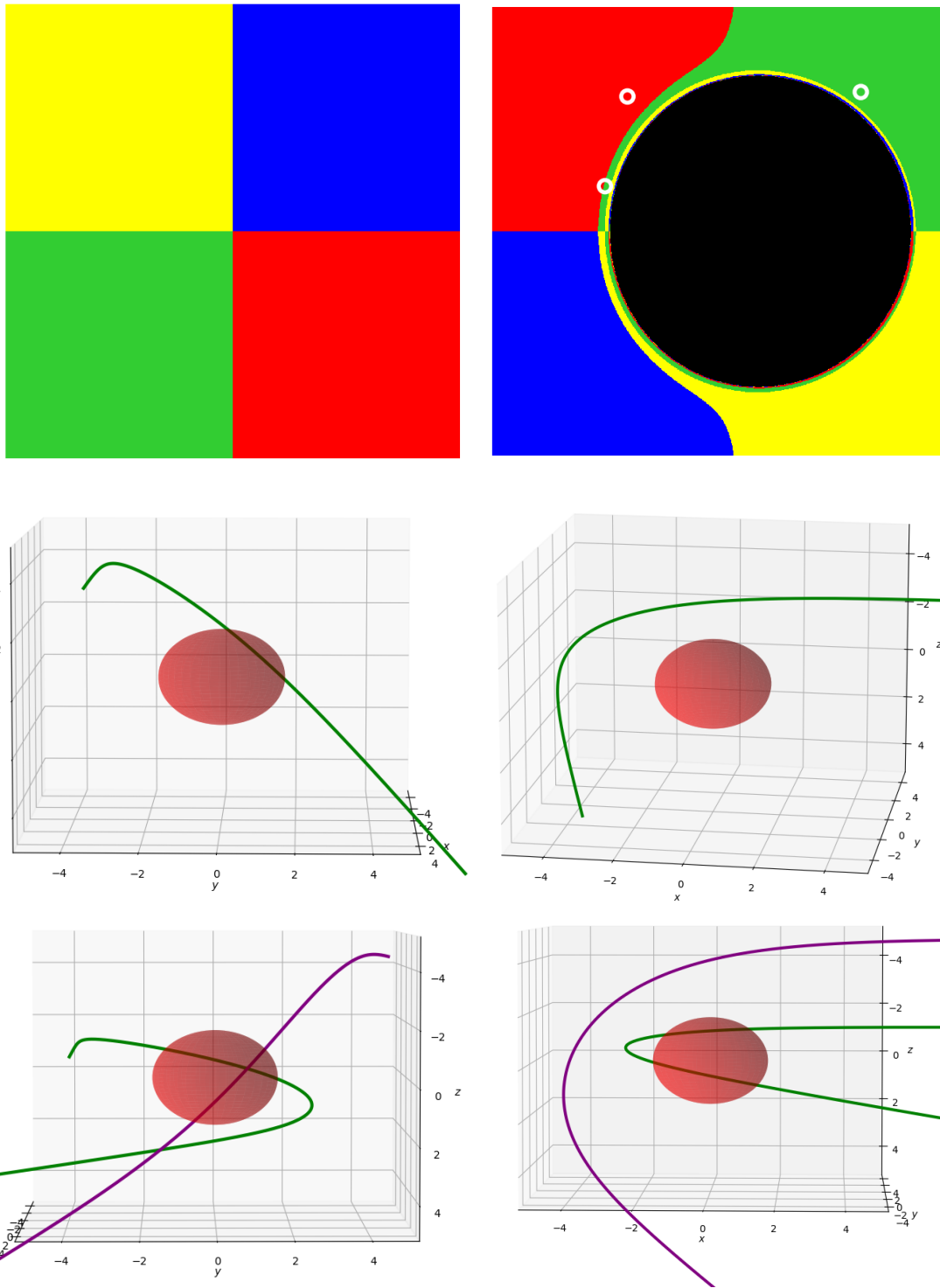


Figure 5.2: The upper plots give examples of ray-traced images. (*left*) Flat space, defining the colour quadrants as we will use them throughout this project. (*right*) Visualization of a Kerr BH with $a/M = 0.7$. Below these four-color images, we plot representative geodesics for the Kerr BH, indicated through the white circles, to show that the geodesics indeed end up in the part of the celestial sphere as defined in the first image. The second row shows a geodesic (green) that corresponds to the circle in the red region. The left plot shows the trajectory from the observer's view, and the right plot gives a view as seen by an observer to the left of the original observer. The bottom row provides similar views of the two geodesics in the green region. The purple geodesic corresponds to the right-most circle, and the green one to the circle closest to the shadow.

In order to numerically integrate the geodesic equations (2.6), they are rewritten as a system of 8 coupled first-order ODE's:

$$\begin{aligned}\frac{dx^\alpha}{d\sigma} &= k^\alpha, \\ \frac{dk^\alpha}{d\sigma} &= -\Gamma_{\mu\nu}^\alpha k^\mu k^\nu.\end{aligned}$$

The code implements 3 different methods to solve these equations. On the one hand, the second- and fourth-order Runge-Kutta integrators are very accurate methods, but computationally expensive as they require many evaluations of the connection coefficients. As an alternative, the Verlet algorithm relies on fewer evaluations of the connection, speeding up the calculations significantly. A detailed description of both can be found in the original papers.

For a given metric, we may have to provide the code with a stopping condition that treats a geodesic as "having fallen into the horizon". For example, in the case of BL coordinates some components of the metric diverge at the event horizon. Numerical codes cannot handle these infinities well, and therefore we have to stop the code before this happens. If we assume that there are no geodesics that can approach the horizon arbitrarily close while escaping afterwards, we can find values for the radial coordinate just outside the horizon that can be considered "an effective horizon".

The stopping condition for the Kerr and Johannsen metric in BL coordinates (as they have the same event horizon) can be formulated as follows:

If a geodesic reaches a point where $r < r_+(1 + \epsilon)$ with ϵ a small number, the integration is stopped.

Most of the time we have taken $\epsilon = 0.05$ and found it to be sufficient. This is due to the fact that the ISCO is usually well outside the event horizon (see Figure 3.2), when the metric is not too close to extremality. However, this is not always the case. An example will be discussed in the next section, using Figure 5.5.

The almost-BPS metric requires a stopping condition as well. The horizon corresponds to $\rho = 0$, and a 'point' is generally not treated well in numerical codes either. The code cannot tell us that a geodesic has reached this point, only that it approached it within a distance that is comparable to the machine precision. Thus, we again need an effective horizon to stop the integration for infalling geodesics. For the almost-BPS black hole, we implement the stopping condition:

If a geodesic reaches a point where $\rho < \epsilon$ with ϵ a small number, the integration is stopped.

We usually adopted the value $\epsilon = 10^{-3}$, which is still relatively large.

In any case, the robustness of the applied stopping criterion can be checked simply by varying the latter. At a fixed resolution, if the shadow edge does not change when decreasing the tolerance ϵ , the stopping criterion is considered appropriate.

The stopping condition need not always correspond to an effective horizon. In the case of horizon-penetrating coordinates (e.g. Kerr-Schild coordinates), the true horizon can be used as a stopping condition since the metric elements do not blow up. Horizon-penetrating coordinates, however, typically render the metric components more complicated and thus more costly to evaluate numerically, slowing down calculations. For our purposes, horizon-penetrating coordinates are not required³, and we use effective horizons.

To implement a new metric in the code, we have to give the covariant and contravariant form. Given the covariant form, it is often useful to rewrite it in the form [4]

$$g_{\mu\nu} = \begin{pmatrix} -\alpha^2 + \beta_k \beta^k & \beta_i \\ \beta_j & \gamma_{ij} \end{pmatrix}.$$

Here, α is the lapse function, β^i is the shift three-vector and γ_{ij} is the spatial part of $g_{\mu\nu}$. From this, we can easily find the inverse metric

$$g^{\mu\nu} = \begin{pmatrix} -1/\alpha^2 & \beta^i/\alpha^2 \\ \beta^j/\alpha^2 & \gamma^{ij} - \beta^i \beta^j / \alpha^2 \end{pmatrix},$$

where γ^{ij} is the algebraic inverse of γ_{ij} and $\beta^i \equiv \gamma^{ij} \beta_j$. This decomposition is useful for implementing the metrics in the **RAPTOR** code.

To speed up the code, we can switch to a logarithmic scale for the radial coordinate with $r \rightarrow s = \log r$. This results in a finer grid close to the horizon, where small integration steps are needed. At large radial distances, the light rays are barely affected by lensing, meaning that a large stepsize is sufficient. In some GRMHD simulations of black hole accretion [20, 28], the polar angle θ is also substituted for a coordinate that concentrates more points in the plane of a possible accretion disk. This is not necessary for our purposes.

The standard output of the code is a list of integers, corresponding to the color on the four-quadrant celestial sphere associated with each geodesic. More output can be produced, such as the total elapsed ϕ -angle and the maximal redshift each geodesic encountered. Conveniently, the code can also save the explicit trajectory of each geodesic, which can then be used to visualize them. We have chosen to use Python for the data processing.

Adding more pixels quickly increases the computation time. In a standard situation where the code is run on 10 OMP threads, four-color simulations of 1000 by 1000 pixels can be completed in a time span on the order of several minutes. This time increases vastly if more output is required (as is the case if we want to extract the photon rings) and if

³For the Johannsen metric, a transformation to Kerr-Schild-like coordinates can be found in [61].

the metric becomes more complicated. In order to accurately determine multiple photon rings in one image, the desired resolution has to be of the order of 16000 by 16000 pixels or more. Since this would require many hours on a regular laptop, we have used the Hortense supercomputer of the Flemish Supercomputer Centre (VSC) to perform these calculations. One computing node on this supercomputer provides 128 cores, which can be used in parallel for **RAPTOR** computations.

5.2 Verification of the analytic shadow

We start by putting **RAPTOR** to use in a verification of the semi-analytic expressions for the BH shadows that we have derived in section 4.1. This is a useful test since the shadow produced by **RAPTOR** is agnostic of concepts like the photon sphere and fixed- r geodesics. We produce the critical curve marking the shadow edge with the help of **Mathematica**, and export this to a Python script, together with the four-color image produced by the **RAPTOR** code. From this four-color image, we extract the shadow (i.e. only plot the points that are assigned the color black) and use the semi-analytical shadow as an overlay.

The results of this verification are presented in Figure 5.3, for a representative BH in the different models. The predictions are clearly very accurate, but the quality really becomes clear when zooming in. Figure 5.4 shows the top part of the black hole, where the different pixels can be distinguished and compared to the critical curve. We have explicitly compared all the analytical and numerical shadows that we have calculated. This shows that the shadows obtained in these two different ways are fully consistent.

We now turn to a peculiar example, which illustrates the importance of choosing and verifying the stopping criterion. Figure 5.5 displays the shadow of the Johannsen BH with non-zero parameters $a/M = 0.7$ and $\alpha_{13} = -4.3$. This value for α_{13} is slightly above the lower bound (2.35). In the left plot of the figure, the shadow as produced by **RAPTOR** with the stopping condition described in the previous section has a relatively large part that is not explained by the semi-analytical shadow. However, this is due to the stopping condition: decreasing ϵ results in a shadow that better resembles the red curve. The fact that this stopping condition is so important for this particular metric is because geodesics aimed at this specific region reach the small zone between the event horizon r_+ and the "effective horizon" $r_+(1 + \epsilon)$, if ϵ is not sufficiently small. This causes the code to treat this geodesic as 'infalling' while it really is able to escape in the end. An example of such a "grazing geodesic" can be seen in Figure 5.6. This figure also gives the four-color visualisation of this particular spacetime, which shows more interesting lensing effects to the left of the shadow. In conclusion, we managed to detect the numerical error based on the semi-analytical results. Given that the semi-analytical critical curve excludes this shearing geodesic from the horizon, we are confident that the latter is not a numerical artifact of integration close to the horizon.

Overall, we conclude that the shadows as produced by **RAPTOR** are consistent with the semi-analytical prescriptions. The discrepancies between the two are smaller than the pixel size, except possibly in points where **Mathematica** relies heavily on interpolation.

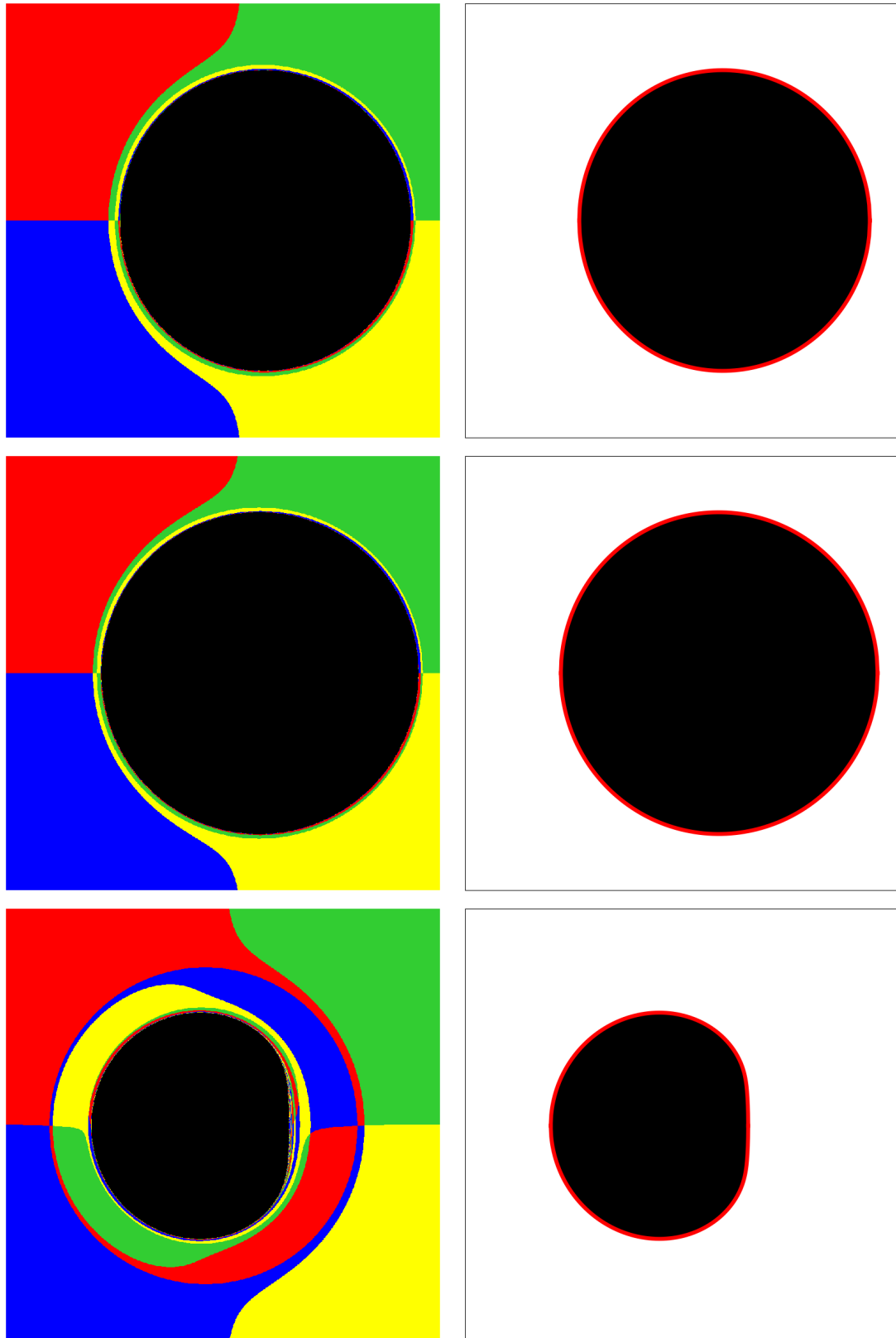


Figure 5.3: The left column shows four-color visualization of three different BHs. The right column shows the extracted shadow, along with a red overlay of the critical curve as calculated in section 4.1. (top) Kerr with $a/M = 0.7$ (middle) Johannsen with $a/M = 0.7, \alpha_{13} = 2$ (bottom) almost-BPS with $\mathbf{Q} = (2, 2, 2, 2) \cdot \zeta, h = 0.3, \alpha = 3.99\zeta$. The bottom image shows a region of space of size $3M$ by $3M$, whereas the other two are $15M$ by $15M$. The resolution is 1000 pixels in each direction.

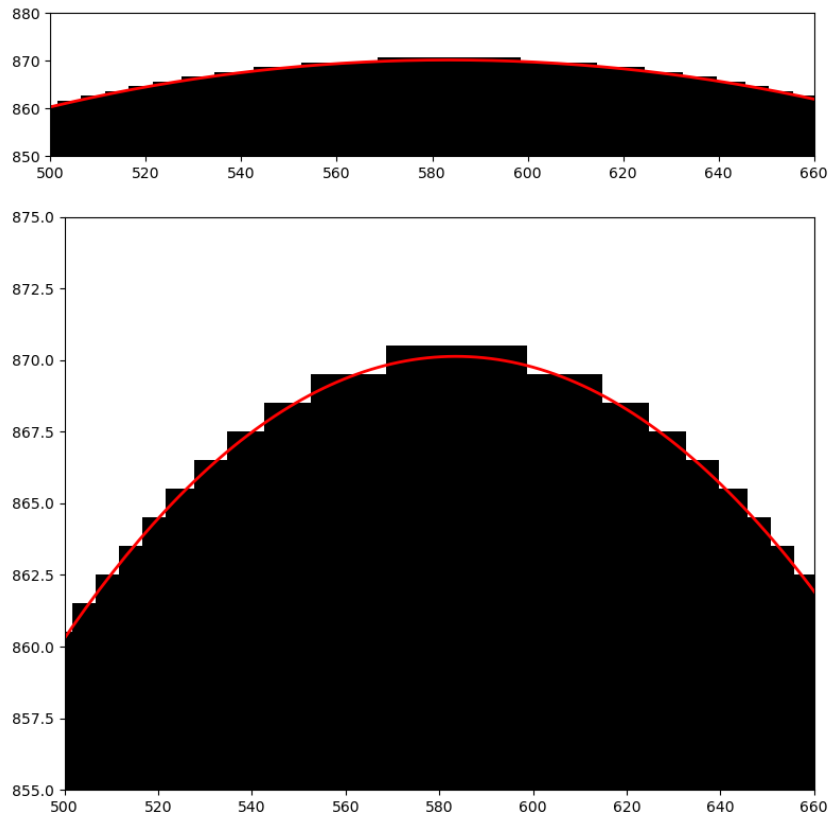


Figure 5.4: Zoom-in of the Johannsen black hole depicted in Figure 5.3. The top of the shadow is seen (*upper*) in a plot where the axes have the same scale (*bottom*) and in a plot where the vertical axis has been stretched out, to facilitate a view of the pixel structure of the shadow as obtained by the RAPTOR computation. The red line is the semi-analytical critical curve, which can be seen to match the numerical shadow very well, to the pixel level. The labels on the axes correspond to the pixel numbers.

This is generally closer to the equator, where the semi-analytical shadow is sampled less accurately due to the non-linear dependence of the angular coordinate ϕ_R on the radial coordinate, used to parametrize the shadow. Also, we have shown with an explicit example that the shadow as determined by RAPTOR can show numerical discrepancies if there are escaping geodesics that approach the horizon to a small distance below the stopping condition. It is therefore important to vary the stopping condition, to verify the convergence of the resulting shadow.

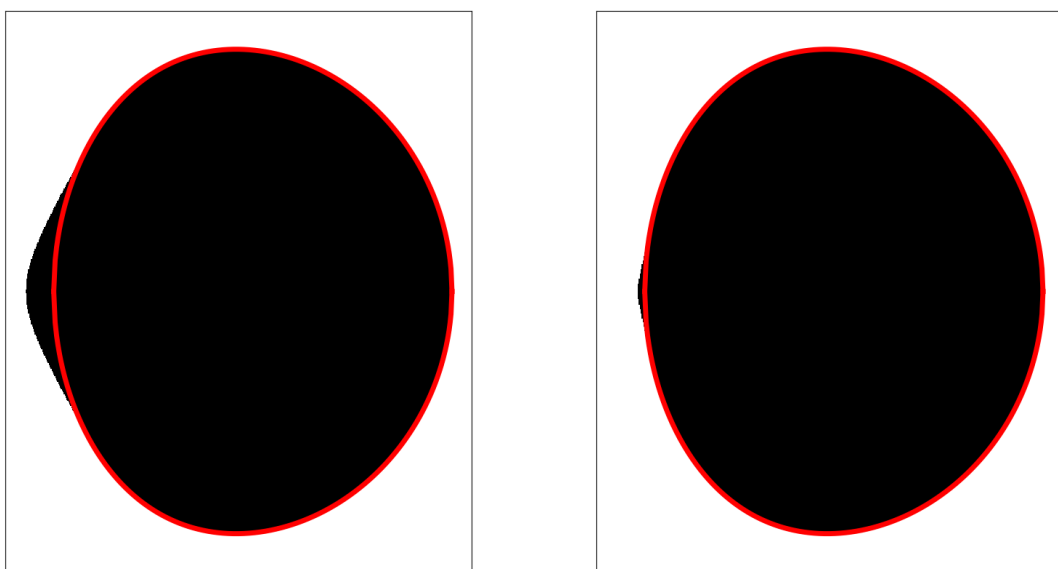


Figure 5.5: Shadow overlays for the Johannsen spacetime with non-zero parameters $a/M = 0.7$, $\alpha_{13} = -4.3$. (*left*) The RAPTOR shadow when $\epsilon = 0.05$ and (*right*) the RAPTOR shadow when $\epsilon = 0.01$. The ray-traced shadow matches the overlay better when the stopping criterion implements a smaller value for ϵ . The numerical error is due to "grazing geodesics", of which an example can be seen in Figure 5.6.

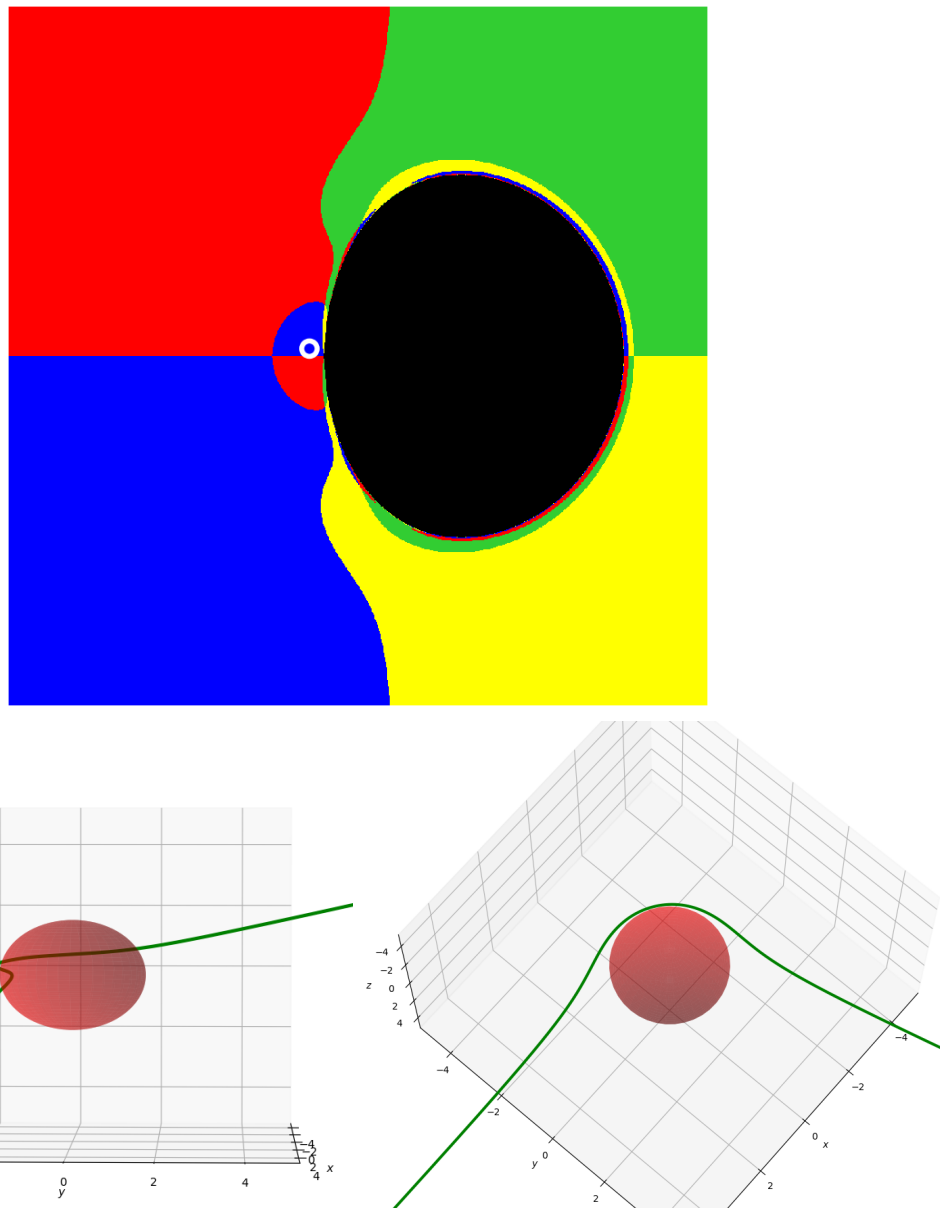


Figure 5.6: (*top*) The Johannsen spacetime with non-zero parameters $a/M = 0.7$, $\alpha_{13} = -4.3$. The white circle indicates the impact parameters of a grazing geodesic, that is plotted in the bottom half of the figure. (*left*) The grazing geodesic viewed under an angle that is approximately that of the observer. The red surface is the event horizon. (*right*) The grazing geodesic as seen from a top view, compared to the plot on the left. This shows how closely the geodesic approaches the event horizon, while still managing to escape off to infinity.

5.3 Estimates of the Lyapunov exponent

In the previous section we have verified that our semi-analytical predictions for the BH shadow are consistent with the numerical results from **RAPTOR** simulations. Given the tight connection between the formulas for the shadow and the Lyapunov exponent (see section 4.3), we want to investigate if we can extract the latter from the ray-traced images as well. If this is possible, this would imply that the Lyapunov exponent could be determined for more complicated spacetimes as well, for which a (semi-)analytical approach is no longer feasible. In this section we explain how we approached this question, and show our estimates for some of the metrics. We compare them to the results of section 4.3.

We recall that the Lyapunov exponent is related to the relative width of subsequent photon rings through equation (4.18). Therefore, the idea is to extract the outermost photon rings from the ray-traced images, and compare their relative widths.

However, we immediately face a problem. The semi-analytical approach to the Lyapunov exponent was based on the definition of 'orbit' as presented in section 4.2.1. But, the **RAPTOR** code does not have an implemented diagnostic that can track the number of oscillations in the θ -direction⁴. Therefore, we are forced into an approach based on orbits as defined in section 4.2.2. The rings with respect to this classification can be extracted from the **RAPTOR** calculations, as the final elapsed ϕ -angle is saved after the computation. We emphasize that, *a priori*, we can not expect the Lyapunov exponent based on these two distinct approaches to be the same. This is primarily due to the fact that we can find explicit geodesics that complete a number of orbits that differs with respect to both criteria.

In order to extract multiple rings from an image, a high resolution is needed. The calculations performed on the supercomputer have a resolution of $2^{14} = 16384$ pixels in both dimensions, for a total of over 250 million geodesics. For each set of parameters, we created 3 images. The first image encompasses the entire BH shadow and its surroundings, whereas the second one zooms in on the critical curve to 1-5% of the initial image width and the third one decreases this to 0.01-0.05%. The exact percentage depends on some trial-and-error at low resolution, depending on where the rings are exactly positioned. The advantage of the second and third image is that they can resolve high- n rings. From each of these images, the rings are extracted and their widths in pixels are stored. The relative widths are then converted to an estimate for the Lyapunov exponent as

$$\gamma_n = \ln \frac{w_n}{w_{n+1}}. \quad (5.1)$$

For the moment, we have only applied this method to images as seen by an equatorial observer. Furthermore, we have mainly focused on estimating the Lyapunov exponent at an on-screen angle of π , i.e the left side. The advantage here is that, since the shadow is equatorially symmetric, we can extract the widths by approaching the shadow horizontally. This allows us to extract the 8192th row of pixels from the image. The width of a ring is now determined by counting the number of pixels in this row that correspond to

⁴It could be implemented in principle, but this goes beyond the scope of this work. We come back to this in Chapter 6.

this ring. This method also works for an on-screen angle equal to zero. However, to make estimates of the Lyapunov exponent in between these angles, we would have to approach the shadow along a straight line with a non-zero slope, which is harder as we only have discrete pixels. We defer this to future work (see Chapter 6).

Figure 5.7 shows the different aspects of the process, for one of the three images within one simulation (Johannsen metric, $a/M = 0.7$ and $\alpha_{13} = 2$). The first plot is the regular four-color screen, which is not explicitly used but is useful for comparison. The second plot depicts the number of azimuthal half-orbits for each geodesic, according to the definition of section 4.2.2. Different rings can clearly be distinguished. The third plot represents the width of each ring according to its order, in the color of the second plot. This figure shows explicitly how the rings decrease in width as the order increases. This is the third image for this specific simulation, and combined with the other two images it is remarkable that we are able to resolve up to approximately the $n \sim 9$ photon ring, which is in this case $\sim 10^{-8}$ times the width of the first photon ring.

The estimates based on the three images are then combined. The result for the same example can be seen in Figure 5.8. First of all, this shows how the three images probe different rings. To make an estimate γ_n for the Lyapunov exponent, both the n -th ring and the $(n+1)$ -th ring have to be completely visible within the image. Furthermore, the highest order estimate within one image appears to differ from the others. This is due to the fact that, within one image, the highest order ring is sometimes only one or two pixels wide, such that the width has a large relative error. Therefore, we decide not to focus too much on estimates that are obtained from the smallest ring in an image. In the example given here, the most reliable estimates are concentrated within an interval [2.1, 2.2]. In order to make a point estimate, we take the mean of all the estimates as this is robust against the outliers. Comparing this to the semi-analytic prediction in Figure 4.15, computed for θ -orbits, we see that our estimates are well below the theoretical value of 2.92. We conclude that this example does not reproduce the theoretical value very well.

The quality of the estimates varies for the different simulations. Table 5.1 gives a summary for the different simulations. The first conclusion we draw from this table is that the estimates seem to be better for BHs with relatively small angular momentum. Increasing the values of the spin creates strong differences between the numerical and theoretical predictions. If we look at the two simulations of the Johannsen metric with $\alpha_{13} = 2$, we see that both the numerical and theoretical prediction decrease. This means that both predictions provide the same qualitative trend, even though they are not quantitatively the same. However, this is not the case when we hold either α_{22} or α_{52} fixed. The numerical prediction decreases for the larger spin, whereas the theoretical prediction shows an increase. The two simulations of the almost-BPS metric do not agree with the theoretical value either. The difference between the two simulations is the value of the parameter h , and we see that the correct qualitative trend is reproduced: the Lyapunov exponent decreases when h decreases (as can be seen in Figure 4.16 as well). The estimate plots for all these simulations can be found in Appendix B.

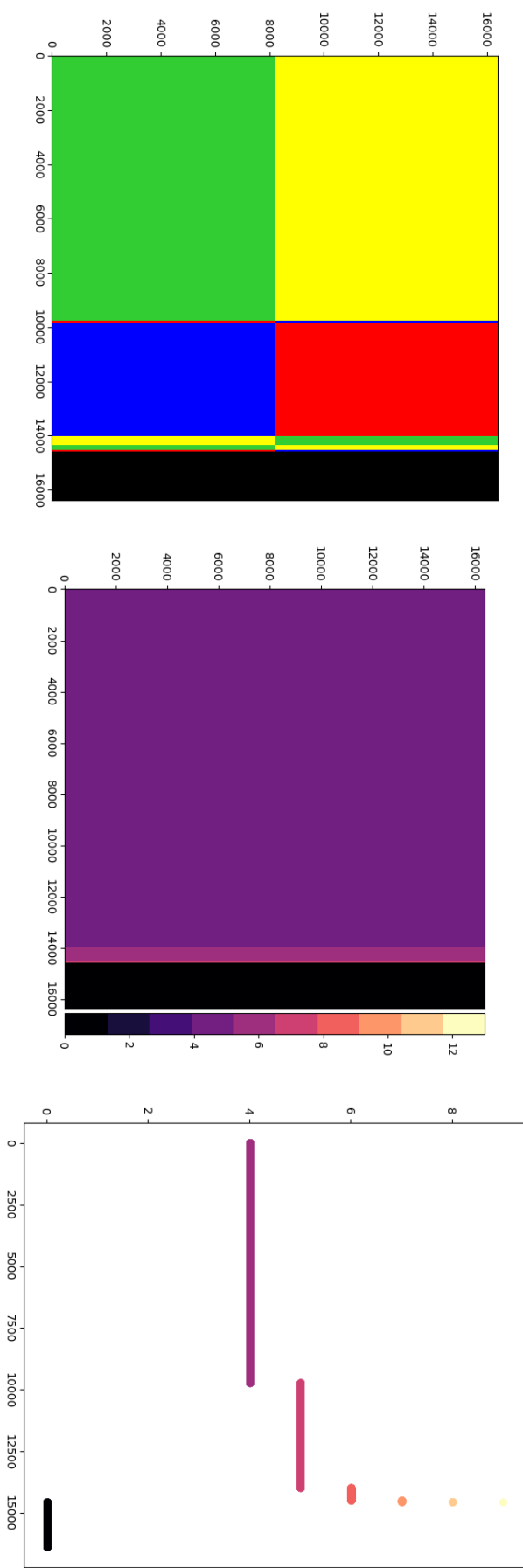


Figure 5.7: This figure shows the analysis of the third image, obtained for the Johanssen metric with $a/M = 0.7$ and $\alpha_{13} = 2$. (*left*) The four-color screen, showing a region of $0.0015M$ in each direction. This is the region The numbers on the axes represent the pixels. (*middle*) The same region as in the left plot, but now the geodesics are colored according to the number of half-orbits they elapsed. The different rings are clearly visible. (*right*) A visualization of the relative widths of the different rings at an on-screen angle $\phi_R = \pi$, in the color of the middle plot. The vertical axis denotes the order n of the ring. The black part at the right corresponds to the shadow.

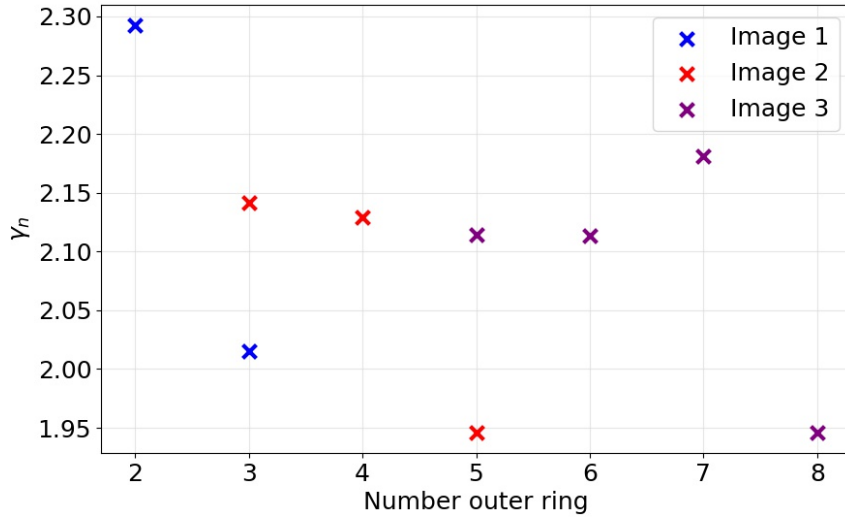


Figure 5.8: Estimates for the Lyapunov exponent at an on-screen angle $\phi_R = \pi$ for the Johannsen metric with parameters $a/M = 0.7$ and $\alpha_{13} = 2$. The different images probe different orders of the rings.

| Metric | Parameters | Median | Theoretical prediction |
|------------|--|--------|------------------------|
| Kerr | $a = 0.1M$ | 3.02 | π |
| Kerr | $a = 0.7M$ | 1.95 | π |
| Kerr | $a = 0.99M$ | 0.53 | π |
| Johannsen | $a = 0, \alpha_{13} = 2$ | 3.16 | 3.16 |
| Johannsen | $a = 0, \alpha_{22} = 2$ | 3.14 | 3.14 |
| Johannsen | $a = 0, \alpha_{52} = 3$ | 3.67 | 3.63 |
| Johannsen | $a = 0.7M, \alpha_{13} = 2$ | 2.11 | 2.92 |
| Johannsen | $a = 0.7M, \alpha_{22} = 2$ | 1.86 | 5.44 |
| Johannsen | $a = 0.7M, \alpha_{52} = 3$ | 2.58 | 4.14 |
| almost-BPS | $\mathbf{Q} = (2, 1, 1, 1) \cdot \zeta, h = 1, \alpha = \zeta$ | 2.49 | 2.18 |
| almost-BPS | $\mathbf{Q} = (2, 1, 1, 1) \cdot \zeta, h = 0.3, \alpha = \zeta$ | 2.03 | 1.85 |

Table 5.1: Summary of the numerical estimates for the Lyapunov exponent at an on-screen angle $\phi_R = \pi$, based on the azimuthal orbits. Different simulations are presented and compared to the theoretical predictions based on the θ -orbit. For the numerical prediction, the median of all estimates is taken. The theoretical prediction is based on Mathematica 12.

Overall, the method we presented based on azimuthal orbits is not yet optimized to predict reliable values for the Lyapunov exponent of θ -orbits. The predictions are relatively accurate for BHs with small angular momentum. This can be understood for the Kerr and Johannsen metric by realizing that these BHs are spherically symmetric if the angular momentum is zero: therefore, the number of orbits in the polar and azimuthal direction will agree for most geodesics, since the nearly-bound orbits will approach great circles. We have not yet checked this explicitly for the almost-BPS metric. The predictions for BHs with large angular momentum are not accurate yet, but we will address possible future improvements to our method in Chapter 6.

Chapter 6

Conclusion and Outlook

In order to resolve the black hole information paradox, gravity is being tested in the strong-field regime. The publications of the EHT have enabled physicists to investigate images of black holes on the horizon scale. In this thesis we have investigated two black hole spacetimes beyond GR, the Johannsen and almost-BPS metrics, and investigated how they can be distinguished from the Kerr metric on the basis of such images.

We have presented semi-analytical expressions for the black hole shadow of both metrics, and explicitly verified their correctness using the ray-tracing code **RAPTOR**. Even though the black hole shadow may not be the most promising observable due its large degree of degeneracy, it is a stepping stone towards determining the Lyapunov exponent associated with the photon rings. This sequence of self-similar rings depends universally on the underlying spacetime, and accurately measuring the first few rings is feasible within the near future.

We have also provided semi-analytic expressions for this Lyapunov exponent in both spacetimes, and made an attempt to obtain these results from the ray-tracing code as well. Our method is promising, but requires further tuning. To improve it, we would first like to implement a diagnostic in the code to correctly determine the photon rings with respect to the number of polar half-orbits. Furthermore, we would like to extend our analysis to extract the Lyapunov exponent off-equatorially in the numerical approach. In a first instance, this can be done using the approximation 4.26, but ideally the aim is to find an accurate numerical procedure.

Another interesting continuation of this research would be to formulate concrete predictions for future precise tests of GR, in the spirit of [53, 54, 64]. Given that we have managed to extend some of the necessary calculations to two non-Kerr metrics, it is feasible that we can make the predictions of these metrics explicit as well.

With respect to the EHT results that are already available for M87* and Sgr A*, it could be interesting to use the data to constrain the parameters of the almost-BPS metric. This would require additional work with the ray-tracing code, now also including an accretion

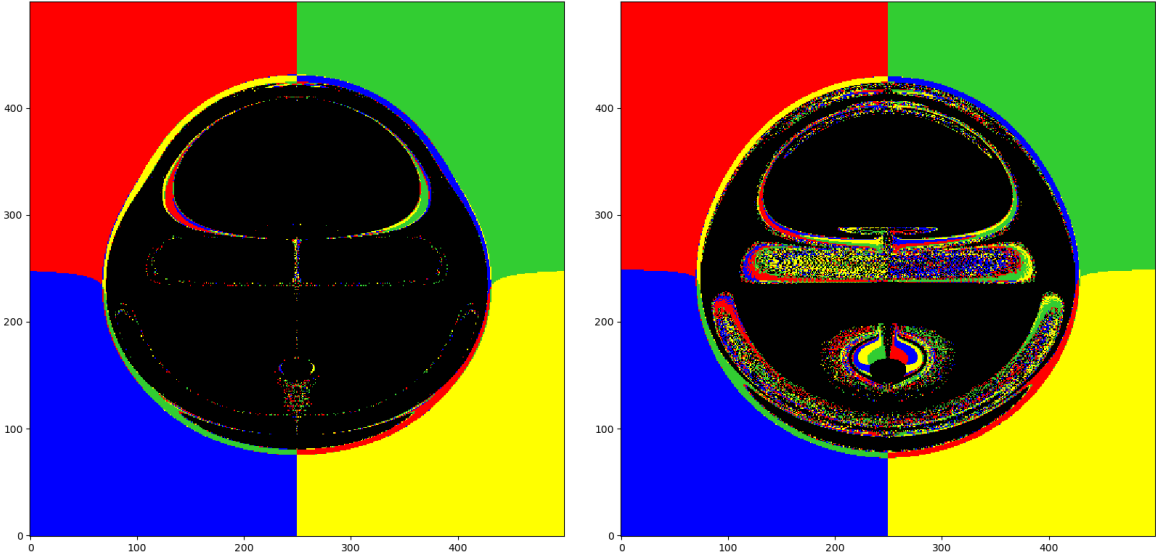


Figure 6.1: Ray-traced images of "bumpy" black holes, whose shadow does not possess equatorial symmetry. (*left*) The Manko-Novikov metric with parameters $\alpha = 0$ and $\alpha_3 = 1.3$, see Appendix C.2. (*right*) The linearized bumpy black hole with parameters $a = 0$ and $B_3 = 0.8$, see Appendix C.1.

disk. The physicists in the EHT have already done this for the Johannsen metric, and the results can be found in [33].

Another interesting prospect is to investigate the microstate geometries associated with the almost-BPS black hole, and see what effect they produce on ray-traced images. A similar problem is addressed in [3], for microstates associated to a supersymmetric, non-rotating BH. It was shown that some microstates can mimick a BH very well by trapping light for a long time. Given that it is more likely that astrophysical black holes are rotating and not supersymmetric, it would be interesting to see if similar results can be obtained for the almost-BPS microstate geometries.

We have already remarked on the fact that the almost-BPS spacetime is not symmetric with respect to the $\theta = \frac{\pi}{2}$ plane, whereas the shadow is. This is explicitly seen in the bottom row of Figure 5.3. In order to break the equatorial symmetry of the shadow, the metric itself cannot posses equatorial symmetry. Furthermore, the metric has to be non-integrable [37]. Therefore, we have briefly investigated two metrics (see Appendix C) that satisfy these conditions, and the result can be seen in Figure 6.1. These are the first ever ray-traced images of black holes with a shadow that is not symmetric with respect to the equatorial plane. A more detailed analysis is required, as peculiar features are clearly present within the shadow boundary. To establish whether they are physical lensing effects due to the non-integrability of the geodesic equations, or artifacts coming from numerical errors or non-physical singularities of these metrics, an investigation of the effective potential that geodesics feel could provide a possible starting point.

Bibliography

- [1] R Abuter, N Aimar, A Amorim, J Ball, M Bauböck, JP Berger, H Bonnet, G Bourdarot, W Brandner, V Cardoso, et al. Mass distribution in the Galactic Center based on interferometric astrometry of multiple stellar orbits. *Astronomy & Astrophysics*, 657:L12, 2022.
- [2] Farruh Atamurotov, Ahmadjon Abdujabbarov, and Bobomurat Ahmedov. Shadow of rotating non-Kerr black hole. *Physical Review D*, 88(6):064004, 2013.
- [3] Fabio Bacchini, Daniel R Mayerson, Bart Ripperda, Jordy Davelaar, Héctor Olivares, Thomas Hertog, and Bert Vercnocke. Fuzzball shadows: Emergent horizons from microstructure. *Physical review letters*, 127(17):171601, 2021.
- [4] Fabio Bacchini, Bart Ripperda, Alexander Yuran Chen, and Lorenzo Sironi. Generalized, energy-conserving numerical simulations of particles in general relativity. I. Time-like and null geodesics. *The Astrophysical Journal Supplement Series*, 237(1):6, 2018.
- [5] Ibrahima Bah, Iosif Bena, Pierre Heidmann, Yixuan Li, and Daniel R Mayerson. Gravitational footprints of black holes and their microstate geometries. *Journal of High Energy Physics*, 2021(10):1–49, 2021.
- [6] James M Bardeen. Timelike and null geodesics in the Kerr metric. *Black holes*, 215, 1973.
- [7] James M Bardeen, William H Press, and Saul A Teukolsky. Rotating black holes: locally nonrotating frames, energy extraction, and scalar synchrotron radiation. *The Astrophysical Journal*, 178:347–370, 1972.
- [8] Jacob D Bekenstein. Black holes and entropy. In *JACOB BEKENSTEIN: The Conservative Revolutionary*, pages 307–320. World Scientific, 2020.
- [9] Jacob D Bekenstein. Generalized second law of thermodynamics in black-hole physics. In *JACOB BEKENSTEIN: The Conservative Revolutionary*, pages 321–329. World Scientific, 2020.
- [10] Iosif Bena, Giang Guido Dall’Agata, Stefano Giusto, Clement Ruef, and Nicholas P Warner. Non-BPS black rings and black holes in Taub-NUT. *Journal of High Energy Physics*, 2009(06):015, 2009.
- [11] Andy Bohn, William Throwe, François Hébert, Katherine Henriksson, Darius Bunandar, Mark A Scheel, and Nicholas W Taylor. What does a binary black hole merger look like? *Classical and Quantum Gravity*, 32(6):065002, 2015.

- [12] Charles Thomas Bolton. Identification of Cygnus X-1 with HDE 226868. *Nature*, 235(5336):271–273, 1972.
- [13] Raphael Bousso. The holographic principle. *Reviews of Modern Physics*, 74(3):825, 2002.
- [14] Thomas Bronzwaer, Jordy Davelaar, Ziri Younsi, Monika Mościbrodzka, Heino Falcke, Michael Kramer, and Luciano Rezzolla. RAPTOR-I. Time-dependent radiative transfer in arbitrary spacetimes. *Astronomy & Astrophysics*, 613:A2, 2018.
- [15] Thomas Bronzwaer, Ziri Younsi, Jordy Davelaar, and Heino Falcke. RAPTOR-II. Polarized radiative transfer in curved spacetime. *Astronomy & Astrophysics*, 641:A126, 2020.
- [16] Vitor Cardoso, Alex S. Miranda, Emanuele Berti, Helvi Witek, and Vilson T. Zanchin. Geodesic stability, Lyapunov exponents, and quasinormal modes. *Physical Review D*, 79(6), mar 2009.
- [17] Vitor Cardoso and Paolo Pani. Testing the nature of dark compact objects: a status report. *Living Reviews in Relativity*, 22(1):1–104, 2019.
- [18] Sean M Carroll. *Spacetime and geometry*. Cambridge University Press, 2019.
- [19] Brandon Carter. Global structure of the Kerr family of gravitational fields. *Physical Review*, 174(5):1559, 1968.
- [20] The Event Horizon Telescope Collaboration. First M87 Event Horizon Telescope Results. I. The Shadow of the Supermassive Black Hole. *The Astrophysical Journal Letters*, 875(1):L1, April 2019.
- [21] The Event Horizon Telescope Collaboration. First M87 Event Horizon Telescope Results. II. Array and Instrumentation. *The Astrophysical Journal Letters*, 875(1):L2, April 2019.
- [22] The Event Horizon Telescope Collaboration. First M87 Event Horizon Telescope Results. III. data processing and calibration. *ApJL*, 875:3, 2019.
- [23] The Event Horizon Telescope Collaboration. First M87 Event Horizon Telescope Results. IV. Imaging the Central Supermassive Black Hole. *The Astrophysical Journal Letters*, 875(1):L4, April 2019.
- [24] The Event Horizon Telescope Collaboration. First M87 Event Horizon Telescope Results. V. Physical Origin of the Asymmetric Ring. *The Astrophysical Journal Letters*, 875(1):L5, April 2019.
- [25] The Event Horizon Telescope Collaboration. First M87 Event Horizon Telescope Results. VI. The Shadow and Mass of the Central Black Hole. *The Astrophysical Journal Letters*, 875(1):L6, April 2019.
- [26] The Event Horizon Telescope Collaboration. First M87 Event Horizon Telescope Results. VII. polarization of the ring. *ApJL*, 910(L12):48, 2021.
- [27] The Event Horizon Telescope Collaboration. First M87 Event Horizon Telescope

- Results. VIII. magnetic field structure near the event horizon. *ApJL*, 910(L13):43, 2021.
- [28] The Event Horizon Telescope Collaboration. First Sagittarius A* Event Horizon Telescope Results. I. the shadow of the supermassive black hole in the center of the Milky Way. *The Astrophysical Journal Letters*, 930(L12), 2022.
- [29] The Event Horizon Telescope Collaboration. First Sagittarius A* Event Horizon Telescope Results. II. EHT and multiwavelength observations, data processing, and calibration. *The Astrophysical Journal Letters*, 930(L13), 2022.
- [30] The Event Horizon Telescope Collaboration. First Sagittarius A* Event Horizon Telescope Results. III. imaging of the Galactic Center supermassive black hole. *The Astrophysical Journal Letters*, 930(L14), 2022.
- [31] The Event Horizon Telescope Collaboration. First Sagittarius A* Event Horizon Telescope Results. IV. variability, morphology, and black hole mass. *The Astrophysical Journal Letters*, 930(L15), 2022.
- [32] The Event Horizon Telescope Collaboration. First Sagittarius A* Event Horizon Telescope Results. V. testing astrophysical models of the Galactic Center black hole. *The Astrophysical Journal Letters*, 930(L16), 2022.
- [33] The Event Horizon Telescope Collaboration. First Sagittarius A* Event Horizon Telescope Results. VI. testing the black hole metric. *The Astrophysical Journal Letters*, 930(L17), 2022.
- [34] Nathan A Collins and Scott A Hughes. Towards a formalism for mapping the space-times of massive compact objects: Bumpy black holes and their orbits. *Physical Review D*, 69(12):124022, 2004.
- [35] Gastón Creci, Stefan Vandoren, and Helvi Witek. Evolution of black hole shadows from superradiance. *Physical Review D*, 101(12):124051, 2020.
- [36] Pedro VP Cunha and Carlos AR Herdeiro. Shadows and strong gravitational lensing: a brief review. *General Relativity and Gravitation*, 50(4):1–27, 2018.
- [37] Pedro VP Cunha, Carlos AR Herdeiro, and Eugen Radu. Isolated black holes without Z2 isometry. *Physical Review D*, 98(10):104060, 2018.
- [38] A De Vries. The apparent shape of a rotating charged black hole, closed photon orbits and the bifurcation set A4. *Classical and Quantum Gravity*, 17(1):123, 2000.
- [39] Frank Watson Dyson, Arthur Stanley Eddington, and Charles Davidson. IX. a determination of the deflection of light by the Sun’s gravitational field, from observations made at the total eclipse of May 29, 1919. *Philosophical Transactions of the Royal Society of London. Series A, Containing Papers of a Mathematical or Physical Character*, 220(571-581):291–333, 1920.
- [40] A. Eckart and R. Genzel. Stellar proper motions in the central 0.1 pc of the Galaxy. *Monthly Notices of the Royal Astronomical Society*, 284(3):576–598, January 1997.
- [41] Albert Einstein. Die Feldgleichungen der Gravitation. *Sitzungsberichte der Königlich Preußischen Akademie der Wissenschaften (Berlin)*, pages 844–847, January 1915.

- [42] Daniel Z Freedman and Antoine Van Proeyen. *Supergravity*. Cambridge university press, 2012.
- [43] Jonathan R Gair, Chao Li, and Ilya Mandel. Observable properties of orbits in exact bumpy spacetimes. *Physical Review D*, 77(2):024035, 2008.
- [44] Anton Galajinsky and Kirill Orekhov. N= 2 superparticle near horizon of extreme Kerr-Newman-AdS-dS black hole. *Nuclear Physics B*, 850(2):339–348, 2011.
- [45] Karl Gebhardt, Joshua Adams, Douglas Richstone, Tod R Lauer, SM Faber, Kayhan Gultekin, Jeremy Murphy, and Scott Tremaine. The black hole mass in M87 from Gemini/NIFS adaptive optics observations. *The Astrophysical Journal*, 729(2):119, 2011.
- [46] A. M. Ghez, B. L. Klein, M. Morris, and E. E. Becklin. High Proper-Motion Stars in the Vicinity of Sagittarius A*: Evidence for a Supermassive Black Hole at the Center of Our Galaxy. *The Astrophysical Journal*, 509(2):678–686, December 1998.
- [47] Kevin Goldstein and Stefanos Katmadas. Almost-BPS black holes. *Journal of High Energy Physics*, 2009(05):058–058, may 2009.
- [48] Samuel E Gralla. Can the EHT M87 results be used to test general relativity? *Physical Review D*, 103(2):024023, 2021.
- [49] Samuel E Gralla, Daniel E Holz, and Robert M Wald. Black hole shadows, photon rings, and lensing rings. *Physical Review D*, 100(2):024018, 2019.
- [50] Samuel E Gralla and Alexandru Lupsasca. Lensing by Kerr black holes. *Physical Review D*, 101(4):044031, 2020.
- [51] Samuel E Gralla and Alexandru Lupsasca. Null geodesics of the Kerr exterior. *Physical Review D*, 101(4):044032, 2020.
- [52] Samuel E Gralla and Alexandru Lupsasca. Observable shape of black hole photon rings. *Physical Review D*, 102(12):124003, 2020.
- [53] Samuel E Gralla, Alexandru Lupsasca, and Daniel P Marrone. The shape of the black hole photon ring: A precise test of strong-field general relativity. *Physical Review D*, 102(12):124004, 2020.
- [54] Shahar Hadar, Michael D Johnson, Alexandru Lupsasca, and George N Wong. Photon ring autocorrelations. *Physical Review D*, 103(10):104038, 2021.
- [55] Daniel Harlow. Jerusalem lectures on black holes and quantum information. *Reviews of Modern Physics*, 88(1):015002, 2016.
- [56] James B Hartle. Gravity: an introduction to Einstein’s general relativity, 2003.
- [57] Stephen W Hawking. Particle creation by black holes. In *Euclidean quantum gravity*, pages 167–188. World Scientific, 1975.
- [58] Stephen W Hawking. Breakdown of predictability in gravitational collapse. *Physical Review D*, 14(10):2460, 1976.

- [59] Gerard 'T Hooft. Dimensional reduction in quantum gravity. *arXiv preprint gr-qc/9310026*, 1993.
- [60] Tim Johannsen. Photon rings around Kerr and Kerr-like black holes. *The Astrophysical Journal*, 777(2):170, 2013.
- [61] Tim Johannsen. Regular black hole metric with three constants of motion. *Physical Review D*, 88(4):044002, 2013.
- [62] Tim Johannsen. Systematic study of event horizons and pathologies of parametrically deformed Kerr spacetimes. *Physical Review D*, 87(12):124017, 2013.
- [63] Tim Johannsen and Dimitrios Psaltis. Metric for rapidly spinning black holes suitable for strong-field tests of the no-hair theorem. *Physical Review D*, 83(12):124015, 2011.
- [64] Michael D Johnson, Alexandru Lupsasca, Andrew Strominger, George N Wong, Shachar Hadar, Daniel Kapec, Ramesh Narayan, Andrew Chael, Charles F Gammie, Peter Galison, et al. Universal interferometric signatures of a black hole's photon ring. *Science advances*, 6(12):eaaz1310, 2020.
- [65] Haroldo CD Lima Junior, Luís CB Crispino, Pedro VP Cunha, and Carlos AR Herdeiro. Can different black holes cast the same shadow? *Physical Review D*, 103(8):084040, 2021.
- [66] Daniel Kapec and Alexandru Lupsasca. Particle motion near high-spin black holes. *Classical and Quantum Gravity*, 37(1):015006, 2019.
- [67] Roy P. Kerr. Gravitational Field of a Spinning Mass as an Example of Algebraically Special Metrics. *Physical Review Letter*, 11(5):237–238, September 1963.
- [68] Finn Larsen and Cynthia Keeler. Separability of black holes in string theory. *arXiv preprint arXiv:1207.5928*, 2012.
- [69] LIGO Scientific Collaboration and Virgo Collaboration. Observation of Gravitational Waves from a Binary Black Hole Merger. *Physical Review Letters*, 116(6):061102, February 2016.
- [70] J. P. Luminet. Image of a spherical black hole with thin accretion disk. *Astronomy and Astrophysics*, 75:228–235, May 1979.
- [71] VS Manko and ID Novikov. Generalizations of the Kerr and Kerr-Newman metrics possessing an arbitrary set of mass-multipole moments. *Classical and Quantum Gravity*, 9(11):2477, 1992.
- [72] Samir D Mathur. The information paradox: a pedagogical introduction. *Classical and Quantum Gravity*, 26(22):224001, 2009.
- [73] S.D. Mathur. The fuzzball proposal for black holes: an elementary review. *Fortschritte der Physik*, 53(7-8):793–827, 2005.
- [74] Robert V Pound and Glen A Rebka Jr. Apparent weight of photons. *Physical Review Letters*, 4(7):337, 1960.
- [75] M. J. Reid, K. M. Menten, A. Brunthaler, X. W. Zheng, T. M. Dame, Y. Xu, J. Li, N. Sakai, Y. Wu, K. Immer, B. Zhang, A. Sanna, L. Moscadelli, K. L. J. Rygl,

- A. Bartkiewicz, B. Hu, L. H. Quiroga-Nuñez, and H. J. van Langevelde. Trigonometric Parallaxes of High-mass Star-forming Regions: Our View of the Milky Way. *The Astrophysical Journal*, 885(2):131, November 2019.
- [76] Rittick Roy, Askar B Abdikamalov, Dmitry Ayzenberg, Cosimo Bambi, Shafqat Riaz, and Ashutosh Tripathi. Testing the weak-equivalence principle near black holes. *Physical Review D*, 104(4):044001, 2021.
- [77] K. Schwarzschild. On the Gravitational Field of a Mass Point According to Einstein’s Theory. *Abh. Konigl. Preuss. Akad. Wissenschaften Jahre 1906, 92, Berlin, 1907*, 1916:189–196, January 1916.
- [78] Rajibul Shaikh. Black hole shadow in a general rotating spacetime obtained through Newman-Janis algorithm. *Physical Review D*, 100(2):024028, 2019.
- [79] Andrew Strominger and Cumrun Vafa. Microscopic origin of the Bekenstein-Hawking entropy. *Physics Letters B*, 379(1-4):99–104, 1996.
- [80] Leonard Susskind. The world as a hologram. *Journal of Mathematical Physics*, 36(11):6377–6396, 1995.
- [81] Edward Teo. Spherical photon orbits around a Kerr black hole. *General Relativity and Gravitation*, 35(11):1909–1926, 2003.
- [82] A Richard Thompson, James M Moran, and George W Swenson. *Interferometry and synthesis in radio astronomy*. Springer Nature, 2017.
- [83] Kip S Thorne, Charles W Misner, and John Archibald Wheeler. *Gravitation*. Freeman San Francisco, 2000.
- [84] Ashutosh Tripathi, Sourabh Nampalliwar, Askar B Abdikamalov, Dmitry Ayzenberg, Jiachen Jiang, and Cosimo Bambi. Testing the Kerr nature of the supermassive black hole in ark 564. *Physical Review D*, 98(2):023018, 2018.
- [85] Ashutosh Tripathi, Jinli Yan, Yuchan Yang, Yunfeng Yan, Marcus Garnham, Yu Yao, Songcheng Li, Ziyu Ding, Askar B Abdikamalov, Dmitry Ayzenberg, et al. Constraints on the spacetime metric around seven “bare” AGNs using X-ray reflection spectroscopy. *The Astrophysical Journal*, 874(2):135, 2019.
- [86] AK Verma, Agnes Fienga, Jacques Laskar, Herve Manche, and Mickael Gastineau. Use of messenger radioscience data to improve planetary ephemeris and to test general relativity. *Astronomy & Astrophysics*, 561:A115, 2014.
- [87] Sarah Vigeland, Nicolás Yunes, and Leo C Stein. Bumpy black holes in alternative theories of gravity. *Physical Review D*, 83(10):104027, 2011.
- [88] Sarah J Vigeland and Scott A Hughes. Spacetime and orbits of bumpy black holes. *Physical Review D*, 81(2):024030, 2010.
- [89] R. Craig Walker, Philip E. Hardee, Frederick B. Davies, Chun Ly, and William Junor. The Structure and Dynamics of the Subparsec Jet in M87 Based on 50 VLBA Observations over 17 Years at 43 GHz. *The Astrophysical Journal*, 855(2):128, March 2018.

- [90] Jonelle L Walsh, Aaron J Barth, Luis C Ho, and Marc Sarzi. The M87 black hole mass from gas-dynamical models of space telescope imaging spectrograph observations. *The Astrophysical Journal*, 770(2):86, 2013.
- [91] Mingzhi Wang, Songbai Chen, and Jiliang Jing. Chaotic shadow of a non-Kerr rotating compact object with quadrupole mass moment. *Physical Review D*, 98(10):104040, 2018.
- [92] B. Louise Webster and Paul Murdin. Cygnus X-1-a Spectroscopic Binary with a Heavy Companion ? *Nature*, 235(5332):37–38, January 1972.
- [93] Huan Yang, David A. Nichols, Fan Zhang, Aaron Zimmerman, Zhongyang Zhang, and Yanbei Chen. Quasinormal-mode spectrum of Kerr black holes and its geometric interpretation. *Physical Review D*, 86(10), nov 2012.

Appendices

Appendix A

Additional solutions to $\eta = 0$ for the KN metric

In section 3.1.3 we wanted to know the solutions to the equation $\eta = 0$, where $\eta = \chi - (\lambda - a)^2$ and χ and λ are given by (3.18) and (3.24). These solutions determine the range of r -values for which bound photon orbits are possible. The two largest real solutions are shown in Figure 3.3. Figures A.1 and A.2 show the third and fourth solution, respectively. It is not very well visible in Figure A.1, but the edge of the circle, corresponding to extremality, always corresponds to the third root being equal to 1. The fourth root also equals 1 for $Q = 1, a = 0$, but decreases for increasing a .

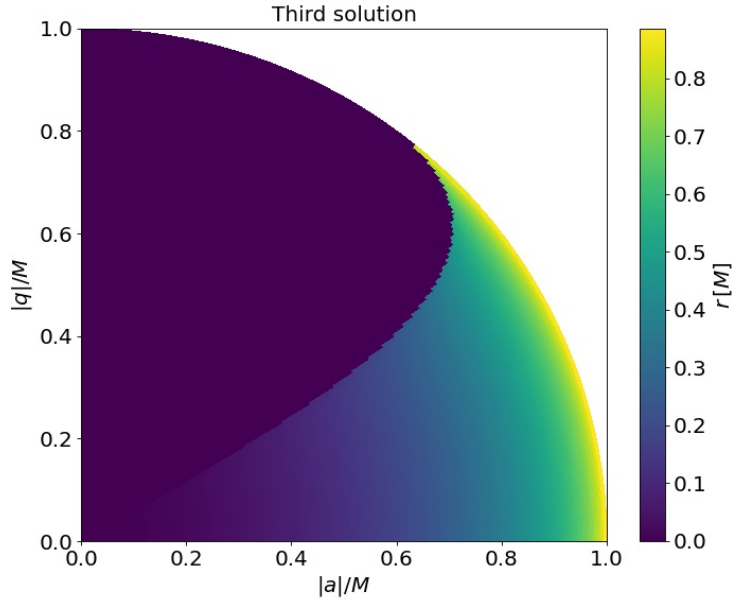


Figure A.1: The third solution to the equation $\eta = 0$ for the Kerr-Newman metric, for varying parameters a and q . The color corresponds to the value of the solution, expressed in gravitational radii. Wherever the result is 0, the solution is actually imaginary, but replaced for visual convenience.

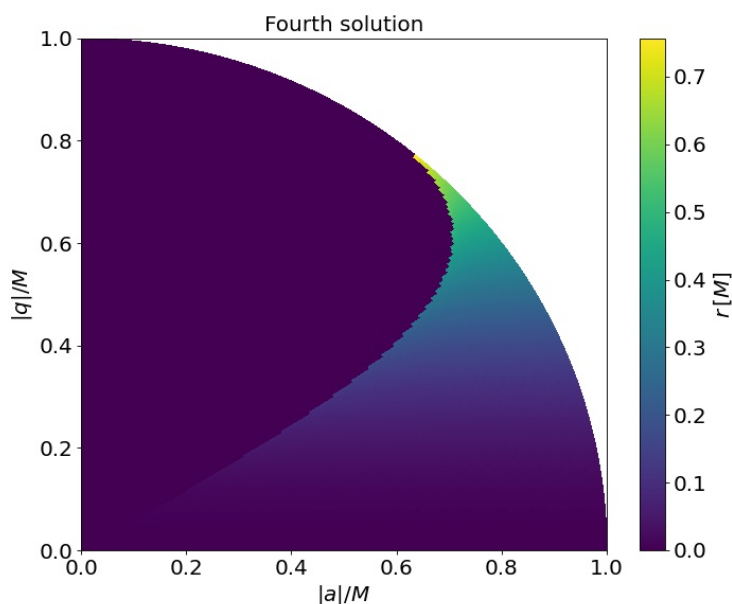


Figure A.2: The fourth solution to the equation $\eta = 0$ for the Kerr-Newman metric, for varying parameters a and q . The color corresponds to the value of the solution, expressed in gravitational radii. Wherever the result is 0, the solution is actually imaginary, but replaced for visual convenience.

Appendix B

Estimates for the Lyapunov exponent

In section 5.3 we have given an example of a plot with estimates for the Lyapunov exponent for a specific model (see Figure 5.8). We have made similar estimates for the other models in Table 5.1 as well. They are shown in Figures B.1, B.2, B.3 and B.4.

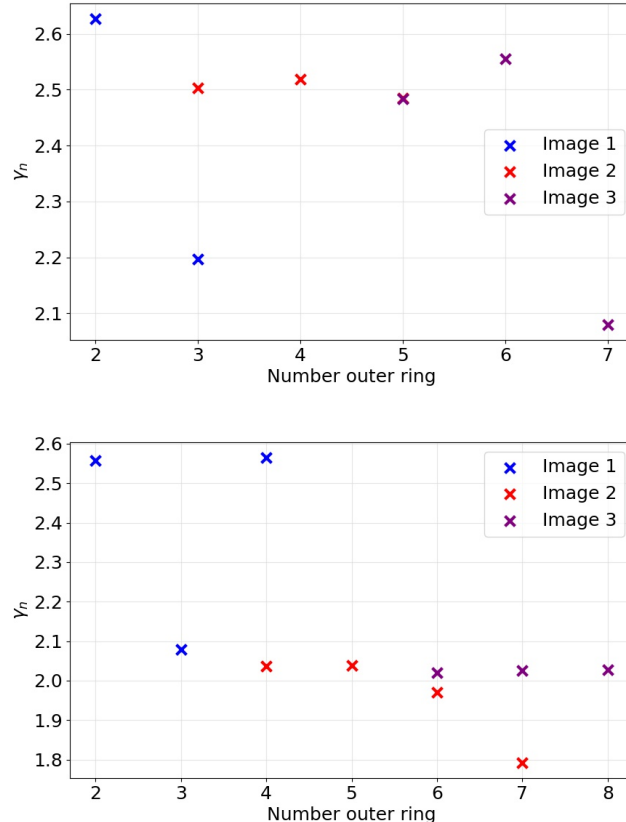


Figure B.1: Estimates for the Lyapunov exponent at on-screen angle $\phi_R = \pi$ for the almost-BPS metric with non-zero parameters $\mathbf{Q} = (2, 1, 1, 1) \cdot \zeta$, $\alpha = \zeta^2$ and (top) $h = 1$, (bottom) $h = 0.3$.

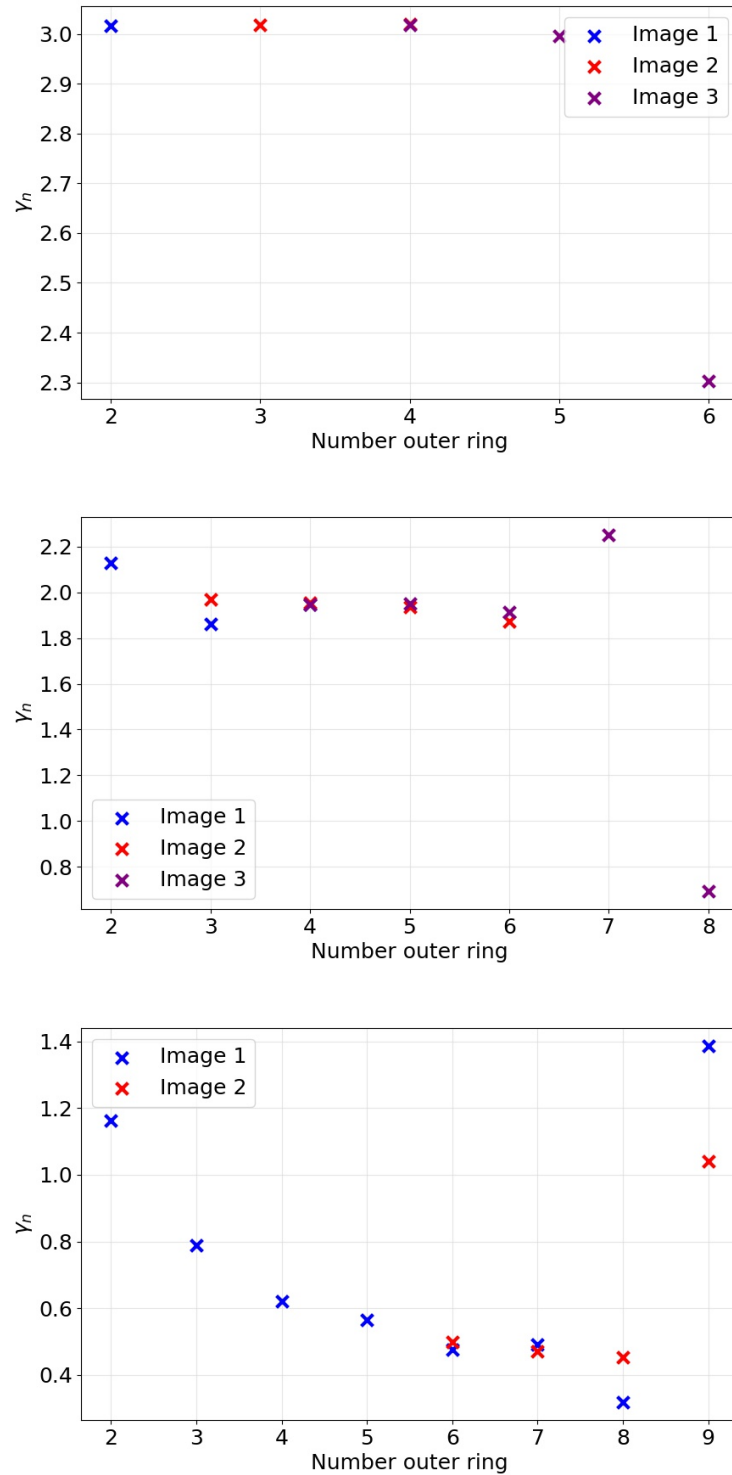


Figure B.2: Estimates for the Lyapunov exponent at on-screen angle $\phi_R = \pi$ for the Kerr metric with (top) $a = 0.1M$, (middle) $a = 0.7M$ and (bottom) $a = 0.99M$.

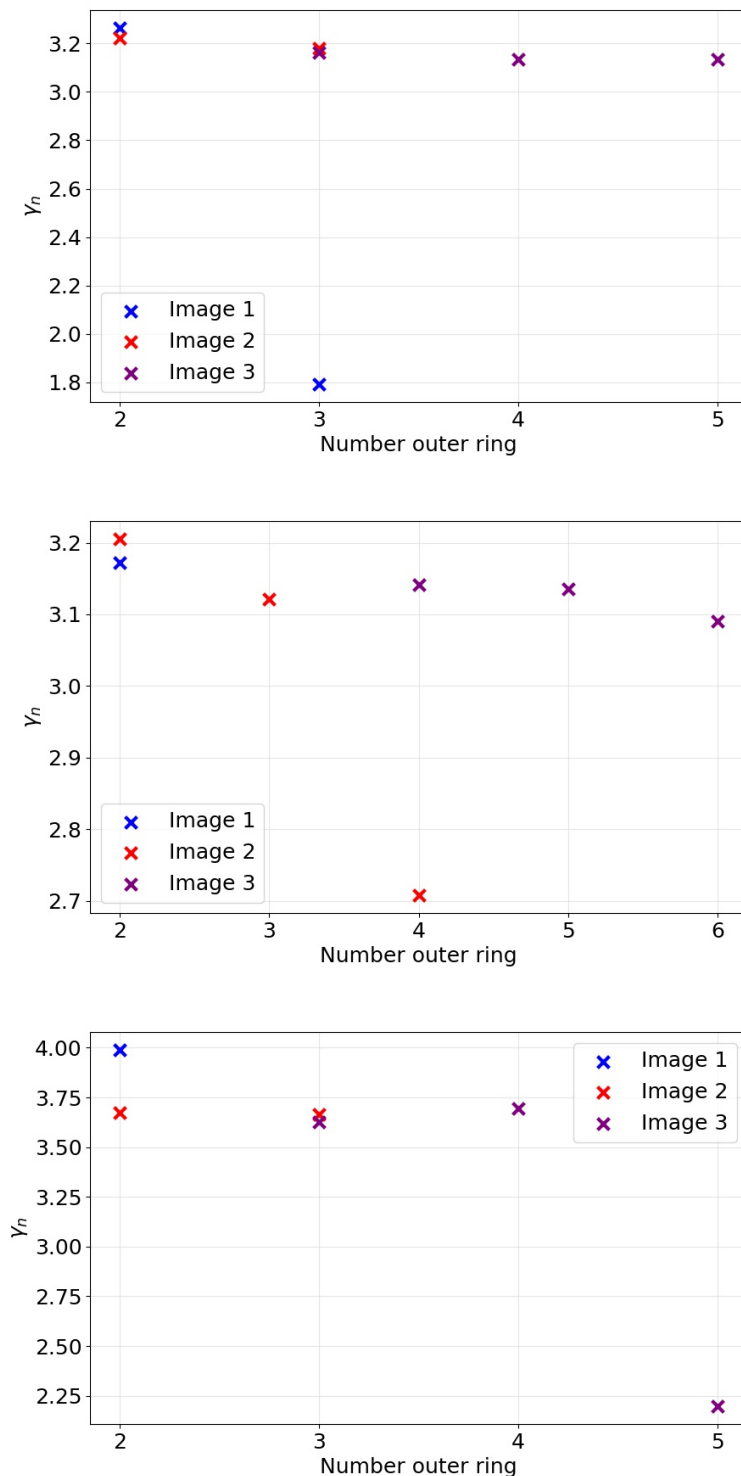


Figure B.3: Estimates for the Lyapunov exponent at on-screen angle $\phi_R = \pi$ for the Johannsen metric with $a = 0$ and non-zero parameters (*top*) $\alpha_{13} = 2$, (*middle*) $\alpha_{22} = 2$ and (*bottom*) $\alpha_{52} = 3$.

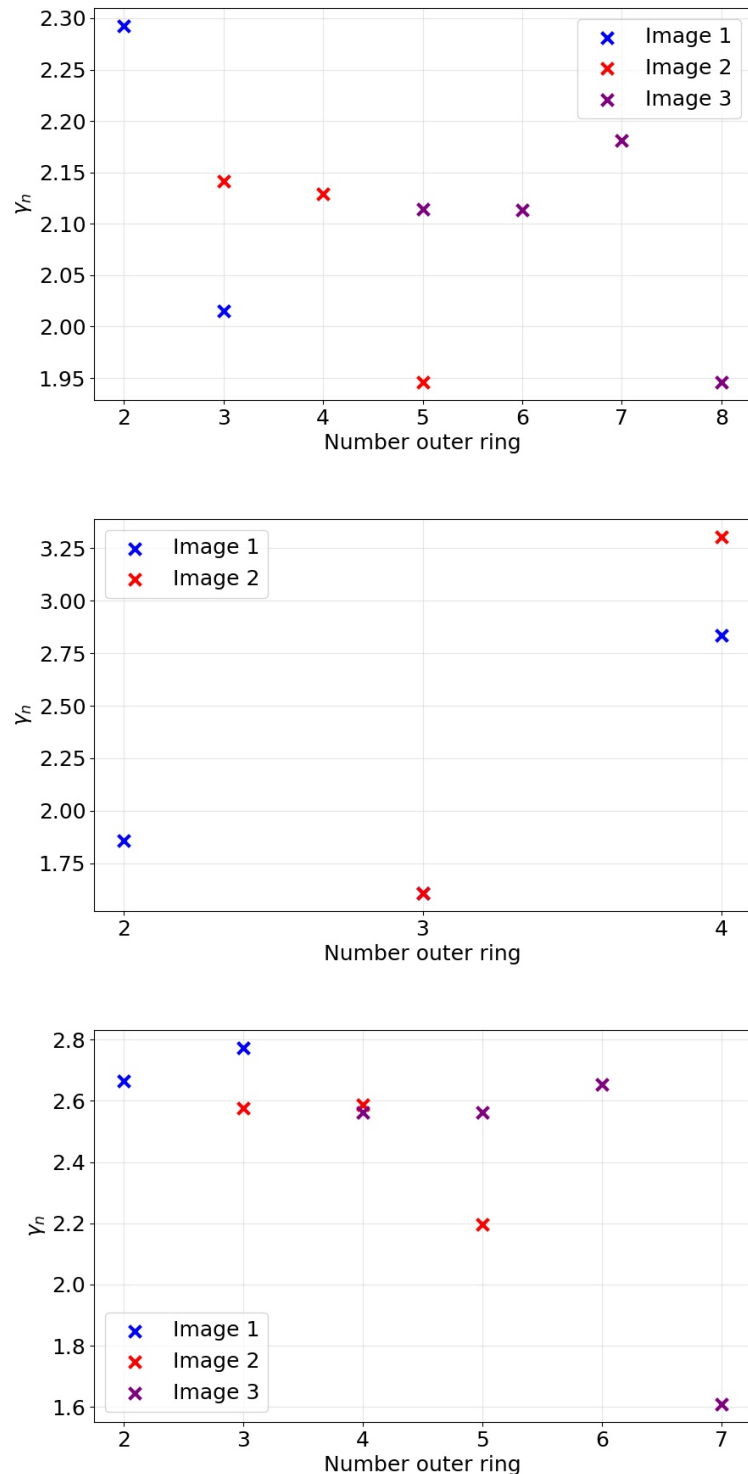


Figure B.4: Estimates for the Lyapunov exponent at on-screen angle $\phi_R = \pi$ for the Johannsen metric with non-zero parameters $a = 0.7M$ and (top) $\alpha_{13} = 2$, (middle) $\alpha_{22} = 2$ and (bottom) $\alpha_{52} = 3$.

Appendix C

Bumpy black hole metrics

The black hole metrics that we present in this section are not discussed in detail. We have implemented them in the RAPTOR code and used them to make the images in Figure 6.1 in Chapter 6. They provide an explicit example of metrics that do not have an equatorially symmetric shadow. They belong to a class of "bumpy" black holes, and the interested reader can find more information in [34].

C.1 Linearized bumpy black hole

This section considers a bumpy Kerr black hole as described in [88]. It is a solution to the linearized Einstein equations, and constructed from a bumpy Schwarzschild black hole to which the Newman-Janis algorithm is applied. The metric is given by

$$\boxed{\begin{aligned} ds^2 = & -e^{2\psi} F dt^2 + e^{2\psi-\gamma} \frac{4aMr \sin^2 \theta}{\Sigma} \left[(1-e^\gamma) \frac{a}{\Delta} dt dr - dt d\phi \right] \\ & + e^{2\gamma-2\psi} F^{-1} \left[1 + e^{-2\gamma} (1-2e^\gamma) \frac{a^2 \sin^2 \theta}{\Delta} \right. \\ & \quad \left. - e^{4\psi-4\gamma} (1-e^\gamma)^2 \frac{4a^4 M^2 r^2 \sin^4 \theta}{\Delta^2 \Sigma^2} \right] dr^2 \\ & - 2(1-e^\gamma) a \sin^2 \theta \left[e^{-2\psi} F^{-1} - e^{2\psi-2\gamma} \frac{4a^2 M^2 r^2 \sin^2 \theta}{\Delta \Sigma (\Sigma - 2Mr)} \right] dr d\phi \\ & + e^{2\gamma-2\psi} \Sigma d\theta^2 + \Delta \left[e^{-2\psi} F^{-1} - e^{2\psi-2\gamma} \frac{4a^2 M^2 r^2 \sin^2 \theta}{\Delta \Sigma (\Sigma - 2Mr)} \right] \sin^2 \theta d\phi^2. \end{aligned}} \quad (C.1)$$

In this expression, we have $F = 1 - \frac{2Mr}{\Sigma}$, $\Delta = r^2 - 2Mr + a^2$ and $\Sigma = r^2 + a^2 \cos^2 \theta$. The exponentials are used for notational convenience, but should be interpreted as $e^x \equiv 1+x$.

We have only considered the octupole bump ($l = 3$), i.e.

$$\psi(r, \theta) = \frac{B_3 M^4}{4} \sqrt{\frac{7}{\pi}} \frac{1}{D^4} \left[\frac{5L^3 \cos^3 \theta}{D^3} - \frac{3L \cos \theta}{D} \right], \quad (\text{C.2})$$

$$\gamma(r, \theta) = \frac{B_3 M^5}{2} \sqrt{\frac{7}{\pi}} \frac{\cos \theta}{D^7} [c_0 + c_2 \cos^2 \theta + c_4 \cos^4 \theta + c_6 \cos^6 \theta]. \quad (\text{C.3})$$

In these expressions, we have used the following functions:

$$D(r, \theta, a) = \sqrt{r^2 - 2Mr + (M^2 + a^2) \cos^2 \theta}, \quad (\text{C.4})$$

$$L(r, \theta, a) = \sqrt{(r - M)^2 + a^2 \cos^2 \theta}, \quad (\text{C.5})$$

$$\begin{aligned} c_0(r, a) &= -3r(r - 2M), \\ c_2(r, a) &= 10r(r - 2M) + 2M^5 - 3a^2, \\ c_4(r, a) &= -7r(r - 2M) + 10a^2, \\ c_6(r, a) &= -2M^2 - 7a^2. \end{aligned}$$

C.2 Manko-Novikov black hole

Two asymptotically flat generalizations of the Kerr-Newman solution are presented in [71]. They describe an arbitrary charged rotating axisymmetric mass. In contrast with earlier work, the event horizon of the obtained metrics is singular only at the equator. The starting point is the Weyl-Papapetrou line element in prolate spheroidal coordinates:

$$ds^2 = -f(dt - \omega d\phi)^2 + \frac{k^2}{f} e^{2\gamma} (x^2 - y^2) \left(\frac{dx^2}{x^2 - 1} + \frac{dy^2}{1 - y^2} \right) + \frac{k^2}{f} (x^2 - 1) (1 - y^2) d\phi^2.$$

(C.6)

In this equation, k is a real constant and f, γ and ω are three functions that depend only on x, y . We will consider the first solution in [71], corresponding to equations (9)-(13) in the article. Again, we only consider an octupole deformation ($n = 3$ in the notation of the original paper), and therefore the formulas presented here are already adapted to our needs. It should be noted that there are two typos¹ in the original paper, and therefore

¹One is in the expression for M_2 : the original paper writes α_2 at the end, which should be α^2 . The other is in the expression (13) of the original paper: the -1 and $(-1)^n$ at the end of the expressions should not be taken into the sum.

the formulas below are based on [43]. The plethora of expressions that go into (C.6) are:

$$\begin{aligned} f &= e^{2\psi} \frac{A}{B}, \\ \omega &= 2ke^{-2\psi} \frac{C}{A} - 4k \frac{\alpha}{1 - \alpha^2}, \\ e^{2\gamma} &= e^{2\gamma'} \frac{A}{(x^2 - 1)(1 - \alpha^2)^2}, \\ \psi &= \alpha_3 \frac{P_3}{R^4}, \\ \gamma' &= \frac{1}{2} \ln \frac{x^2 - 1}{x^2 - y^2} + 2\alpha_3^2 \frac{P_4^2 - P_3^2}{R^8} + \alpha_3 \sum_{l=0}^3 \left(\frac{x - y + (-1)^{3-l}(x + y)}{R^{l+1}} P_l \right), \end{aligned}$$

$$\begin{aligned} A &= (x^2 - 1)(1 + ab)^2 - (1 - y^2)(b - a)^2, \\ B &= [x + 1 + ab(x - 1)]^2 + [(1 + y)a + (1 - y)b]^2, \\ C &= (x^2 - 1)(1 + ab)[b - a - y(a + b)] + (1 - y^2)(b - a)[1 + ab + x(1 - ab)], \end{aligned}$$

$$\begin{aligned} a &= -\alpha \exp \left(2\alpha_3 \left[1 - (x - y) \sum_{l=0}^3 \frac{P_l}{R^{l+1}} \right] \right), \\ b &= \alpha \exp \left(2\alpha_3 \left[-1 + (x + y) \sum_{l=0}^3 \frac{(-1)^l P_l}{R^{l+1}} \right] \right), \end{aligned}$$

$$R = \sqrt{x^2 + y^2 - 1}.$$

The P_l are the Legendre polynomials evaluated at xy/R , i.e. $P_l = P_l(xy/R)$. The Manko-Novikov metric as described above can be brought to Boyer-Lindquist coordinates by the following transformation [91]:

$$x = \frac{r - M}{k}, \quad y = \cos \theta. \quad (\text{C.7})$$

The result of this transformation is the line element

$$ds^2 = -f(dt - \omega d\phi)^2 + \frac{e^{2\gamma}\rho^2}{f\Delta} dr^2 + \frac{e^{2\gamma}\rho^2}{f} d\theta^2 + \frac{\Delta \sin^2 \theta}{f} d\phi^2, \quad (\text{C.8})$$

where $\rho^2 = (r - M)^2 - k^2 \cos^2 \theta$ and $\Delta = (r - M)^2 - k^2$. The outer event horizon is now located at $r_H = M + k$.

DEPARTMENT OF PHYSICS AND ASTRONOMY

Celestijnenlaan 200D bus 2412

3001 LEUVEN, BELGIUM

tel. + 32 16 32 71 24

fys.kuleuven.be

